# A Body Force Model for Cavitating Inducers in Rocket Engine Turbopumps

by

William Alarik Sorensen

S.B., Massachusetts Institute of Technology (2012)

Submitted to the Department of Aeronautics and Astronautics
in partial fulfillment of the requirements for the degree of

Master of Science in Aeronautics and Astronautics

at the

MASSACHUSETTS INSTITUTE OF TECHNOLOGY

September 2014

Author . . . . . . . . . . . . . . . . . . . . . . . . . . . . . . . . . . . . . . . . . . . . . . . . . . . . . .
Department of Aeronautics and Astronautics
August 6, 2014

Certified by . . . . . . . . . . . . . . . . . . . . . . . . . . . . . . . . . . . . . . . . . . . . . . . . . . . .
Zoltán S. Spakovszky
Professor of Aeronautics and Astronautics
Thesis Supervisor

Accepted by . . . . . . . . . . . . . . . . . . . . . . . . . . . . . . . . . . . . . . . . . . . . . . . . . . . .
Paulo C. Lozano
Associate Professor of Aeronautics and Astronautics
Chair, Graduate Program Committee

# A Body Force Model for Cavitating Inducers in Rocket Engine Turbopumps

by

William Alarik Sorensen

Submitted to the Department of Aeronautics and Astronautics
on August 6, 2014, in partial fulfillment of the
requirements for the degree of
Master of Science in Aeronautics and Astronautics

## Abstract

Modern rocket engine turbopumps utilize cavitating inducers to meet mass and volume requirements. Rotating cavitation and higher order cavitation instabilities have frequently been observed during inducer testing and operation and can cause severe asymmetric loading on the inducer blades and shaft, potentially leading to failure of the inducer. To date no broadly applicable design method exists to characterize and suppress the onset of cavitation instabilities.

This thesis presents the development of a body force model for cavitating inducers with the goal of enabling interrogation of the onset of rotating cavitation and higher order cavitation instabilities and characterization of the governing fluid dynamic mechanisms. Building on body force models of gas turbine compressors for compressor stability, the model introduces an additional force component, the binormal force, to capture the strong radial flows observed in inducer flow fields. The body forces were defined and the methodology was successfully validated for two test inducers, a helical inducer and a more advanced design resembling the Space Shuttle Main Engine Low Pressure Oxidizer Pump. The head rise characteristic of each test inducer was captured with less than 4% error across the operating range and the extent of the upstream backflow region was predicted to within 18% at every operating condition. Several challenges with the blade passage model were encountered during the course of the research and the diagnostics performed to investigate them are detailed. An extension of the body force model to two-phase flows was formulated and preliminary calculations with the extended model are presented. The preliminary two-phase results are encouraging and pave the way for future assessment of rotating cavitation instabilities.

Thesis Supervisor: Zoltán S. Spakovszky
Title: Professor of Aeronautics and Astronautics

# Acknowledgments

I would like to thank first my advisor, Professor Zoltán S. Spakovszky, for the opportunity to study at the Gas Turbine Laboratory, and for the countless lessons he has taught me over the course of my graduate education, not the least of which is the direction a compressor spins.

I am indebted to NASA and the SLS Program for their financial and technical support of my research, especially our technical monitors at Marshall Space Flight Center, Tom Zoladz and Andy Mulder, whose insight and advice during our monthly telecons was invaluable.

I would also like to thank Dr. Claudio Lettieri for his tremendous help and support throughout the course of the project, and for educating me on all matters related to CFD and turbomachinery I had the whim to ask about.

I am grateful for the support and friendship offered by everyone in the Gas Turbine Lab over my tenure here. A special thanks must go to the members of Team Body Force, Max, Anjaney, and Andreas, for their many hours spent educating me and debating me on the finer points of the body force methodology. I am also grateful for the camaraderie of my office mates David, Sebastian, and Peter.

I could not have succeeded in my education without the help of my friends Andres, Brett, Arni, and Katy. Their constant willingness to provide welcome distraction from work will always be appreciated. I would also like to thank my roommates Gavin, Max, Aaron, and Sarah for their nonchalance towards my unpredictable working schedule and constant friendship.

Finally, I would like to thank my parents and my sister Megan for their never ending love and support. Without them I could never have reached where I am now, and their strength through adversity and hardship, especially in recent years, has always inspired me.

# Contents

# List of Figures

# List of Tables

# Nomenclature

## Symbols

| | |
|---|---|
| $A$ | area |
| $B$ | passage free area ratio |
| $c$ | axial chord |
| $C_p$ | coefficient of static pressure |
| $f_h$ | binormal force |
| $f_p$ | parallel force |
| $f_n$ | normal force |
| $F_{cone}$ | condensation rate factor |
| $F_{gap}$ | vaporization rate factor |
| $K_{off}$ | normal force model offset |
| $N_D$ | design specific speed |
| $p$ | static pressure |
| $p_t$ | stagnation pressure |
| $p_v$ | vapor pressure |
| $r$ | radius |
| $R_{nuc}$ | cavitation nucleation site radius |
| $S_{cav}$ | cavity blockage model source term |
| $S_m$ | blade metal blockage model mass source term |
| $S_r$ | blade metal blockage model radial momentum source term |
| $S_x$ | blade metal blockage model axial momentum source term |
| $S_\theta$ | blade metal blockage model circumferential momentum source term |
| $u$ | stationary frame velocity |
| $u_{tip}$ | blade tip speed |
| $w$ | relative frame velocity |
| $x$ | axial location |

### Greek symbols

| | |
|---|---|
| $\alpha_v$ | vapor volume fraction |
| $\alpha_{nuc}$ | cavitation nucleation site volume fraction |
| $\beta$ | relative flow angle |
| $\delta_\beta$ | relative flow angle deviation |
| $\delta_\varphi$ | pitch angle deviation |
| $\kappa$ | blade metal angle |
| $\rho$ | density |
| $\sigma$ | cavitation number |
| $\phi$ | flow coefficient |
| $\psi$ | head rise coefficient |
| $\Omega$ | inducer shaft speed |
| $\varphi$ | flow pitch angle |
| $\varphi_{GP}$ | geometric gas path angle |

### Vectors

| | |
|---|---|
| $\hat{\mathbf{h}}$ | binormal direction unit vector |
| $\hat{\mathbf{l}}$ | parallel direction unit vector |
| $\hat{\mathbf{m}}$ | meridional direction unit vector |
| $\hat{\mathbf{n}}$ | normal direction unit vector |
| $\hat{\mathbf{r}}$ | radial direction unit vector |
| $\hat{\mathbf{x}}$ | axial direction unit vector |
| $\hat{\theta}$ | circumferential direction unit vector |
| $\mathbf{u}$ | stationary frame velocity vector |
| $\mathbf{w}$ | relative frame velocity vector |

### Superscripts

| | |
|---|---|
| $\bar{\ }$ | pitchwise averaged quantity |
| $\hat{\ }$ | body force calculation quantity |

### Subscripts

| | |
|---|---|
| eff | effective |
| h | conditions at hub |
| in | conditions at inlet |
| $\ell$ | liquid phase |
| m | meridional component |
| $MFA$ | mass flow average |
| out | conditions at outlet |
| r | radial component |
| t | conditions at tip |
| v | vapor phase |
| x | axial component |
| $\theta$ | circumferential component |

### Acronyms

| | |
|---|---|
| LOX | liquid oxygen |
| LPOP | low pressure oxidizer pump |
| P-LPOP | pseudo-low pressure oxidizer pump |
| PWA | pratt and whitney aircraft |
| SSME | space shuttle main engine |

# Chapter 1

# Introduction

## 1.1 Background and Motivation

System level design trades for launch vehicles drive modern rocket engines to use high specific power density turbopumps to provide the pressurized propellents for combustion. The high rotational speeds of the turbopumps required to minimize mass and volume lead to operating conditions where cavitation can occur. In order to prevent the highly loaded main impeller from experiencing cavitation, typical turbopump designs feature an axial inducer as the first stage to raise the static pressure sufficiently so as to prevent cavitation in the downstream components. As a consequence, the inducer must be designed to be robust to the loads and stresses imparted by cavitation behavior. If the cavitation behavior is unsteady, severe vibrations can be created within the pump, and large asymmetric loads can be placed on the blades and shaft of the inducer.

Unsteady cavitation phenomena which produce such loads and vibrations are referred to as cavitation instabilities and have been observed in the turbopump development process for many engine programs, including the liquid oxygen and liquid hydrogen turbopump inducers of Japan's LE-7 engine [11], the High Pressure Oxidizer Turbopump of NASA's Space Shuttle Main Engine (SSME) [19], and the LOX turbopump of NASA's FASTRAC engine [27]. In each of these cases, the cavitation instabilities experienced were discovered late in the development program and well into turbopump component testing; in the case of the LE-7 engine, a previously unobserved cavitation instability was determined as the root cause for the fatigue failure of an inducer blade in flight, resulting in the loss of the mission [10]. Despite significant research, no widely applicable method exists to date that can predict the onset of cavitation instabilities during the design phase before expensive hardware fabrication and testing begin. Moreover, due to the challenging three dimensional unsteady nature of the phenomenon, the physical mechanisms which govern the behavior have yet to be characterized.

For organizations developing turbopumps, the capability to determine the onset of cavitation instabilities from first principles would simultaneously improve reliability and decrease development costs. NASA's Space Launch System (SLS) in particular stands to benefit from improvements to the inducer design process. With new turbopumps under development for the J2-X upper stage engine and the SSME tubompumps experiencing different operating conditions on the new core stage compared to their role on the Space Shuttle, identification of the mechanisms of cavitation instabilities and the development of first principles based design guidelines for inducers could reduce risk for the system,and improve both reliability and performance.

### 1.1.1 Cavitation Instabilities in Inducers

Many distinct cavitation instability patterns exist. The exact forms which occur in an inducer are highly dependent both on the geometry of the inducer itself and on the operating conditions, namely the flow coefficient $\phi$ (representative of the incidence angle of flow) and the cavitation number $\sigma$ (the nondimensional difference between the local static pressure and the liquid's vapor pressure). This dependence can be observed in a cavitation map, as for example seen in Figure 1-1 for a scale model of the LE-7 LOX turbopump inducer, which uses the static pressure rise coefficient as a surrogate for the incidence angle. Generated from experimental data [25], several of the most critical cavitation instabilities are represented, namely rotating cavitation and higher order cavitation, backflow cavitation, and cavitation surge.

Cavitation surge, also referred to as inducer autooscillation in the literature, is

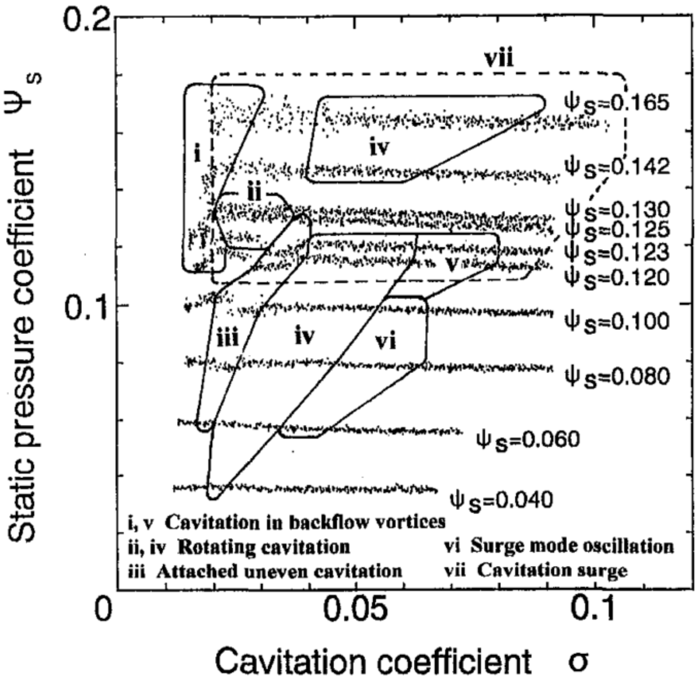

Figure 1-1: Cavitation instability map for scale LE-7 inducer, from [25]

characterized by largely one dimensional oscillations in the inducer upstream pressure field, and somewhat resembles traditional compressor surge, with the cavities providing the fluid compliance necessary for surge [23]. Backflow cavitation consists of unsteady cavity formation in the turbulent backflow regions upstream of the blade row generated by the pressure driven tip clearance flows [3].

Rotating cavitation and higher order cavitation, the primary instabilities of concern for this work, are highly three dimensional flow features which create strong asymmetric periodic loading patterns on the inducer blades [23]. These instabilities typically rotate at 1.1 to 1.3 times the shaft speed of the inducer. A strong parallel can be drawn between rotating cavitation and rotating stall as observed in axial gas turbine compressors - just as a stall cell propagates from blade to blade driving rotating stall, a disturbance in the relative size of the blade cavities travels circumferentially during rotating cavitation.

Efforts to model cavitation instabilities in the literature have largely been formulated as one- and two-dimensional linearized approaches. Early work by Brennen [4]

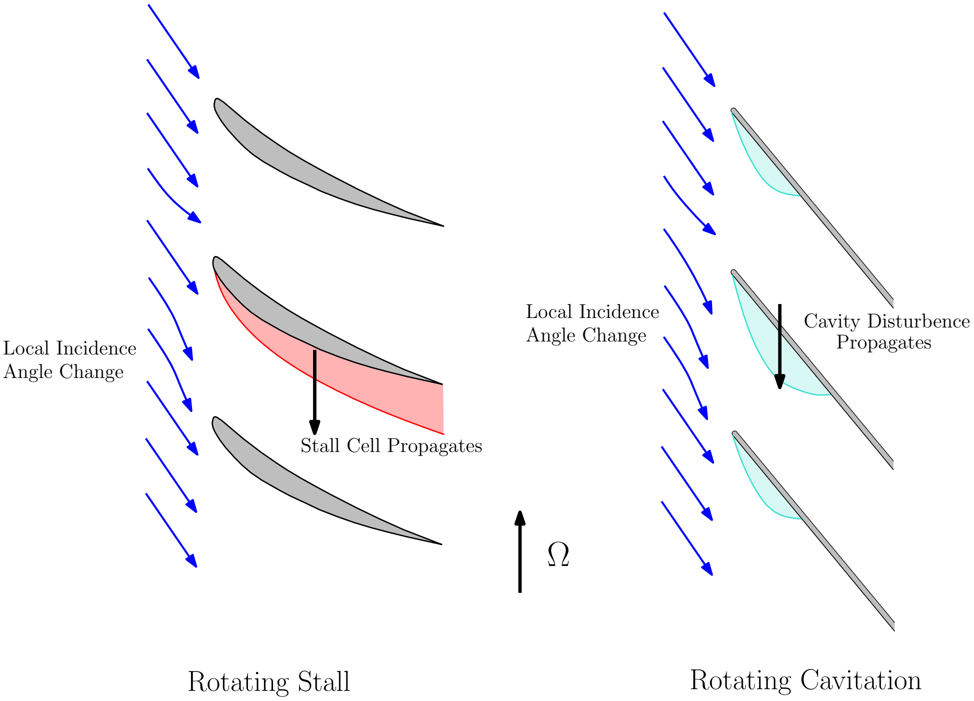

Figure 1-2: Qualitative comparison between rotating stall and rotating cavitation behaviors in relative frame, adapted from [13]

utilized one-dimensional transfer functions to model cavitating inducers with some success in capturing cavitation surge. Tsujimoto [24] proposed a linear two dimensional model for rotating cavitation that was able to explain some elements of observed behavior. Later, Brennen and Tsujimoto [23] laid out a unified analytical framework to model four major flow instabilities in inducers: surge, cavitation surge, rotating stall, and rotating cavitation. The analysis applied similar modeling techniques for each "traditional" instability and its cavitation equivalent, treating the flow as either one-dimensional, for surge and cavitation surge, or two-dimensional, for rotating stall and rotating cavitation. Two distinct modes for rotating cavitation were estimated, the previously observed forward rotating mode, and a backward rotating mode slower than the shaft speed. The backward mode has been difficult to identify in experiments, though Tsujimoto notes some potential observations in experimental work with the LE-7 LOX turbopump inducer [25]. The models developed are dependent on experimental data for key parameters, and as such are of limited use in predicting a priori the onset of rotating cavitation for a new inducer design. The true three-dimensional nature of rotating cavitation as observed in experiments is not captured by these models.

High-fidelity simulations have recently been applied to modeling rotating cavitation and higher order cavitation with some success. For example, Ugajin et al [26] successfully captured the unsteady, cavitating flow field of an inducer using DES calculations. Hosangadi [7, 8, 9] has had similar success capturing unsteady cavitation using URANS calculations, even recreating the experimentally observed frequency spectrum of dynamic pressure fluctuations at the leading edge of a scale model of the SSME Low Pressure Fuel Pump Inducer. While these methods are able to compute rotating cavitation, the involved computational costs prohibit the determination of the causal links between the inducer geometry and the flow features necessary for rotating cavitation. Furthermore, these methods are currently infeasible for use in the inducer design phase and for testing hypotheses and new design concepts.

### 1.1.2 Problem Statement and Approach

The research in this thesis seeks to identify the fundamental fluid dynamic mechanisms which govern the onset and development of rotating cavitation and higher order cavitation instabilities. The so-called body force modeling methodology, which has previously been successfully applied to the study of aerodynamic instabilities in axial and centrifugal compressors [1] as well as the design space exploration of novel short inlet nacelles for high bypass ratio turbofans [17] is proposed here to model the cavitation instabilities with the goal of identifying the governing mechanisms.

The idea is to model the onset of rotating cavitation by representing the inducer blades with force field distributions (so-called body forces) in an unsteady, three-dimensional two-phase flow calculation. The key attributes of this modeling approach are that, one, it defines the causal link between the desired flow field and the required fluid force distribution without having to consider device geometry, and two, it models all relevant length and time scales in a holistic approach to capture component interactions and flow field coupling. From a computational perspective there are a number of advantages including carrying out unsteady calculations without sliding interfaces, performing steady calculations without mixing planes, and use of simplified mesh topographies, all of which can lead to significant reductions in computational cost.

Let's take the example of applying the body force methodology to investigate the behavior of casing treatmemst: many strategies for mitigating rotating cavitation with casing treatments have been determined experimentally on a case-by-case basis for individual inducer designs. Kamijo et al [11] tested multiple inducer housings which modified the tip clearance at different axial locations, eventually identifying a design which suppressed rotating cavitation. Similar development processes were undertaken by Shimiya et al [21] , who successfully suppressed rotating cavitation with a "J groove" casing treatment near the inducer leading edge tip, and Subbaraman et al [22], who achieved success by implementing a Tip Vortex Suppressor, essentially a fluid jet which increased axial velocity in the tip clearance region. Each of these approaches started with a particular casing treatment geometry and required multiple iterations on a trial and error basis. The proposed body force methodology, however, would determine the force field necessary to suppress rotating cavitation and then define the corresponding casing treatment geometry which creates this force field.

### 1.1.3 Body Force Modeling of Turbomachinery

The body force modeling methodology was first introduced by Marble [15]. The underlying idea is to represent the effects of the discrete blades on the flow via force distributions as shown in Figure 1-3. In this work, the forces are determined based on the pitchwise averaged flow field of the inducer.

In Marble's original formulation of the methodology, as well as subsequent approaches, the body force field consists of two components, as shown in Figure 1-4. The normal force $f_n$, is normal to the flow, and captures the turning of the flow by the blades. The parallel force $f_p$, is parallel to the flow, and captures the viscous losses in the blade row, and correspondingly the change in entropy in the blade row. These relationships can be derived by combining the governing equations in the blade row with the Gibbs equation; the full derivation is given in [15] and more recently in

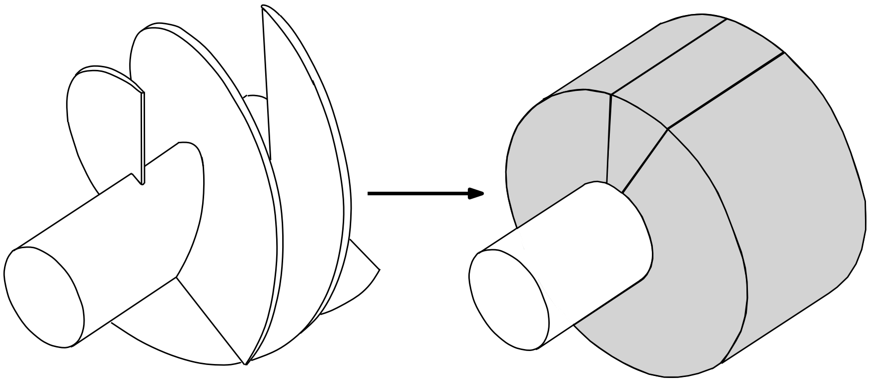

Figure 1-3: Body force representation of inducer

[13].

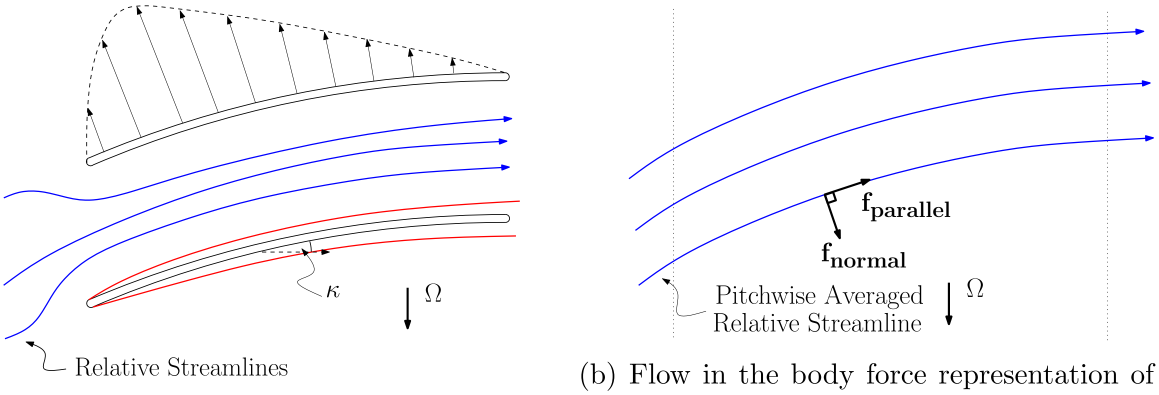

(a) Flow in the discrete blade passage

(b) Flow in the body force representation of the blade row

Figure 1-4: Normal and parallel force components

Several approaches have been taken to define the body forces. A brief summary of these approaches is given here and a more detailed analysis of their development and formulation may be found in [13]. Gong [5] developed a blade passage model based on the forces in a straight blade passage to allow the forces to adjust to inlet flow distortions and perturbations. The blade passage model contained two key elements: a dependence on the local flow field to allow the forces to respond to the perturbations, and an empirical parameter within the model to capture information about the forces the original discrete blade row applied on the fluid at a given operating point.

Benneke [1] used a look-up table for the force values at different operating conditions to allow the body force field to vary with local perturbations. This model was used to study the onset of rotating stall in vaned diffusers for centrifugal compressors.

The body force model successfully identified spike type and modal stall precursors which qualitatively agreed with unsteady pressure data gathered during the onset of rotating stall in experimental testing at different operating conditions.

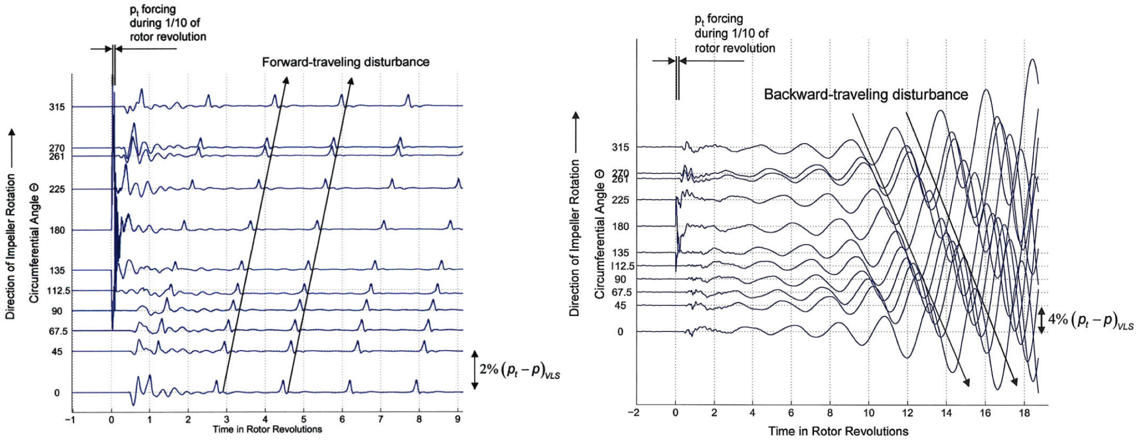

(a) Observed spike type stall precursors

(b) Observed modal stall precursors

Figure 1-5: Body force model recreation of spike type and modal stall precursors, from [1]

Peters [17] modified Gong's blade passage model, calculating a distribution of empirical term values at every location in the body force domain instead of a single value for the entire domain. A new parallel force model to capture the change in losses at different operating conditions and a coordinate transformation to capture the effects of blade cant and twist in a modern fan stage were also introduced. The new blade passage model enabled the design of novel short inlet nacelles for high bypass ratio turbofans. The body force model allowed simulation of the interaction between the fan and nacelle without having to carry out computationally expensive full wheel URANS calculations, enabling full exploration of the design space.

Recently, Brand [2] and Kottapalli [13] identified and corrected several inconsistencies in Gong's original blade passage model, including an inability to capture streamline curvature accurately in some cases, and a lack of physical interpretation of the empirical terms defined in the model. The body force model presented in this thesis was developed concurrently with the above models and a similar formulation is adopted to incorporate the model improvements and rectify the inconsistencies in

Gong's model.

To the author's knowledge, the present work represents the first time the implementation of the body force modeling methodology for two-phase flows and turbopump inducers. Relative to previous formulations, a new dependence on the flow pitch angle is introduced, an additional force component is added to capture the strong radial flows observed in inducer flow fields, and a preliminary model is introduced to account for cavity blockage within the flow.

## 1.2 Research Goals and Objectives

The overall objective of the multiyear research project this work is a part of is to provide a new capability to guide the design of cavitating inducers so as to suppress the onset of rotating and higher order cavitation instabilities. The end goals are to identify the required inducer blade loading distributions and end wall flow forcing requirements to suppress rotating cavitation and higher order cavitation instabilities, and to determine the blade geometry and casing treatment which create the required loading distributions and end wall forces.

In contribution to the goals of the multiyear project, the specific objectives of this thesis are to:

- Develop a body force model for a cavitating inducer which captures the inducer's single-phase performance and local flow field
- Extend the single phase body force model to two-phase flows and introduce an additional model to capture the effect of cavity blockage

## 1.3 Key Contributions

A body force model for a cavitating inducer was developed with the aim to investigate the onset and behavior of rotating cavitation and higher order cavitation instabilities. An extra force component, the binormal force, was introduced to capture the strong radial flow features produced by the unique design features of inducers, most notably the high blade stagger angles and leading edge backsweep. The force extraction process within the model was validated by capturing the steady, wetted performance of a test inducer across its entire operating range. A preliminary extension of the body force model to two phase flows was also carried out to capture the effect of cavity blockage not present in single phase flows.

## 1.4 Thesis Outline

This thesis is organized as follows: Chapter 2 presents an analysis of the performance and major flow features of two test inducer geometries, under both single phase (wetted) and two phase (cavitating) conditions. Chapter 3 describes the formulation and implementation of the body force model used to capture inducer behavior. Chapter 4 presents an assessment of the performance of the model for the test inducers, along with analysis of challenges encountered during the assessment. Chapter 5 summarizes the contributions of this research and provides guidance for future work.

# Chapter 2

# Characterization of Test Inducers

## 2.1 Representative Inducer Geometries

The primary inducer used in this research was the MIT Pseudo-Low Pressure Oxider Pump inducer (P-LPOP). The P-LPOP is based on publicly available data on NASA's Space Shuttle Main Engine Low Pressure Oxidizer Pump (SSME LPOP) Inducer. The reconstructed P-LPOP design may differ from the actual geometry, introducing an additional level of uncertainty ; see [14] for a full discussion of the P-LPOP reconstruction process and a comparison of experimental data from the P-LPOP and SSME LPOP designs. The P-LPOP inducer is a four bladed design that is representative of many modern inducers, exhibiting high blade stagger angles ($\sim 80°$), a backswept leading leading edge, significant gas path area contraction, and high blade cant angles. A secondary blade row, referred to as the "tandem blade" or "kicker", is also present, and consists of 12 blades which serve to increase the head rise of the device beyond that provided by the four main inducer blades.

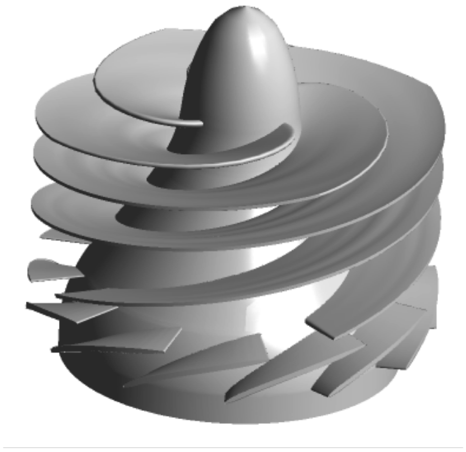

Figure 2-1: MIT Pseudo-Low Pressure Oxidizer Pump (P-LPOP) inducer geometry

A second inducer, the PWA inducer, was also used in the development of the body force model. The three bladed design created by Pratt and Whitney Aircraft in 1970 [20] shares some design features with the more modern P-LPOP inducer, including high blade stagger angles, but lacks leading edge backsweep or canted blades, making it a simpler test case for body force model diagnostics. The geometry for the PWA inducer was directly available [20], reducing uncertainty when comparing computations to the available experimental data.

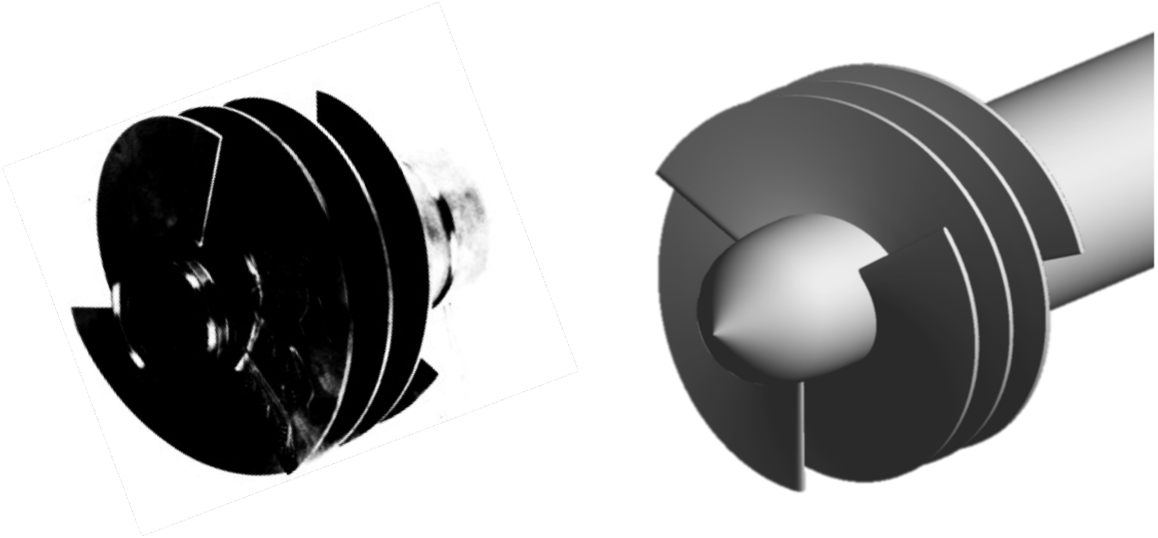

(a) PWA inducer hardware [20]

(b) CAD model of PWA inducer geometry

Figure 2-2: PWA inducer geometry

Data on the designs of both inducers is summarized in Table 2.1 below. The appropriate nondimensional design parameters are the flow coefficient $\phi$, which captures the mass flow of the device, head rise coefficient $\psi$, which captures the stagnation pressure rise, and the specific speed $N$, which is a single value representing the design objective of the inducer, containing information about the mass flow, head rise, and shaft speed.

$$\phi = \frac{u_{in}}{r_t \Omega} \tag{2.1}$$

$$\psi = \frac{p_{t_{out}} - p_{t_{in}}}{\rho r_t^2 \Omega^2} \tag{2.2}$$

$$N = \sqrt{\pi \left(1 - \frac{r_h^2}{r_t^2}\right)} \frac{\phi^{\frac{1}{2}}}{\psi^{\frac{3}{4}}} \tag{2.3}$$

Table 2.1: Design data for test inducers

| | P-LPOP | PWA Inducer |
|---|---|---|
| Number of Blades | 4 | 3 |
| Design Flow Coefficient, $\phi_D$ | 0.07 | 0.093 |
| Design Head Rise Coefficient, $\psi_D$ | 0.35 | 0.14 |
| Design Specific Speed, $N_D$ | 0.9 | 3.3 |
| Inlet Hub-to-Tip Radius Ratio, $(r_h/r_t)_{in}$ | 0.29 | 0.40 |
| Outlet Hub-to-Tip Radius Ratio, $(r_h/r_t)_{out}$ | 0.85 | 0.53 |

## 2.2 Inducer Performance Assessment - Steady Single-Phase Calculations

In order to characterize the wetted performance of the test inducers, steady CFD simulations were carried out and compared to experimental data to validate the computational procedures. Computational grids for both inducers were created using ANSYS Turbogrid, and were limited to a single passage with periodic boundary conditions to reduce mesh size. Each mesh contained approximately 1 million elements; the mesh utilized for simulations of the P-LPOP inducer is shown in Figure 2-3. The simulations were run using the ANSYS CFX commercial solver with the $k$-$\omega$ - SST turbulence model. A total pressure boundary condition was applied at the inlet, and a specified mass flow was applied at the outlet.

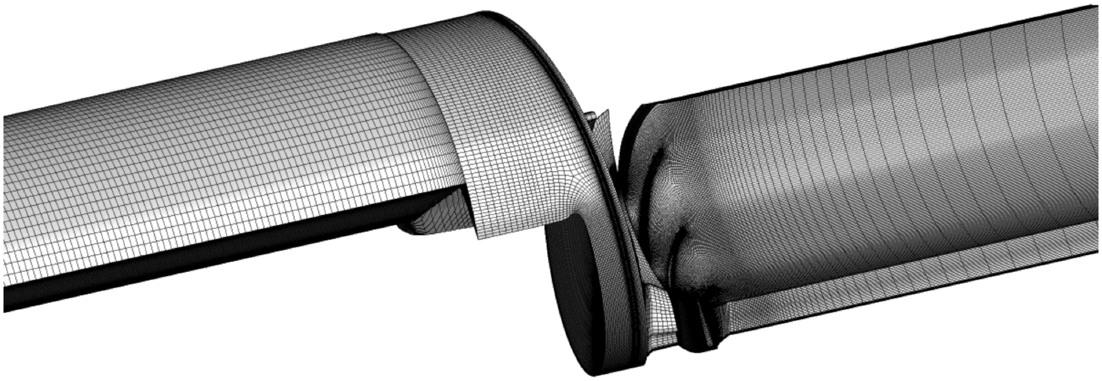

Figure 2-3: P-LPOP inducer single passage RANS computational mesh

The computed head rise characteristic at design speed for the PWA inducer, presented in Figure 2-4, agrees with the experimental data from [20], with less than 5% error across the range of data available. As expected for the simple inducer design, the characteristic is close to linear across the operating range and consistent with the shape of the ideal characteristic [3].

The computed P-LPOP inducer head rise characteristic (at design speed) captures the experimental data from [16] within 20% across its operating range, as shown in Figure 2-5. The larger variance from the experimental data compared to the PWA inducer is attributed to small but important geometry differences between the P-LPOP and SSME LPOP design. Both the experimental and computational data show a distinct non-linear behavior, with an inflection point around $\phi = 0.06$, and an offset in optimal efficiency points between the blade rows. The inflection in the characteristic is due to a mismatch between the trailing edge blade angle of the main inducer blade and the leading edge angle of the tandem blades [14].

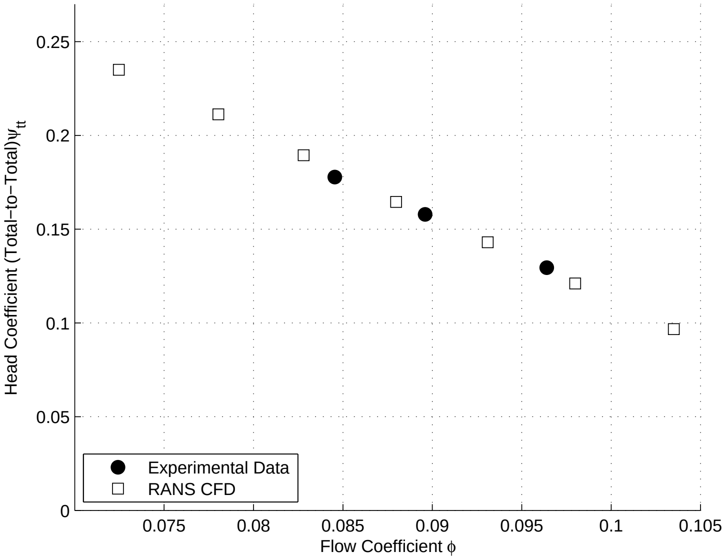

Figure 2-4: PWA inducer head rise performance

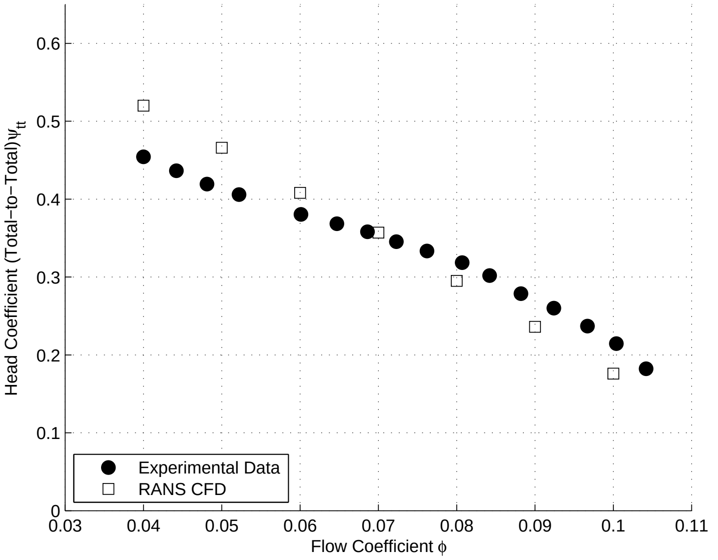

Figure 2-5: P-LPOP inducer head rise performance

## 2.3 Relevant Flow Features

The non-cavitating inducer flow fields from the single passage RANS calculations are dominated by significant upstream backflow regions created by the pressure driven tip clearance flows. These backflow regions vary dramatically in upstream extent with the head rise of the inducer, and correspondingly the flow coefficient. In the P-LPOP inducer flow field at its design flow coefficient, the backflow extends approximately one device diameter upstream, as observed in Figure 2-6. A 30% reduction in flow coefficient from the design value doubles the upstream axial penetration of the backflow, while a 40% increase from the design point entirely eliminates the backflow upstream of the inducer, though smaller backflow regions do exist within the inducer blade passage.

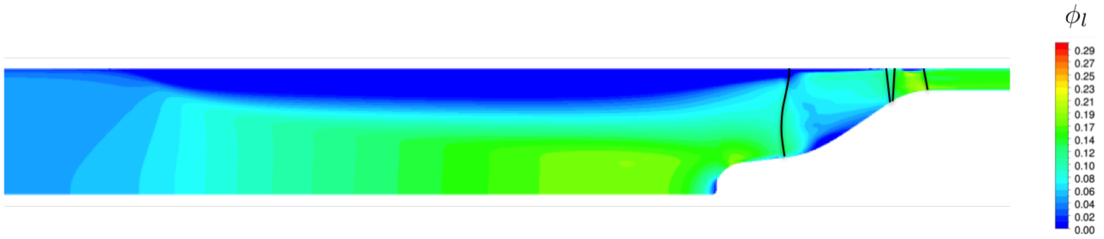

(a) Contours of pitchwise averaged axial velocity, $\phi = 0.05$

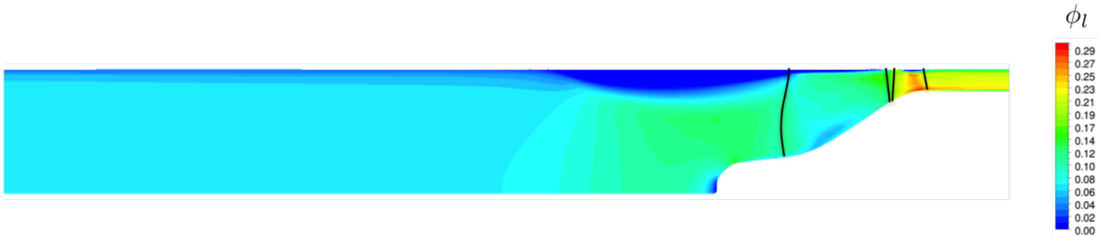

(b) Contours of pitchwise averaged axial velocity, $\phi = 0.07$

(c) Contours of pitchwise averaged axial velocity, $\phi = 0.10$

Figure 2-6: Backflow in P-LPOP inducer at various operating conditions

The large extent of these backflow regions in the P-LPOP inducer is a function of the leading edge backsweep, which acts to enlarge the effective tip clearance gap at the shroud near the lead-in edge. This can be directly observed if the P-LPOP flow field is compared to that of the PWA inducer. The axial extent of the backflow in the PWA inducer at its design flow coefficient, shown in Figure 2-7, is less than 10% of a device diameter, 90% less than the extent observed in the P-LPOP inducer.

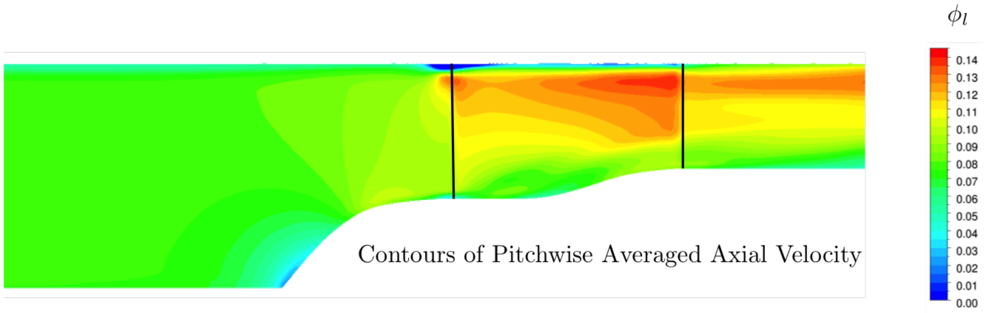

Figure 2-7: Backflow in PWA inducer, $\phi = 0.093$

The presence of backflow regions in the inducer pitchwise averaged flow field is accompanied by strong radial flows within the blade passage itself. These radial flows are a consequence of the pressure driven flow through the tip clearance; as streamlines enter the blade passage, they are shifted radially outwards and pushed back out of the passage across the backswept leading edge or through the tip clearance gap. The actual pitchwise averaged streamlines from the P-LPOP inducer at its design point are compared to the streamlines from the simple potential flow solution of the gas path in Figure 2-8. Large radial deviations can be observed in the first 30% of the chord, with the flow pitch angle reaching 90° near the leading edge above 95% span, and more than 50% of the span experiencing pitch angle deviations from the potential flow streamlines of greater than 10°.

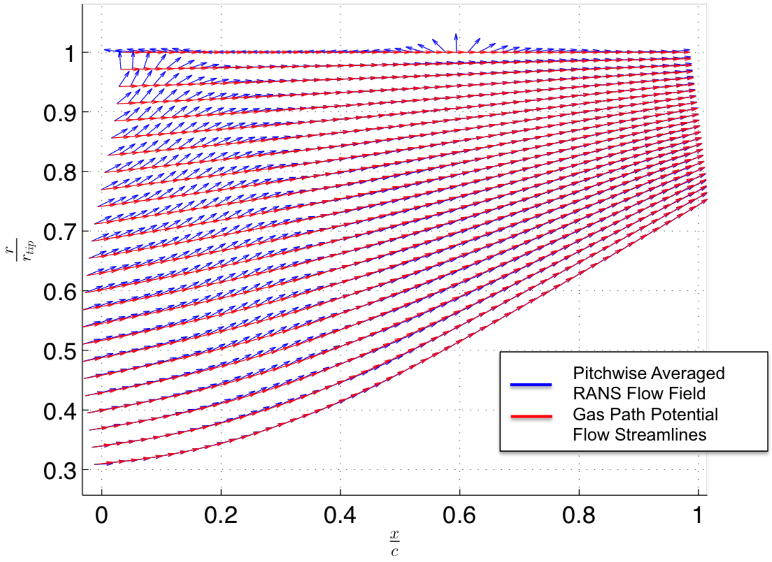

Figure 2-8: Comparison of actual pitchwise averaged meridional streamlines and gas path potential flow streamlines in main inducer blade passage ($\phi = 0.07$)

The strength of the radial flows observed in the passage scales directly with size of the tip clearance backflow region, and accordingly the device flow coefficient. Figure 2-9 presents a direct comparison of the passage radial flows at flow coefficient values 40% above and 30% below the design point. In the low flow coefficient case, shown in Figure 2-9a, when the backflow extent is double the design value, pitch angle deviations of greater than 10° occur across the entire span, compared to only 50% of the span in the design case. The high flow coefficient case, seen in Figure 2-9b, where no backflow is present upstream of the inducer, shows only 10% of the span experiences pitch angle deviations of greater than 10°. To illustrate the formation and growth of the radial flow regions, Figure 2-10 shows profiles of radial and axial velocities at 10% chord across the operating range.

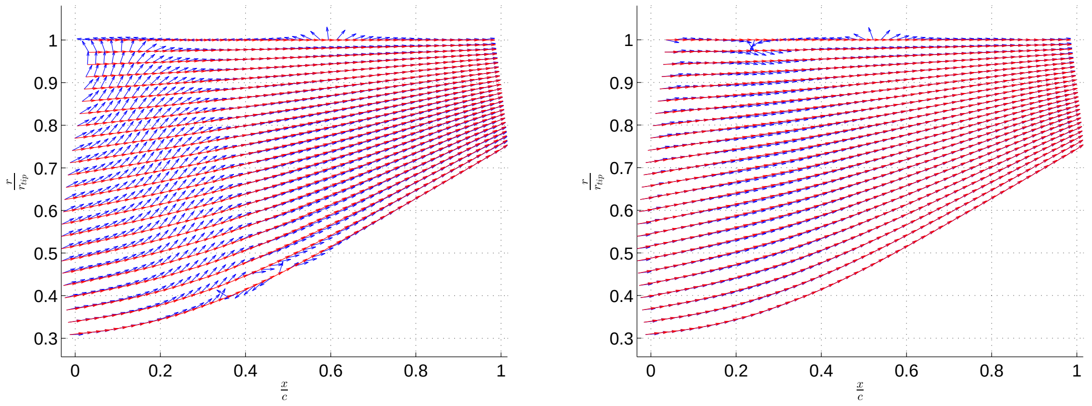

(a) $\phi = 0.05$ (b) $\phi = 0.10$

Figure 2-9: Comparison of blade passage radial flows in P-LPOP inducer above and below design flow coefficient

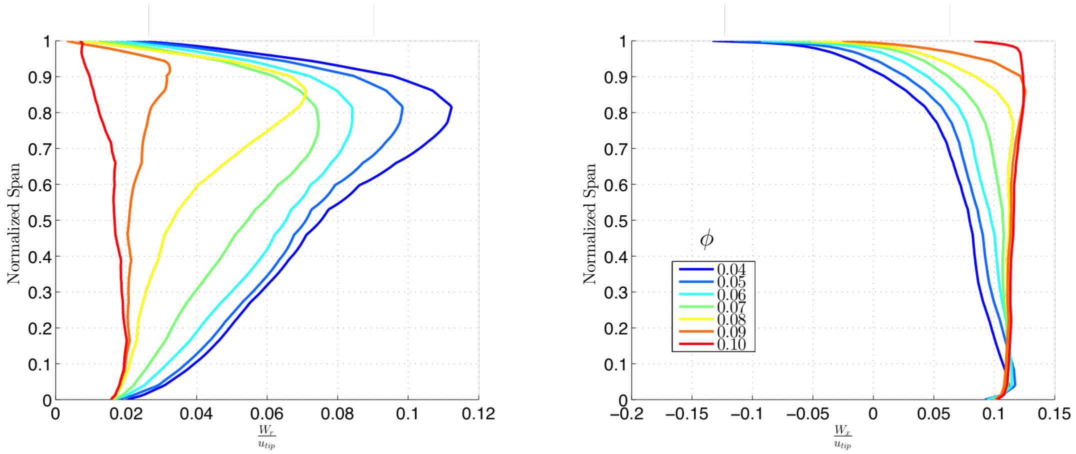

(a) Radial velocity profiles (b) Axial velocity profiles

Figure 2-10: Profiles of radial and axial velocities in P-LPOP inducer at 10% chord at various operating conditions

The blade metal blockage of the inducer also strongly impacts the pitchwise averaged flow field. The high stagger angle of the inducer blades leads to a strong cross sectional area change through the device, especially near the leading and trailing edges. The continuity equation stipulates that the area change in turn causes a proportional change in the axial velocity of the flow, and in regions of large blockage gradients the axial velocity can change significantly over short axial extents. Figure 2-11 depicts the effect of the blade metal blockage on the axial velocity distribution in the P-LPOP inducer's main blade. Both the passage free area ratio and the axial velocity are seen to change approximately 10% over less than 5% of the axial chord near leading and trailing edges.

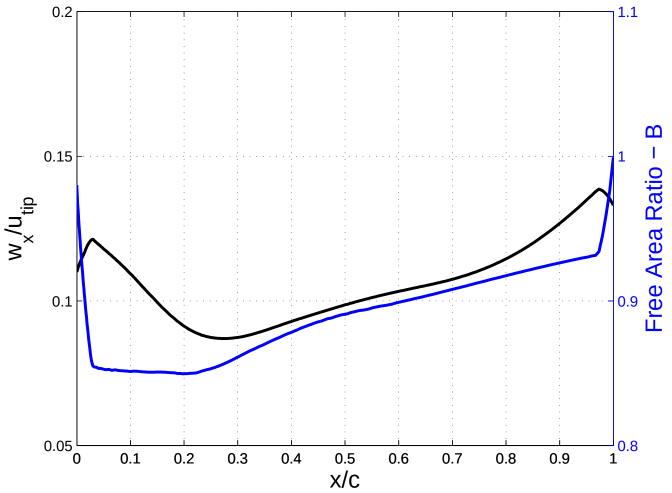

Figure 2-11: Axial velocity and passage free area ratio distributions through P-LPOP inducer main blade at midspan

The blade loading distributions of the inducer are dominated by the loading created by the incidence angle of the flow on the blades. This is manifested as a large spike in loading near the leading edge, as observed in the loading distributions from the PWA inducer and the P-LPOP inducer at their design flow coefficients shown in Figure 2-12. A secondary spike near the trailing edge is also observed and is caused by the local flow acceleration around the blade's elliptical trailing edge. The normal force distributions in the body force model closely resemble the shape of the blade loading distributions, and see the same leading edge and trailing edge spikes.

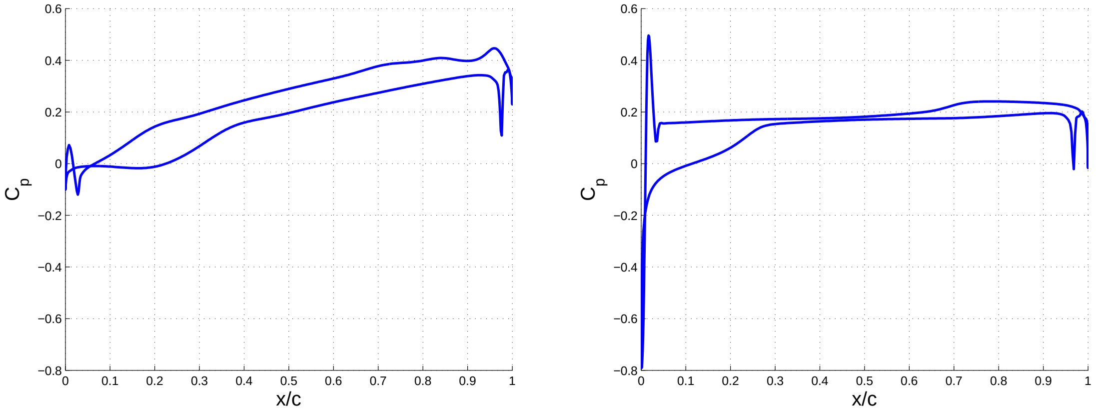

(a) P-LPOP inducer ($\phi = 0.07$)

(b) PWA inducer ($\phi = 0.093$)

Figure 2-12: Inducer midspan blade loading distributions at design conditions

## 2.4 Inducer Performance Assessment - Steady Two-Phase Calculationss

In order to assess the cavitating performance of the test inducers, single passage RANS simulations were computed using the same mesh and boundary conditions as for the single-phase case, but with ANSYS CFX's cavitation model enabled. The CFX cavitation model is developed from the Rayleigh-Plesset model for bubble formation and collapse, and is detailed in [28]. The default values of the model parameters were used. Calculations were carried out over a sweep of decreasing of cavitation numbers to identify the head breakdown point.

In order to match the operating conditions from the experimental data, the cavitating behavior of the PWA inducer was simulated at a flow coefficient below the design value, $\phi = 0.07$. The experimental head breakdown point is under predicted by approximately 10%, which is consistent with observed accuracies in the literature and in industry [18].

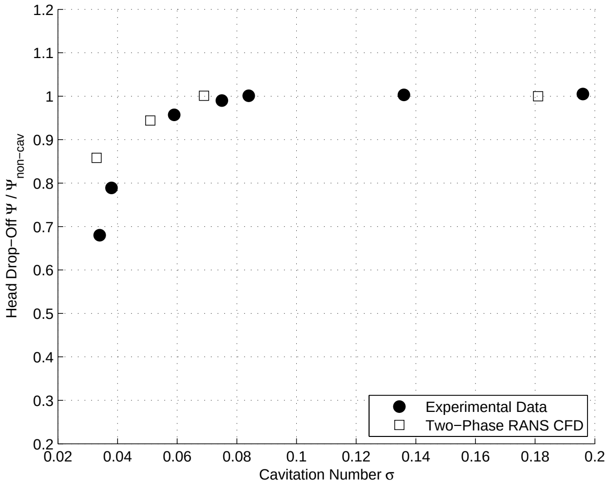

Figure 2-13: PWA inducer head loss due to cavitation, $\phi = 0.07$

The head breakdown point for the P-LPOP inducer was also computed at a flow coefficient below the design value, $\phi = 0.06$. The computational results show head breakdown beginning before it is observed in the experimental results, but the accuracy is again within that typically observed in two-phase RANS calculations.

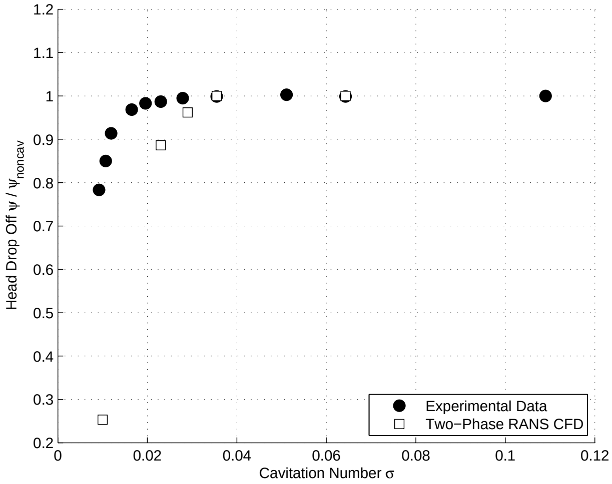

Figure 2-14: P-LPOP inducer head loss due to cavitation, $\phi = 0.07$

## 2.5 Relevant Two-Phase Flow Features

The calculated flow fields from the two-phase single passage RANS calculations are characterized by the formation of vapor cavities in local low pressure regions of the flow. In the P-LPOP inducer, these cavities occur in two distinct forms: blade cavitation, where cavities form on the suction surfaces of the inducer blades near the leading edge, and backflow cavitation, in which cavities occur in the tip clearance vortex and are convected into the upstream backflow region. The three-dimensional features of the cavities in the P-LPOP inducer at design flow coefficient for a cavitation number of $\sigma = 0.06$ are depicted in Figure 2-15.

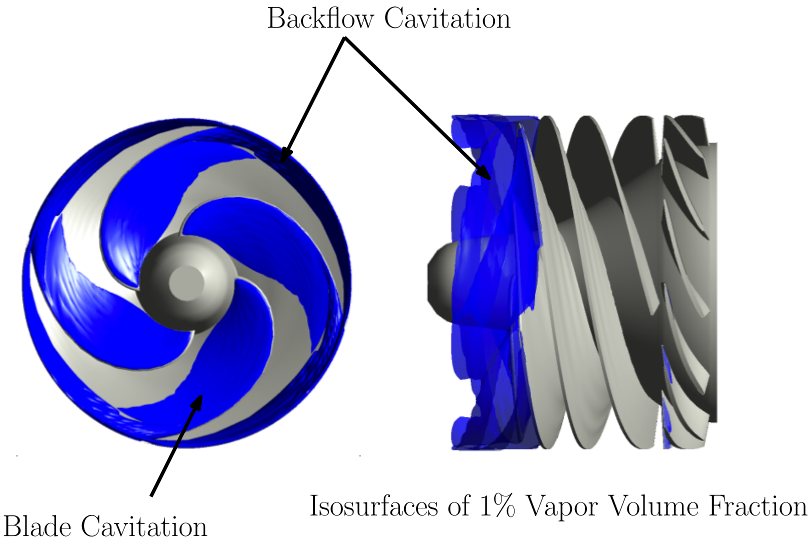

Figure 2-15: Visualization of steady cavitation in P-LPOP ($\sigma = 0.06$, $\phi = 0.07$)

In the pitchwise averaged flow field of the inducer, the presence of cavitation results in regions of non-zero pitchwise averaged vapor volume fraction, which in turn create regions of proportionally lower effective fluid density. This can be seen in the P-LPOP inducer at a cavitation number of $\sigma = 0.06$ in Figure 2-16, where backflow cavitation generates a maximum pitchwise averaged vapor volume fraction of 35% near the leading edge of the inducer at the tip, which corresponds to an effective density 35% lower than the density of the liquid phase.

The change in the effective density of the flow creates a blockage effect in addition to the blade metal blockage, altering the axial velocity of the flow. For the P-LPOP inducer at $\sigma = 0.06$, the axial velocity within the blade cavitation region increases the axial velocity magnitude of approximately 30% as compared to the non-cavitating case; the axial velocity distribution at 95 % span is shown in Figure 2-17.

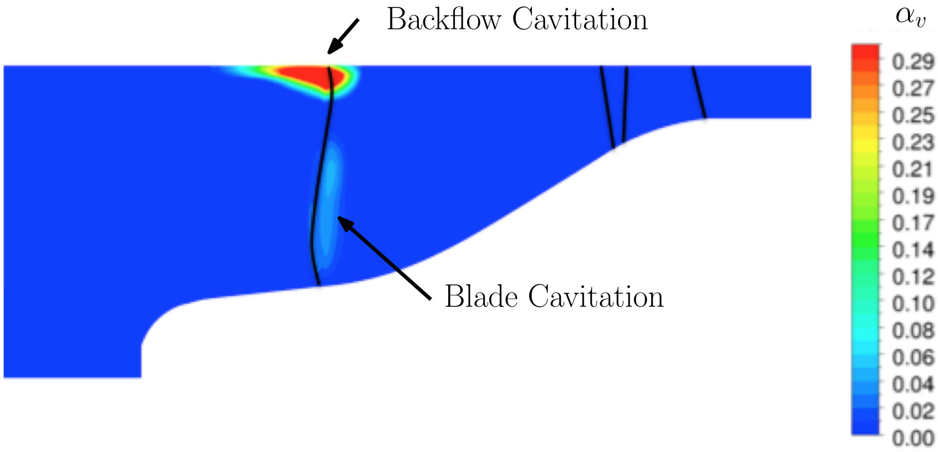

Figure 2-16: Pitchwise averaged vapor volume fraction in P-LPOP ($\sigma = 0.06$, $\phi = 0.07$)

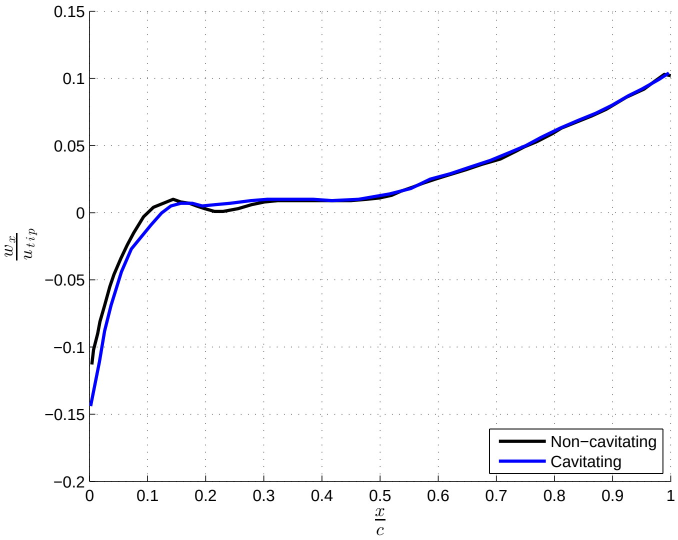

Figure 2-17: Effect of cavity blockage on axial velocity distribution at 95% span in main blade of P-LPOP inducer ($\sigma = 0.06$, $\phi = 0.07$)

Decreasing the cavitation number leads to cavity growth; Figure 2-18 depicts this process in the PWA inducer. When the cavitation number drops to $\sigma = 0.06$, blade cavitation occurs on both sides of the inducer blade due to the local overspeed of the flow around the leading edge.

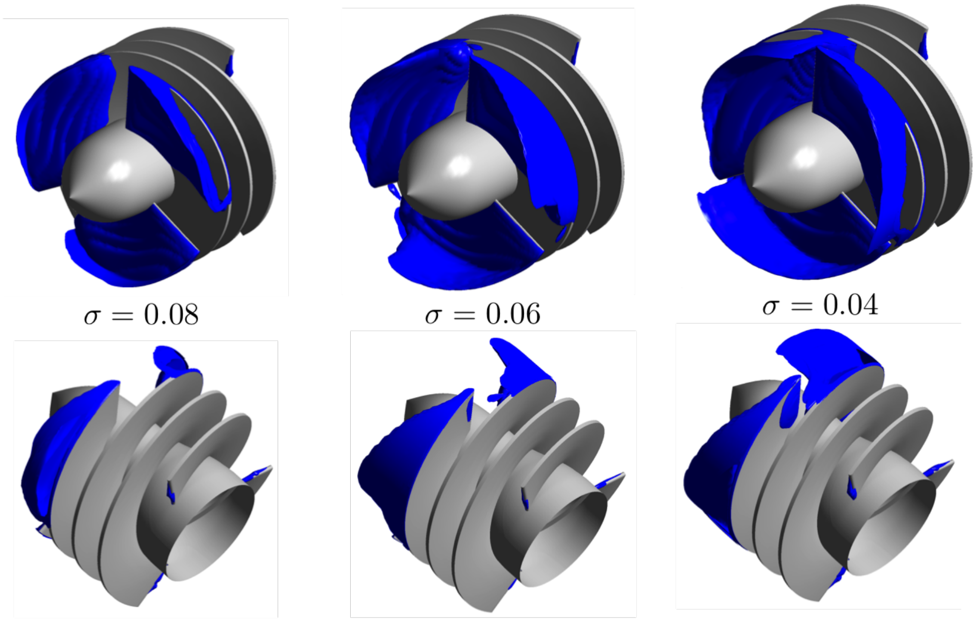

$\sigma = 0.08$ $\sigma = 0.06$ $\sigma = 0.04$

Isosurfaces of 1% Vapor Volume Fraction

Figure 2-18: Progression of steady cavitation in PWA inducer ($\phi = 0.093$)

The growth of vapor cavities on the blade surface leads to a shift in the leading edge stagnation point relative to the non-cavitating case. The PWA inducer sees a shift of approximately 8° towards the pressure side at midspan, indicating reduced incidence angle on the blades. This reduction in incidence angle alters the blade loading distributions in the inducer, attenuating the sharp spike observed at the leading edge in the non-cavitating case, as shown in Figure 2-19. The change in blade loading is directly responsible for the head drop off seen in the global performance of the inducer.

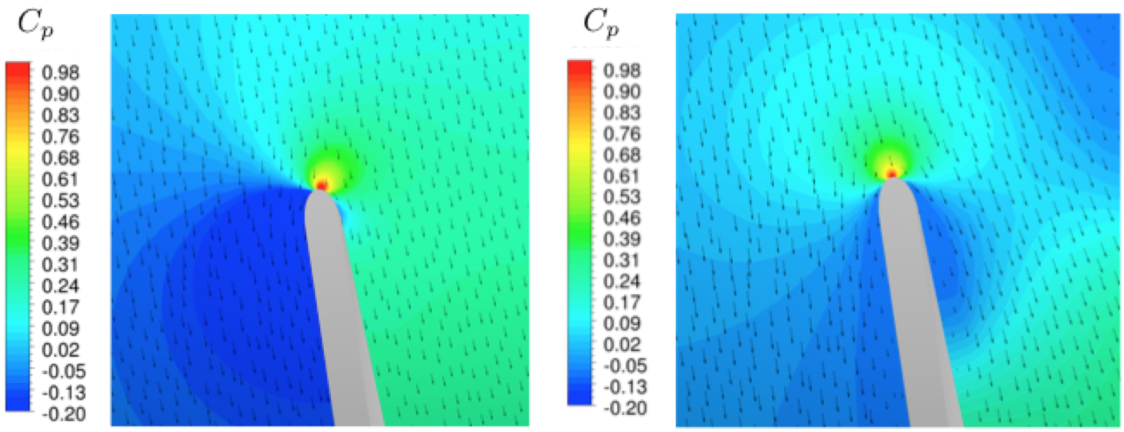

(a) non-cavitating case, $\sigma = 1.0$ (b) Cavitating case, $\sigma = 0.04$

Figure 2-19: Leading edge stagnation point shift due to cavitation in PWA inducer at midspan

## 2.6 Body Force Model Requirements

In previous body force model formulations, the most critical steady flow features to be captured were the correct flow turning and losses within the blade passage, and the accuracy of the local flow field was treated as secondary, with significant assumptions made about its behavior [13]. However, the observed sensitivity of rotating cavitation instabilities to the flow field near the leading edge at the tip suggests that the body force model must reproduce that flow field accurately in order to correctly capture the mechanisms which govern rotating cavitation. Given the significant changes in axial velocity associated with the blade metal blockage at the leading edge, the effect of the blade metal blockage must be accounted for to ensure the the body force model captures the leading edge flow field accurately.

When simulating an inducer operating under cavitating conditions, the body force model must capture the axial velocity and density changes created by the cavity blockage. The model must also recreate the reduced blade loading near the leading edge and the resultant global head drop off caused by the shift in the leading edge stagnation point location.

# Chapter 3

# A Body Force Model for Cavitating Inducers

## 3.1 Model Objectives and Assumptions

The primary objective of the body force model is to recreate the pitchwise averaged flow field of an inducer in a steady, axisymmetric calculation, including all of the relevant flow features observed in the non-cavitating single passage RANS calculations. The model should contain a link between the forces applied and the local field to allow the flow to respond to perturbations in unsteady calculations.

The framework of the body force model is given in Figure 3-1. There are two key elements to the model, the force extraction process and the blade passage model. The force extraction process calculates the forces that the discrete blades in the inducer place on the flow based on a single passage RANS calculation. The blade passage model consists of component models for each force component which provide the desired link between the force and the local flow field, along with a model to capture effect of blockage produced by the physical blades. The blade passage model is implemented as mass and momentum source terms within the commercial CFD solver ANSYS CFX.

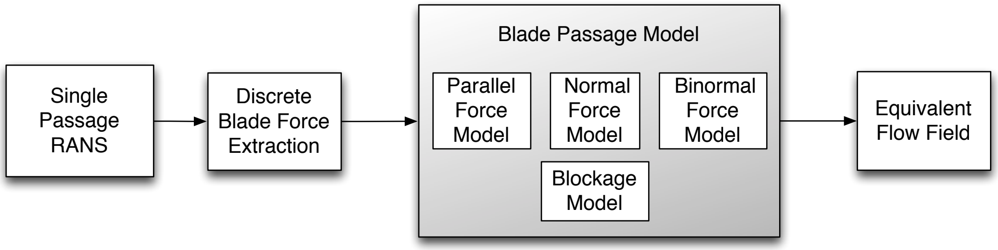

Figure 3-1: Body force model framework

While previous body force model formulations only used the normal and parallel forces, an additional third force component, the binormal force, is included in the blade passage model to capture the strong radial flows observed in the inducer pitchwise averaged flow fields. Just as the normal and parallel forces are applied in the corresponding natural coordinate direction, the binormal force is applied to the flow in the binormal direction.

The formulation of the body force model assumes the flow is quasi-steady and incompressible, with adiabatic boundaries and no volumetric heat sources. The flow is also assumed to be inviscid, with the viscous effects of the blade and wall boundary layers captured in the parallel force component of the model.

## 3.2 Model Coordinate System and Governing Equations

The model is formulated in a natural coordinate system aligned with the streamlines of the flow, consisting of three orthogonal coordinates, $l$, $n$, and $h$. Two planes are used to define the coordinate system, the meridional plane of the device as well as a stream surface which is orthogonal to the meridional plane and tangent to the meridional projection of the streamlines. These surfaces are depicted together in Figure 3-2, and individually in Figures 3-3a and 3-3b.

The relative flow angle, which is the angle the streamline direction forms with the meridional direction $\hat{\mathbf{m}}$, is denoted $\beta$. The unit vector $\hat{\mathbf{n}}$ is always normal to the streamline direction on the stream surface. The unit vector $\hat{\mathbf{h}}$ is normal to both $\hat{\mathbf{l}}$ and

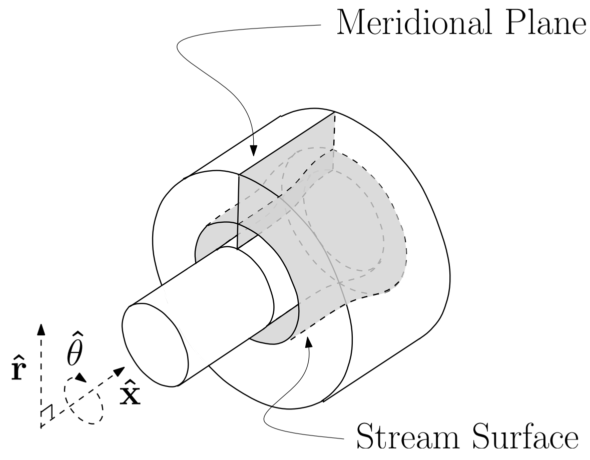

Figure 3-2: Natural coordinate planes

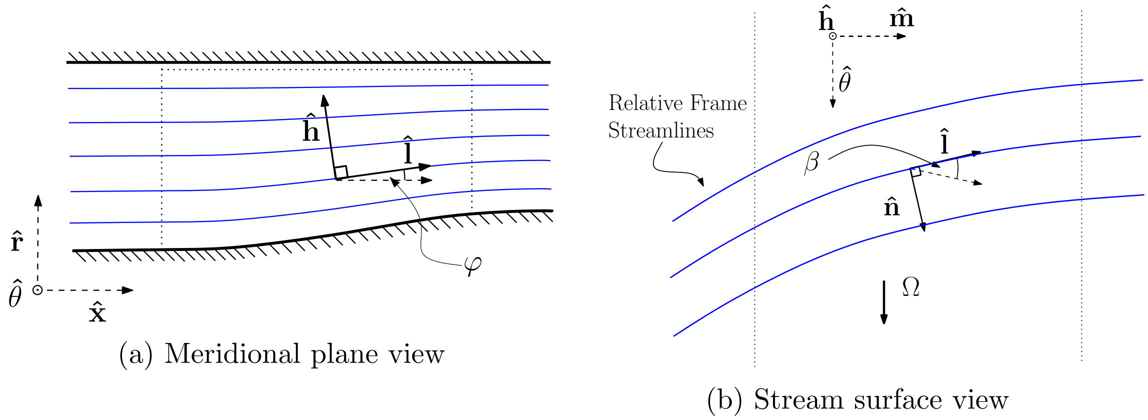

(a) Meridional plane view

(b) Stream surface view

Figure 3-3: Natural coordinate plane views

$\hat{\mathbf{n}}$, and so is referred to as the binormal direction. The angle between the binormal axis and the radial axis is the pitch angle of the flow and is denoted $\varphi$.

$$\varphi = \arctan\left(\frac{u_r}{u_x}\right) \quad \beta = \arctan\left(\frac{u_\theta - \Omega r}{\sqrt{{u_x}^2 + {u_r}^2}}\right) \tag{3.1}$$

As the flow is assumed incompressible, only the mass continuity and momentum conservation equations are necessary, and the energy conservation equation can be neglected. The model is formulated in the relative frame of the inducer, so fictitious centrifugal and coriolis force terms must be included.

$$\nabla \cdot \mathbf{w} = 0 \tag{3.2}$$

$$(\mathbf{w} \cdot \nabla)\mathbf{w} = -\frac{1}{\rho}\nabla p - \boldsymbol{\Omega} \times (\boldsymbol{\Omega} \times \mathbf{r}) - 2(\boldsymbol{\Omega} \times \mathbf{w}) \tag{3.3}$$

The momentum equations must be formulated in the model's natural coordinate system. The full derivation is presented in Appendix A; the final equations are given below.

$$\mathbf{l}:\ w\frac{\partial w}{\partial l} = -\frac{1}{\rho}\frac{\partial p}{\partial l} + \Omega^2 r \sin\varphi \cos\beta \tag{3.4}$$

$$\mathbf{n}:\ -w^2\frac{\partial \beta}{\partial l} - w^2 \sin\varphi \frac{\sin\beta}{r} = -\frac{1}{\rho}\frac{\partial p}{\partial n} + \Omega^2 r \sin\beta \sin\varphi + 2\Omega w \sin\varphi \tag{3.5}$$

$$\mathbf{h}:\ w^2 \cos\beta \frac{\partial \varphi}{\partial l} - w^2 \cos\varphi \frac{\sin^2\beta}{r} = -\frac{1}{\rho}\frac{\partial p}{\partial h} + \Omega^2 r \cos\varphi + 2\Omega w \cos\varphi \sin\beta \tag{3.6}$$

## 3.3 Force Extraction Process

### 3.3.1 Blade Force Average Approach to Force Extraction

The concept of the blade force average, as described by Kiwada [12] and Peters [17], is used to define and to extract the force components. Beginning with the governing equations, the blade force average preserves the forces the blade imparts on the fluid on a pitchwise average basis. Consider the momentum equation in the normal direction

$$-w^2\frac{\partial \beta}{\partial l} - w^2 \sin\varphi \frac{\sin\beta}{r} + \frac{1}{\rho}\frac{\partial p}{\partial n} - \Omega^2 r \sin\beta \sin\varphi - 2\Omega w \sin\varphi = 0\,. \tag{3.7}$$

For a non-axisymmetric flow the pitchwise average of this expression yields

$$\overline{-w^2\frac{\partial\beta}{\partial l} - w^2\sin\varphi\frac{\sin\beta}{r} + \frac{1}{\rho}\frac{\partial p}{\partial n} - \Omega^2 r\sin\beta\sin\varphi - 2\Omega w\sin\varphi} = 0\,. \tag{3.8}$$

The expression being averaged is non-linear (for example, $\overline{x^2} \neq \overline{x}^2$), and the above can be written in terms of the pitchwise averaged flow field as

$$-\overline{w}^2\frac{\partial\overline{\beta}}{\partial\overline{l}} - \overline{w}^2\sin\overline{\varphi}\frac{\sin\overline{\beta}}{r} + \frac{1}{\rho}\frac{\partial\overline{p}}{\partial\overline{n}} - \Omega^2 r\sin\overline{\beta}\sin\overline{\varphi} - 2\Omega\overline{w}\sin\overline{\varphi} + \sum(H.O.T.s) = 0\,, \tag{3.9}$$

where H.O.T. denotes higher order non-axisymmetric terms. For an axisymmetric flow field, the higher order terms sum to zero, such that if present they directly account for the circumferential non uniformity in the flow field. Since this non-uniformity is caused by the presence of the blades in the flow, the higher order terms provide a direct definition of the body forces (the negative sign preserves the natural coordinate definitions):

$$\sum(H.O.T.s) = -f_n\,, \tag{3.10}$$

or

$$f_n = -\overline{w}^2\frac{\partial\overline{\beta}}{\partial\overline{l}} - \overline{w}^2\sin\overline{\varphi}\frac{\sin\overline{\beta}}{r} + \frac{1}{\rho}\frac{\partial\overline{p}}{\partial\overline{n}} - \Omega^2 r\sin\overline{\beta}\sin\overline{\varphi} - 2\Omega\overline{w}\sin\overline{\varphi}\,. \tag{3.11}$$

The blade force average can also be applied to the governing equations in the parallel and binormal directions to define the force components in the those directions. The resulting parallel force definition becomes

$$f_l = \overline{w}\frac{\partial \overline{w}}{\partial \overline{l}} + \frac{1}{\rho}\frac{\partial \overline{p}}{\partial \overline{l}} - \Omega^2 r \sin\overline{\varphi}\cos\overline{\beta}\,. \tag{3.12}$$

Similarly, the binormal force is defined as

$$f_h = \overline{w}^2 \cos\overline{\beta}\frac{\partial \overline{\varphi}}{\partial \overline{l}} - \overline{w}^2\cos\overline{\varphi}\frac{\sin^2\overline{\beta}}{r} + \frac{1}{\rho}\frac{\partial \overline{p}}{\partial \overline{h}} - \Omega^2 r\cos\overline{\varphi} - 2\Omega\overline{w}\cos\overline{\varphi}\sin\overline{\beta}\,. \tag{3.13}$$

The force definitions can be used directly to extract the blade forces from non-cavitating single passage RANS calculations for use in the body force model. Using the geometry of a given blade row, an extraction grid of $x$, $r$ locations where the force is to be computed is created. The grid is refined around the leading and trailing edges in order to capture the blade loading concentrations observed near the leading and trailing edges. The extraction grids used to extract the forces from the P-LPOP inducer main blade and tandem blade are shown in Figure 3-4.

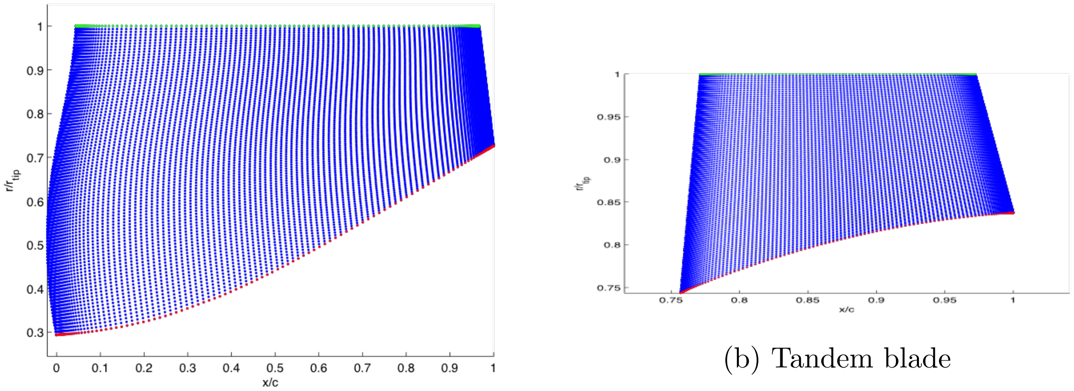

(b) Tandem blade

(a) Main inducer blade

Figure 3-4: Body force extraction grids for P-LPOP blade rows

The geometry of the blade near the leading edge and trailing edge must treated carefully. Due to the high stagger angles of the inducer blades, the axial location of the leading edge can be beyond the axial extent of the camber line of the blade, as depicted in Figure 3-5. Though the blade geometry is most often defined using the camber surface, in order to capture the forces near the leading edge correctly the first extraction grid point must be placed at the actual leading edge location, not the camber line leading edge location.

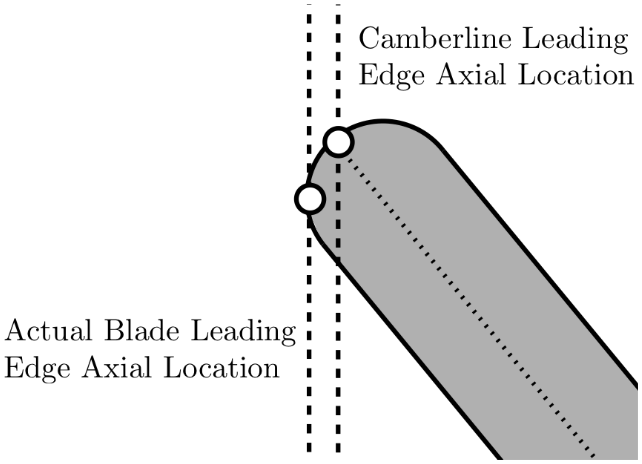

Figure 3-5: Extraction grid leading edge geometry

At each grid point, the required pitchwise averaged flow field quantities are calculated using an area average, and the forces are computed based on the above definitions. The pressure gradient terms require the gradients of the pitchwise averaged pressure field, which are computed using a second order finite difference approximation.

Using the force extraction process, force distributions for the P-LPOP inducer were calculated from the single passage RANS calculations. The force distributions were used to characterize the inducer performance and flow field at flow coefficients spanning the operating range of the inducer.

### 3.3.2 Extracted Force Component Distributions

The normal force distributions capture the shape of the observed blade loading distributions, including the sharp spikes near the leading and trailing edges. As the inducer flow coefficient decreases, the head rise of the inducer increases, driven by a change in the incidence angle of the flow. The normal force distributions capture this change in incidence angle and loading, as seen in the higher force magnitudes in the first 30% of the blade. Downstream, the effect of the incidence angle on the flow has subsided, and the normal force distributions show little variation in magnitude.

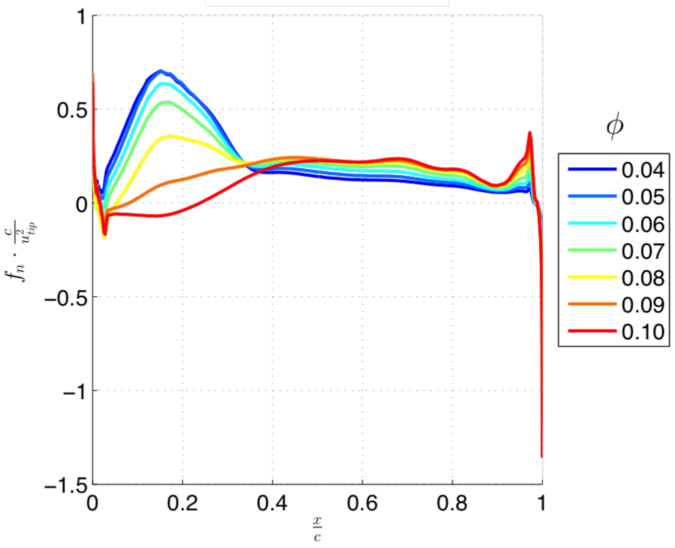

Figure 3-6: Extracted normal force streamwise distributions at midspan

The calculated parallel force distributions at midspan are largely negative; as the parallel force captures the viscous losses in the flow, it takes negative values across the bulk of the inducer in order to decreases the pressure rise. Near the leading and trailing edges, the parallel force also captures a component of the effect of the local acceleration of the flow around edges of the blade, leading to large force spikes. In comparison with the normal force, the parallel force is an order of magnitude smaller over the bulk of the domain, indicating that the normal force drives the flow behavior.

The binormal force distributions have magnitudes comparable to the value of the normal force in regions where strong radial flows are observed in the pitchwise averaged single passage flow fields, most notably near the shroud at the leading edge where the backflow regions are located. The distributions show the same strong dependence on the operating conditions of the inducer as the radial flow features, diminishing in magnitude at high flow coefficients when the backflow region is minimal and the flow largely follows the potential flow streamlines.

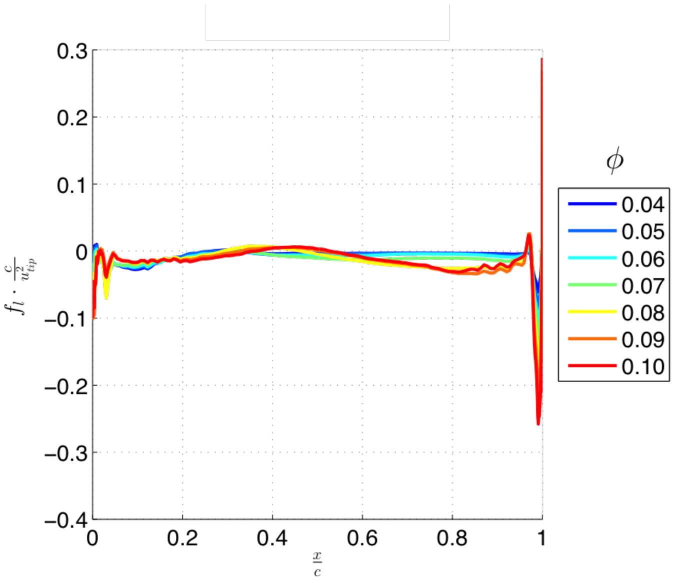

Figure 3-7: Extracted parallel force streamwise distributions at midspan

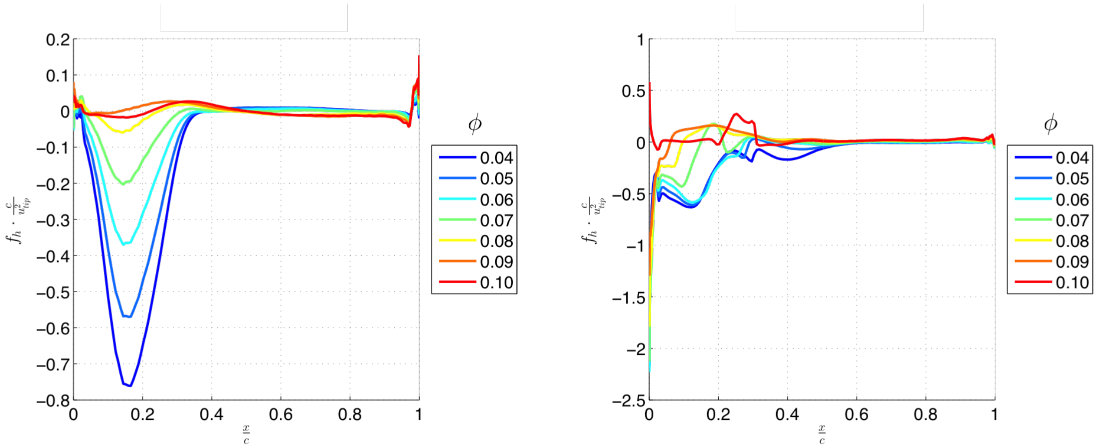

(a) Distributions at midspan

(b) Distributions near shroud (95% Span)

Figure 3-8: Binormal force streamwise distributions in P-LPOP inducer main blade

### 3.3.3 Impact of Alternate Pitchwise Averaging Methods

In the force extraction process an area average was used to calculate the required pitchwise averaged quantities used to compute the force components, but the other averaging methods could be used. Application of the mass flow average, as used in previous body force model formulations [2, 13, 1], was investigated during the development of the body force model, but was found to produce spurious results around the backflow regions seen in the inducer. On the boundary points of the backflow region, the denominator of the mass flow average expression approaches zero and a singularity is created.

$$\overline{q}_{MFA} = \frac{\int \rho w_x q d\theta}{\int \rho w_x d\theta} \tag{3.14}$$

In other applications of the body force model methodology, the use of the mass flow average may be advantageous by improving the capture of the device performance, as it properly bookkeeps the entropy flux in the flow [6], but it can only be used provided no pitchwise averaged backflow regions exist in the flow field.

## 3.4 Single Phase Blade Passage Model

The blade passage model consists of three force component models and a model which accounts for the blade metal blockage. Each force component model is derived from the governing equation in the corresponding direction, and contains an empirical term which captures the information about the blade forces as extracted from the single passage RANS calculations and is formulated with a clear physical interpretation.

### 3.4.1 Normal Force Model

The normal force model is derived from the governing equation in the normal direction as applied to a body force calculation, which now includes a body force term. Note, a $\hat{q}$ is used to denote a quantity in the body force calculation, as opposed the $\bar{q}$ which represents a quantity obtained by pitchwise averaging a single passage RANS calculation. First, a connection to the geometry of the inducer is introduced. It is assumed that the relative flow angle $\hat{\beta}$ can be decomposed into the sum of the physical blade metal angle of the blade and a deviation angle $\delta_\beta$ which captures the net deviation of the pitchwise averaged flow from the blade metal angle.

$$\hat{\beta} = \kappa + \delta_\beta \tag{3.15}$$

This expression can be substituted into the governing equation to create two new terms.

$$\hat{f}_n = -\hat{w}^2 \left( \frac{\partial \kappa}{\partial \hat{l}} + \frac{\partial \delta_\beta}{\partial \bar{l}} \right) - \hat{w}^2 \sin \hat{\varphi} \frac{\sin \hat{\beta}}{r} + \frac{1}{\rho} \frac{\partial \hat{p}}{\partial \hat{n}} - \Omega^2 r \sin \hat{\beta} \sin \hat{\varphi} - 2\Omega \hat{w} \sin \hat{\varphi} \tag{3.16}$$

The geometry term $\frac{\partial \kappa}{\partial \hat{l}}$, can be expanded to contain two quantities dependent only on the geometry of the inducer. These are the axial and radial gradients of the blade metal angle, which are known a priori.

$$\frac{\partial \kappa}{\partial \hat{l}} = \left( \frac{\partial \kappa}{\partial x} \cos \hat{\varphi} + \frac{\partial \kappa}{\partial r} \sin \hat{\varphi} \right) \cos \hat{\beta} \tag{3.17}$$

The relative flow angle deviation gradient $\frac{\partial \delta_\beta}{\partial \bar{l}}$ captures external information about the forces to be applied to the flow. This information can come from correlations of experimental data, streamline curvature analyses, or, as in this research, from single passage RANS calculations. Physically, it represents the rate of change of the deviation of the flow from the blade metal angle, which may be driven by incidence effects or the growth of viscous boundary layers on the blades. $\bar{l}$ is used to indicate that the value of the term is calculated from single passage RANS data. The expression for the normal force model then becomes

$$\begin{aligned}\hat{f}_n = &- \hat{w}^2 \left( \left( \frac{\partial \kappa}{\partial x} \cos \hat{\varphi} + \frac{\partial \kappa}{\partial r} \sin \hat{\varphi} \right) \cos \hat{\beta} + \frac{\partial \delta_\beta}{\partial \bar{l}} \right) - \hat{w}^2 \sin \hat{\varphi} \frac{\sin \hat{\beta}}{r} \\ &+ \frac{1}{\rho} \frac{\partial \hat{p}}{\partial \hat{l}} - \Omega^2 r \sin \hat{\beta} \sin \hat{\varphi} - 2\Omega \hat{w} \sin \hat{\varphi}\end{aligned} \tag{3.18}$$

The two geometry terms and the relative flow angle deviation gradient are the inputs to the model. The force is calculated from those inputs and the local flow field quantities $\hat{w}$, $\hat{\varphi}$, $\hat{\beta}$, and $\frac{\partial \hat{p}}{\partial \hat{n}}$, creating the desired link between the force and the local flow field.

### Modification to Prevent Numerical Instability

Brand [2] and Kottapalli [13] identified a numerical instability caused by a positive feedback loop between the pressure gradient term and the normal force. This instability was eliminated through the use of a control volume analysis of axisymmetric swirling flow to determine the influence coefficients which related the local velocity field to the pressure gradient. The pressure gradient term in the original model was rewritten in terms of the velocity field using those influence coefficients. A similar approach is taken here, with the final result presented below, and the full details of the analysis provided in Appendix B. The offset term $K_{off}$ is used to prevent singularities when the relative flow angle approaches 90°, and does not change the model behavior as long as it is consistently implemented in both calculation of the relative flow angle deviation gradient term and the final normal force model expression.

$$\begin{aligned}\hat{f}_n = \Bigg[ &- \hat{w}^2 \left( \left( \frac{\partial \kappa}{\partial x} \cos \hat{\varphi} + \frac{\partial \kappa}{\partial r} \sin \hat{\varphi} \right) \cos \hat{\beta} + \frac{\partial \delta_\beta}{\partial \bar{l}} \right) - 2\hat{w}^2 \sin \hat{\varphi} \frac{\sin \hat{\beta}}{r} \\ &- 2\Omega^2 r \sin \hat{\beta} \sin \hat{\varphi} - 2\Omega \hat{w} \sin \hat{\varphi} (1 + \sin^2 \hat{\beta}) - \hat{f}_l \sin \beta \cos \beta \Bigg] \frac{1}{1 - \sin^2 \hat{\beta} + K_{off}}\end{aligned} \tag{3.19}$$

**Determination of Relative Flow Angle Deviation Gradient**

The values of the relative flow angle deviation gradient are calculated by rearranging the normal force model expression and inserting the forces $f_n$ and $f_l$ extracted from the single passage RANS calculations, along with the pitchwise averaged flow field data, $\overline{w}$, $\overline{\varphi}$, and $\overline{\beta}$.

$$\begin{aligned}\frac{\partial \delta_\beta}{\partial \bar{l}} = &-\frac{1}{\overline{w}^2}\Big[f_n(1-\sin^2\overline{\beta}+K_{off}) + 2\overline{w}^2\sin\overline{\varphi}\frac{\sin\overline{\beta}}{r} + 2\Omega^2 r\sin\overline{\beta}\sin\overline{\varphi} \\ &+ 2\Omega\overline{w}\sin\overline{\varphi}(1+\sin^2\overline{\beta}) + f_l\sin\beta\cos\beta\Big] - \left(\frac{\partial\kappa}{\partial x}\cos\overline{\varphi} + \frac{\partial\kappa}{\partial r}\sin\overline{\varphi}\right)\cos\overline{\beta}\end{aligned} \tag{3.20}$$

The calculated distributions of the relative flow angle deviation gradient show similar trends to the normal force distributions from which they are calculated, as observed in the midspan distributions in Figure 3-9. The loading spikes from the leading and trailing edges are captured in the $\frac{\partial \delta_\beta}{\partial \bar{l}}$ distributions as well, as the deviation of the flow from the blade metal angle is rapidly changing in those regions, turning to match the blade angle near the leading edge and correcting as the blades end near the trailing edge. Outside of the incidence affected region of the blade, the gradient takes similar values under all operating conditions as the growth of the boundary layers on the blades occurs at similar rates.

## 3.4.2 Parallel Force Model

The parallel force is derived from the momentum equation in the streamwise direction.

$$\hat{f}_l = \hat{w}\frac{\partial \hat{w}}{\partial \hat{l}} + \frac{1}{\rho}\frac{\partial \hat{p}}{\partial \hat{l}} - \Omega^2 r\sin\hat{\varphi}\cos\hat{\beta} \tag{3.21}$$

By combining Equation 3.21 and the Gibbs equation, it can be shown that the inertial and pressure gradient terms represent the entropy gradient in the parallel

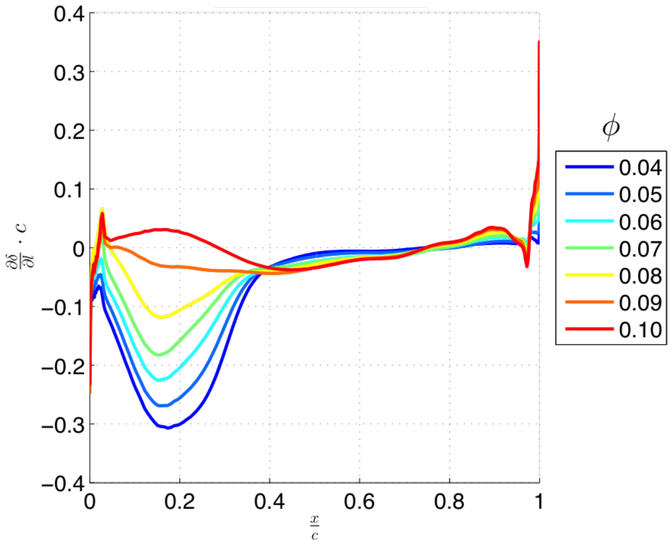

Figure 3-9: Calculated streamwise distributions of the relative flow angle deviation gradient at midspan

direction.

$$\hat{f}_l = -T\frac{\partial \hat{s}}{\partial \hat{l}} - \Omega^2 r \sin\hat{\varphi}\cos\hat{\beta} \tag{3.22}$$

To introduce an empirical term into the parallel force model, the parallel direction entropy gradient is rewritten in terms of the meridional entropy gradient. The meridional entropy gradient $\frac{\partial \overline{s}}{\partial \overline{m}}$ is used directly as the empirical term for the model, and captures the viscous entropy generation in the flow. The final expression for the parallel force model is given below.

$$\hat{f}_l = -T\frac{\partial \overline{s}}{\partial \overline{m}}\cos\hat{\beta} - \Omega^2 r \sin\hat{\varphi}\cos\hat{\beta} \tag{3.23}$$

### Determination of the Meridional Entropy Gradient

The meridional entropy gradient $\frac{\partial \overline{s}}{\partial \overline{m}}$ is determined in the same manner as the normal force, by manipulating the parallel force model expression and substituting the

the force $f_l$ as extracted from a single passage RANS calculation and the pitchwise averaged flow field quantities $\overline{\varphi}$ and $\overline{\beta}$.

$$\frac{\partial \overline{s}}{\partial \overline{m}} = -\left(f_l + \Omega^2 r \sin \overline{\varphi} \cos \overline{\beta}\right) \frac{1}{T \cos \overline{\beta}} \tag{3.24}$$

The calculated meridional entropy distributions capture the behavior of the parallel force distributions, as seen in the distributions calculated for the P-LPOP inducer in Figure 3-10.

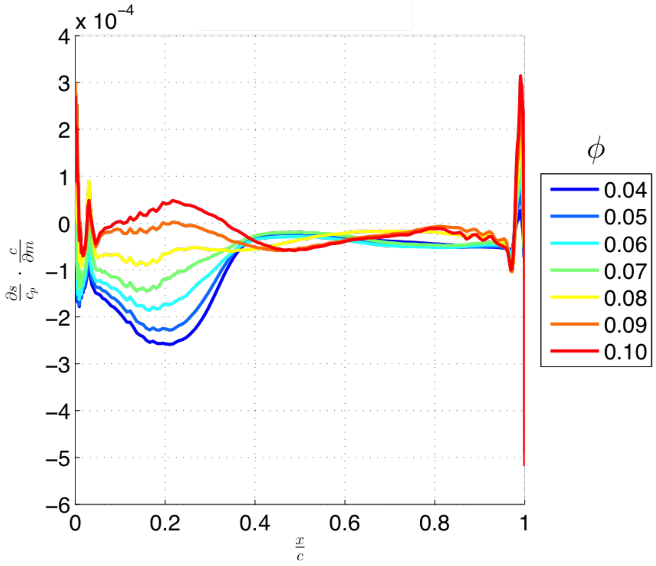

Figure 3-10: Calculated streamwise distributions of the meridional entropy gradient at midspan

### 3.4.3 Binormal Force Model

The binormal force model is derived from the governing equation in the binormal direction using a similar approach to the normal force model. The link to the geometry of the inducer is introduced by decomposing the pitch angle into the geometric gas path angle (defined as the angle of the potential flow streamline at that $x$,$r$ location) and the deviation of the flow from that angle.

$$\hat{\varphi} = \varphi_{GP} + \delta_{\varphi} \tag{3.25}$$

This expression can then be substituted into the governing equation, with geometry term being broken down further into two quantities that are known a priori, the axial and radial gradients of the geometric gas path angle. Just as for the normal force, the new term, the pitch angle deviation gradient, is used as the empirical term within the model. The pitch angle deviation gradient captures the rate of change of the deviation of the flow from the geometric gas path angle, which is caused primarily by the pressure driven radial flows observed in the inducer flow fields.

$$\begin{aligned} \hat{f}_h = {} & \hat{w}^2 \cos\hat{\beta} \left( \left( \frac{\partial \varphi_{GP}}{\partial x} \cos\hat{\varphi} + \frac{\partial \varphi_{GP}}{\partial r} \sin\hat{\varphi} \right) \cos\hat{\beta} + \frac{\partial \delta_{\varphi}}{\partial \bar{l}} \right) - \hat{w}^2 \cos\hat{\varphi} \frac{\sin^2\hat{\beta}}{r} \\ & + \frac{1}{\rho} \frac{\partial \hat{p}}{\partial \hat{h}} - \Omega^2 r \cos\hat{\varphi} - 2\Omega \hat{w} \cos\hat{\varphi} \sin\hat{\beta} \end{aligned} \tag{3.26}$$

The binormal force model is modified in the same manner as the normal force to prevent the appearance of a numerical instability involving the pressure gradient term. The final binormal force model expression with the pressure gradient recast in terms of the velocity field is given below. No offset term is needed for the binormal force, as the potential for singularities does not occur in the expression.

$$\begin{aligned} \hat{f}_h = {} & \hat{w}^2 \cos\hat{\beta} \left( \left( \frac{\partial \varphi_{GP}}{\partial x} \cos\hat{\varphi} + \frac{\partial \varphi_{GP}}{\partial r} \sin\hat{\varphi} \right) \cos\hat{\beta} + \frac{\partial \delta_{\varphi}}{\partial \bar{l}} \right) - \hat{w}^2 \cos\hat{\varphi} \frac{1 + \sin^2\hat{\beta}}{r} \\ & - 2\Omega^2 r \cos\hat{\varphi} - 4\Omega \hat{w} \cos\hat{\varphi} \sin\hat{\beta} \end{aligned} \tag{3.27}$$

### Determination of the Pitch Angle Deviation Gradient

The values of the pitch angle deviation gradient are determined by the same method as the empirical terms for the normal and parallel forces. The binormal force model expression is rearranged to isolate $\frac{\partial \delta_\varphi}{\partial \bar{l}}$, and the force $f_h$ extracted from the single passage RANS calculations, along with the pitchwise averaged flow field data, $\overline{w}$, $\overline{\varphi}$, and $\overline{\beta}$, is used to calculate the pitch angle deviation gradient.

$$
\begin{aligned}
\frac{\partial \delta_\varphi}{\partial \bar{l}} = &\left[ f_h + \overline{w}^2 \cos\overline{\varphi} \frac{1+\sin^2\overline{\beta}}{r} + 2\Omega^2 r \cos\overline{\varphi} + 4\Omega\overline{w}\cos\overline{\varphi}\sin\overline{\beta} \right] \frac{1}{\overline{w}^2 \cos\overline{\beta}} \\
&- \left( \frac{\partial \varphi_{GP}}{\partial x}\cos\overline{\varphi} + \frac{\partial \varphi_{GP}}{\partial r}\sin\overline{\varphi} \right)\cos\overline{\beta}
\end{aligned}
\tag{3.28}
$$

The calculated distributions of the pitch angle deviation gradient display the same trends as the binormal force. As the inducer flow coefficient increases, the magnitude of the pitch angle deviation gradient decreases across the entire chord, as the strength of the radial flows seen in the single passage calculations decreases.

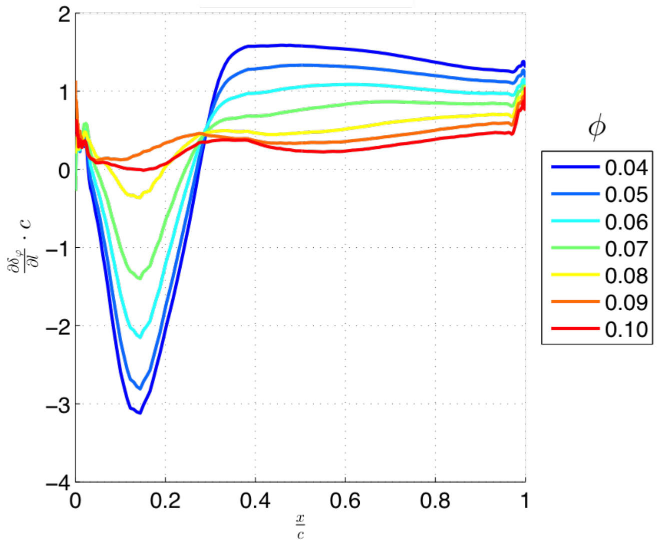

Figure 3-11: Calculated streamwise distributions of the pitch angle deviation gradient at midspan

### 3.4.4 Blade Metal Blockage Model

The blade metal blockage model implemented as part of the blade passage model was first derived by Benneke [1]. It is derived from an analysis of the impact of the change in passage cross sectional area on the pitchwise average process; the full derivation may be found in [1] or [13]. The model is defined in terms of the passage free area ratio $B$, where $t$ is the blade thickness normal to its camberline.

$$B = 1 - \frac{t}{\cos\kappa}\frac{N_B}{2\pi r} \tag{3.29}$$

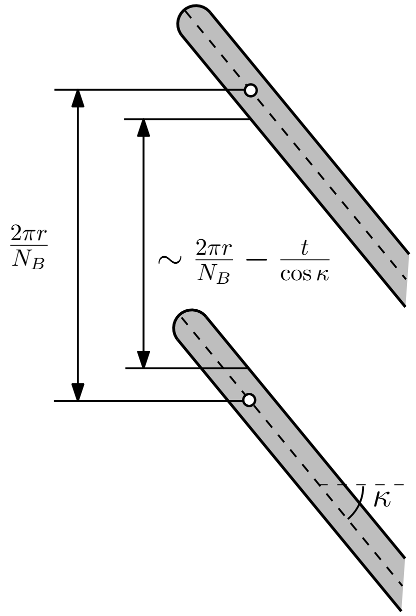

Figure 3-12: Definiton of passage free area ratio $B$, adapted from [13]

The model consists of a source term for the continuity equation which adds mass to the flow to create the effect of the area change caused by the blade metal blockage. The only input is $B$ which is known from the geometry of the inducer.

$$\hat{S}_m = -\rho\frac{1}{B}\left(\hat{w}_x\frac{\partial B}{\partial x} + \hat{w}_r\frac{\partial B}{\partial x}\right) \tag{3.30}$$

Additional sources terms are required for the momentum equations to bookkeep the added mass, which are the product of mass source term $S_m$ and the local velocity components. Depending on the CFD solver used to implement the blade passage model, these source terms may be added automatically to the flow when a mass source term is specified. This is the case for the solver used in this research, ANSYS CFX.

$$\hat{S}_x = -\rho \frac{1}{B}\left(\hat{w}_x \frac{\partial B}{\partial x} + \hat{w}_r \frac{\partial B}{\partial x}\right) \cdot \hat{w}_x \tag{3.31}$$

$$\hat{S}_r = -\rho \frac{1}{B}\left(\hat{w}_x \frac{\partial B}{\partial x} + \hat{w}_r \frac{\partial B}{\partial x}\right) \cdot \hat{w}_r \tag{3.32}$$

$$\hat{S}_\theta = -\rho \frac{1}{B}\left(\hat{w}_x \frac{\partial B}{\partial x} + \hat{w}_r \frac{\partial B}{\partial x}\right) \cdot \hat{w}_\theta \tag{3.33}$$

### Validation of the Blade Metal Blockage Model

The blade metal blockage model was validated using a simple test case, inviscid and incompressible flow through a stationary straight vane row. This geometry is depicted in Figure 3-13.

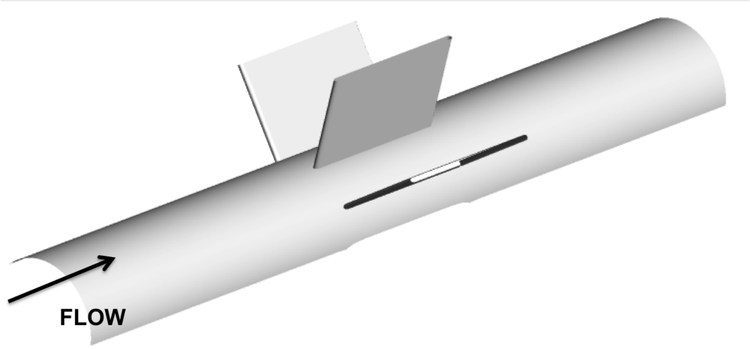

Figure 3-13: Blade metal blockage model test case

Since the flow is inviscid and the vanes are straight, there is no flow turning or viscous losses, so it is assumed the normal and parallel forces on the flow are zero. Without a pressure rise through the vane row there is no mechanism to drive the strong radial flows which would require a binormal force, so it is also neglected. Applying only the blade metal blockage model sources terms from the blade passage model, the pitchwise averaged flow through the vanes was recreated in an axisymmetric body force calculation. The static pressure distribution was captured to within 1% over the bulk of the blade passage, with a maximum error of 10% error near the leading and trailing edges, where some pressure overshoot occurs due to local flow acceleration around the blades edges (which would be captured by the parallel force in the full blade passage model).

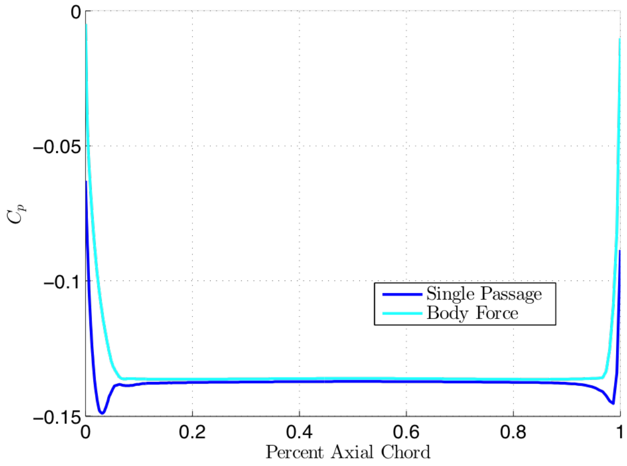

(a) Streamwise distribution of static pressure at midspan

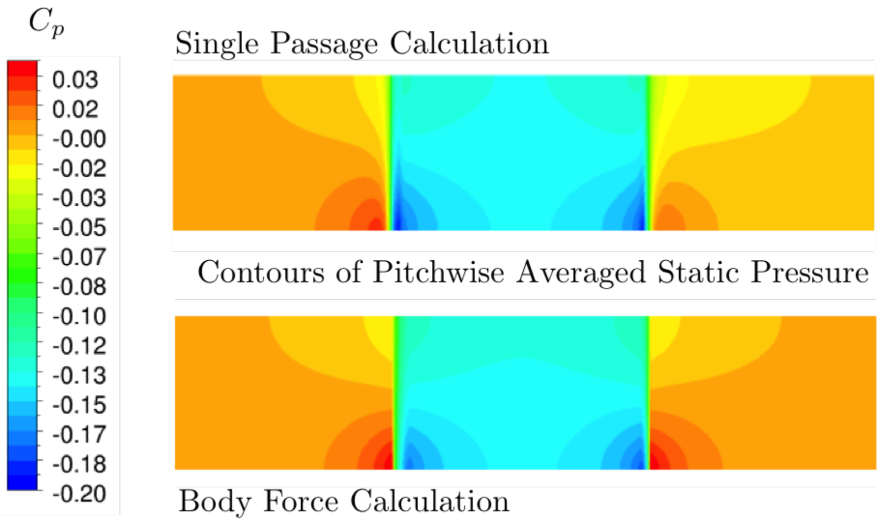

(b) Contours of static pressure

Figure 3-14: Blade metal blockage model capture of straight vane static pressure distributions

## 3.5 Analytical Representation of Force Component Empirical Terms

The final element to the blade passage model is formulating analytical representations of the empirical terms in each force component model in order to allow the force field to respond to changes in the flow field.

### 3.5.1 Relative Flow Angle Deviation Gradient

The relative flow angle deviation gradient $\frac{\partial \delta_\beta}{\partial \bar{l}}$ is represented analytically by calculating a one dimensional fit of the value of $\frac{\partial \delta_\beta}{\partial \bar{l}}$ to the local relative velocity at each $x$,$r$ location in the body force extraction grid.

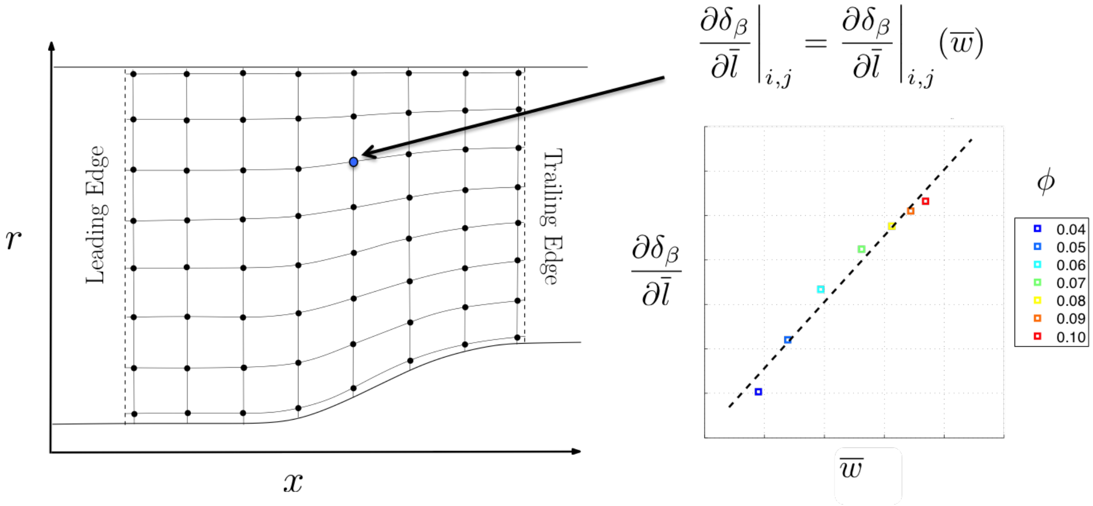

Figure 3-15: Analytical representation of relative flow angle deviation gradient

Across the bulk of the blade domain, a simple linear fit captures the relative flow angle deviation gradient data well and allows for extrapolation beyond the range of data consistently with the trends observed. Figure 3-16 shows two of the individual data fits, near the leading edge and well into the passage in the region were the magnitude of the relative flow angle deviation gradient is highest.

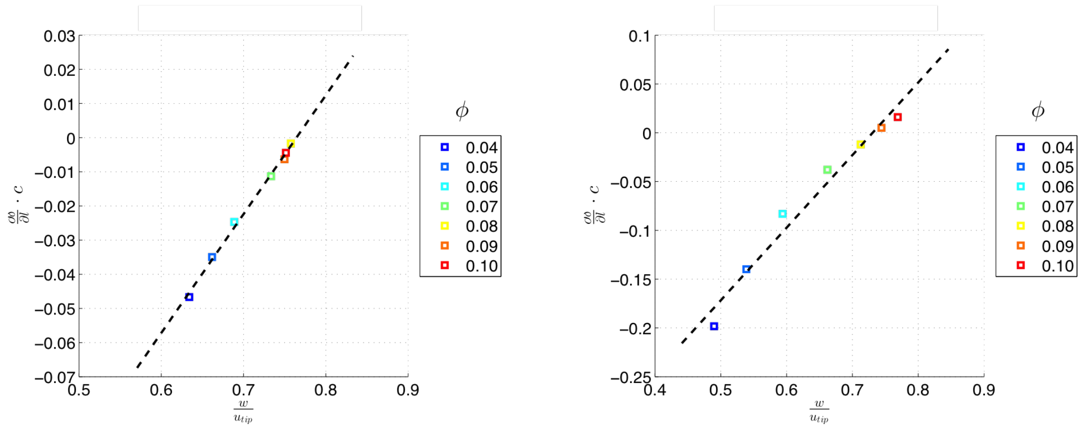

(a) Near leading edge (2% chord) at midspan

(b) 20% chord at midpsan

Figure 3-16: Linear fits of relative flow angle deviation gradient

### 3.5.2 Meridional Entropy Gradient

The analytical representation of the meridional entropy gradient is formulated in the same manner as the relative flow angle deviation angle gradient, a one-dimensional fit to the local relative velocity. Linear fits again capture the trends of the data well across the blade domain, as shown in Figure 3-17.

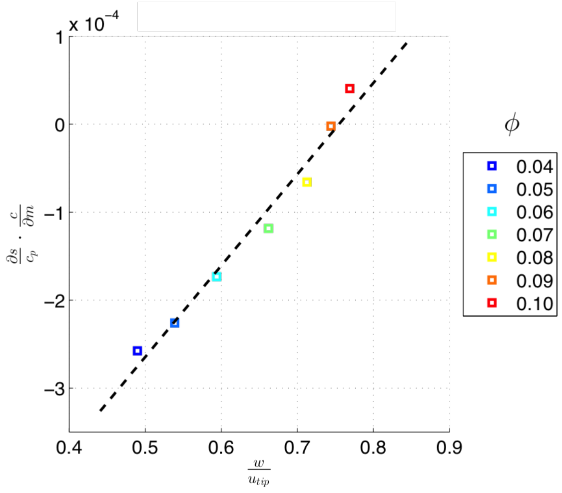

Figure 3-17: Linear fit of meridional entropy gradient

### 3.5.3 Pitch Angle Deviation Gradient

The analytical representation of the pitch angle deviation gradient takes the same form as the normal force and parallel force empirical term representations. As for the other cases, a linear fit is satisfactory to capture the observed trends in the data for the bulk of the blade domain, as observed in the fits at 20% and 80% chord at midspan seen in Figure 3-18.

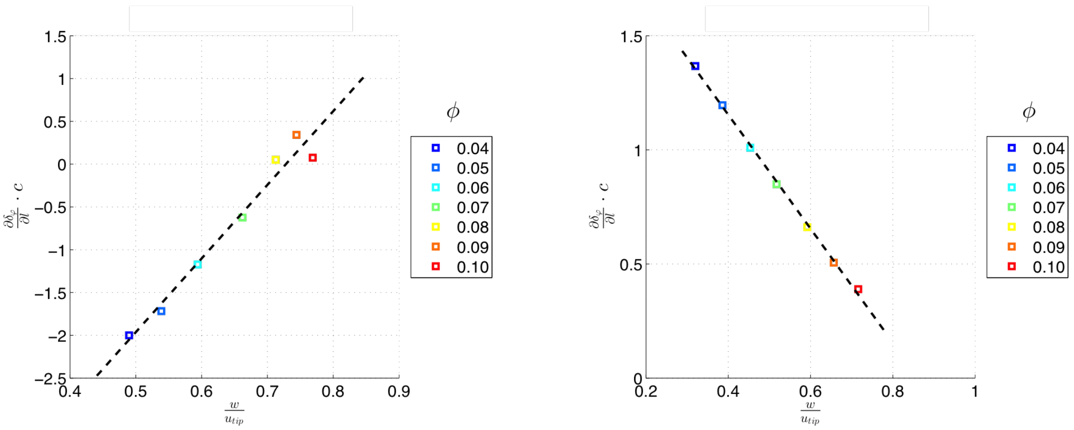

(a) 20% chord at midspan (b) 80% chord at midpsan

Figure 3-18: Linear fits of pitch angle deviation gradient

### 3.5.4 Challenges Encountered in Fitting Process

While the linear fits used in each empirical term analytical formulation capture the trends observed in the term values well over the bulk of the blade domain, near the hub and shroud the fits breakdown and no longer capture the data. This is due to the formation and shift of backflow regions as operating conditions change, which causes discontinuities in the flow angles used to calculate the empirical terms. In the backflow regions, the discontinuities result in scattered data which is challenging for any polynomial based fitting scheme to capture, as observed near the shroud in Figure 3-19.

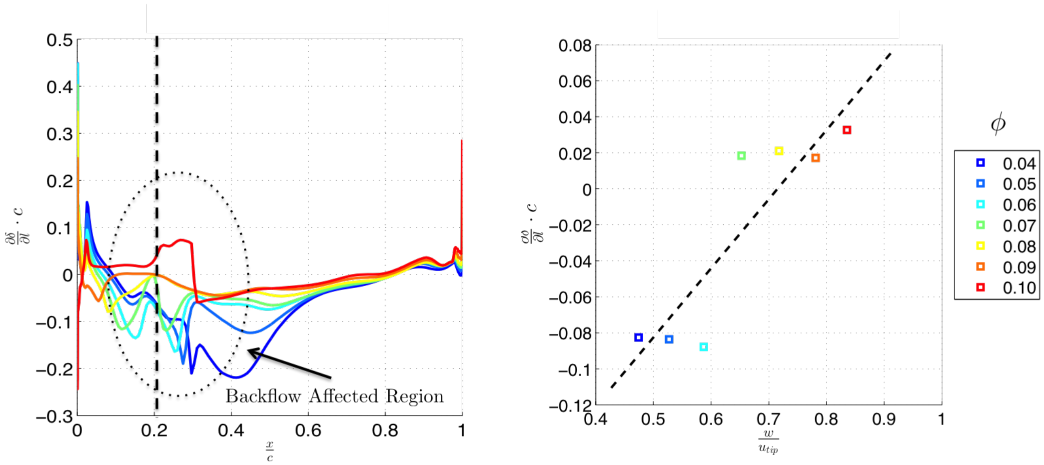

(a) Relative flow angle deviation gradient distrbution at 95% span

(b) Linear fit of $\frac{\partial \delta_\beta}{\partial \bar{l}}$ at 95% span and 20% chord

Figure 3-19: Impact of backflow on $\frac{\partial \delta_\beta}{\partial \bar{l}}$ fits near shroud

## 3.6 Body Force Model Implementation

### 3.6.1 Force Extraction Process Implementation

The force extraction process is implemented in MATLAB and the CFX post processor software, CFD-Post. The calculation of the pitchwise averaged flow field data is done in CFD-Post. A specific geometry feature CFD-Post calls a“polyline” is created at the desired radial and axial location in the blade blade passage, as demonstrated in Figure 3-20. The area average of the desired quantity is computed by CFD-Post along the polyline. This value is then exported and stored externally. CFD-Post incorporates a scripting language that allows this process to be done in an automated fashion, so MATLAB scripts were built to interface with CFD-Post and extract the necessary pitchwise averaged data.

The pitchwise averaged data was then used within other MATLAB scripts to compute the forces, empirical terms, analytical fits, and other necessary quantities needed for the blade passage model, and write input files for the commercial CFD solver used to implement the blade passage model.

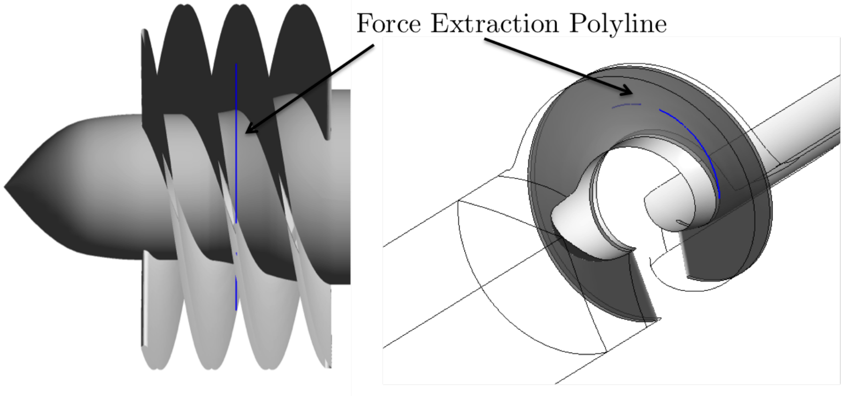

Figure 3-20: Example of "polyline" used for force extraction in CFD-Post

### 3.6.2 Blade Passage Model Implementation

The blade passage model was implemented in ANSYS CFX, the same CFD software used for computing the single passage RANS calculations.

### 3.6.3 Computational Grids

The axisymmetric computational grids used for body force calculations were generated from the three dimensional inducer geometry using ANSYS ICEM mesh generation software. The hub and shroud boundaries are refined to capture the developing boundary layers on the surfaces. The meshes used for both the P-LPOP inducer and the PWA inducer were 20° wedges with periodic boundary conditions applied, each containing approximately 500,000 cells. The P-LPOP body force computational mesh is shown in Figure 3-21.

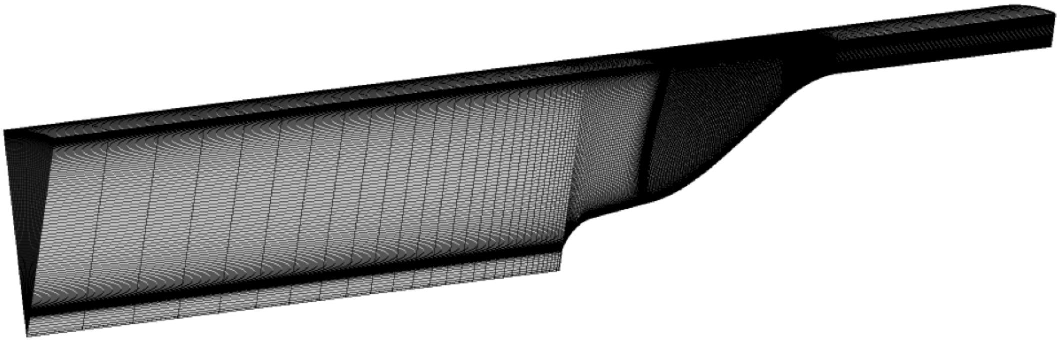

Figure 3-21: P-LPOP inducer body force computational mesh

Small discrepancies between the hub profiles in the single passage RANS meshes and the body force computational meshes, seen in Figure 3-22, were noted during the body force model assessment process, detailed later in Section 4.3. These discrepancies were determined to be caused by the ICEM's automatic conversion of the single passage RANS geometry into spline representations when imported to use for mesh generation. While the errors are small, less than 1% of the blade span, it is suggested that future body force grids be generated in a manner which avoids these discrepancies.

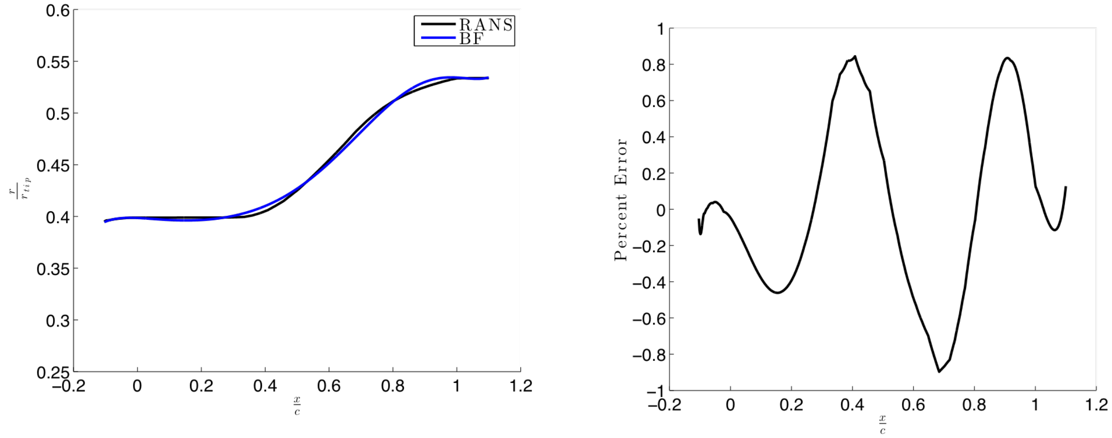

(a) Comparison of single passage RANS and body force grid hub profiles

(b) Error in body force grid hub profile

Figure 3-22: Discrepancies in body force grid hub profile for PWA inducer

### 3.6.4 Commercial CFD Solver Setup

The force component models were implemented as CFL "expressions" in the CFX preprocessing software, CFX-Pre. Since CFX is an unstructured solver, there is no access to the individual cell information, so the required model inputs were implemented as "user-defined interpolation functions", where the list of input values as calculated on the body force extraction grid, with associated $x$,$r$ coordinates, were fed into the solver, which then interpolated those values internally on to the actual $x$,$r$ location of the computational cells. The solver requires momentum sources be implemented in either cylindrical or cartesian coordinates, so a "user fortran function" was written to carry out the necessary coordinate transformation from the natural coordinate system of the model to the cylindrical system of the solver. For all body force model calculations, a total pressure boundary condition was applied at the inlet, and a mass flow boundary condition was applied at the outlet. The $k$-$\omega$ - SST turbulence model was used for consistency with the single passage RANS calculations.

# 3.7 Extension of Blade Passage Model to Two Phase Flows

## 3.7.1 Modification of Blade Passage Model

In order to simulate two-phase flows with the blade passage model, several modifications were implemented. The first is to replace the density, assumed constant in all models, with the local effective density $\rho_{eff}$.

$$\rho_{eff} = \rho_\ell \cdot (1 - \alpha_v) + \rho_v \cdot \alpha_v \tag{3.34}$$

The force extraction process is also altered to extract forces from two-phase single passage RANS calculations. As seen in Section 2.5, the presence of cavitation in the flow can significantly alter the blade loading distributions of the inducers by changing the leading edge stagnation point location. Since the flow incidence angle decreases, the blades have to turn the flow less to meet the blade metal angle, indicating the normal force should decrease in magnitude near the leading edge. This is exactly what is observed in Figure 3-23, which shows the normal force distribution at midspan for the PWA inducer at different cavitation numbers. Outside of the region affected by cavitation, the normal force distributions show little variation, suggesting that the flow field downstream of the main blade cavitation region is not sensitive to the details of the cavitating flow upstream.

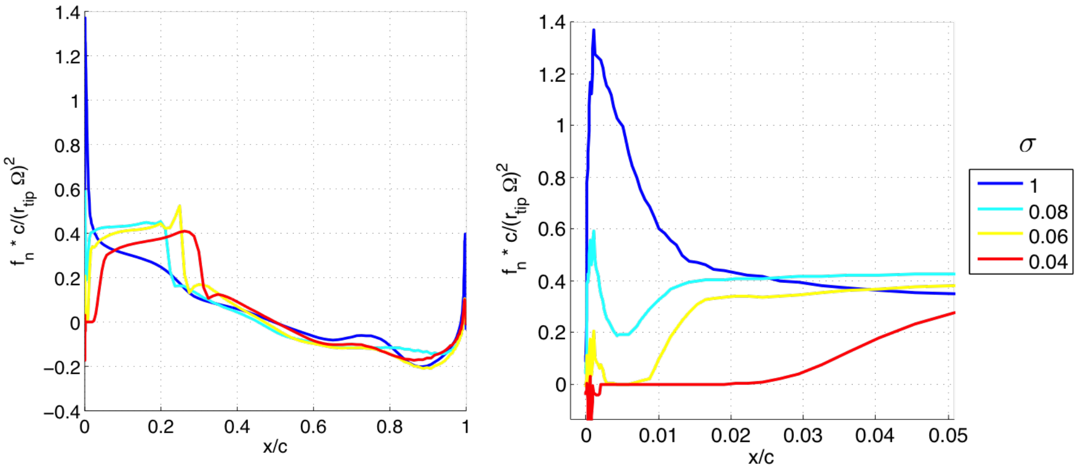

(a) Normal force distributions at midspan

(b) Closeup of leading edge region

Figure 3-23: Effect of cavitation on extracted normal force distributions for PWA inducer

Finally, the analytical representation of the force component model empirical terms must be altered for two-phase flows. The approach used for the single-phase blade passage model provides a natural extension to two-phase flows: instead of a one-dimensional fit on the local relative velocity, a two-dimensional fit on the local relative velocity and local cavitation number can be used.

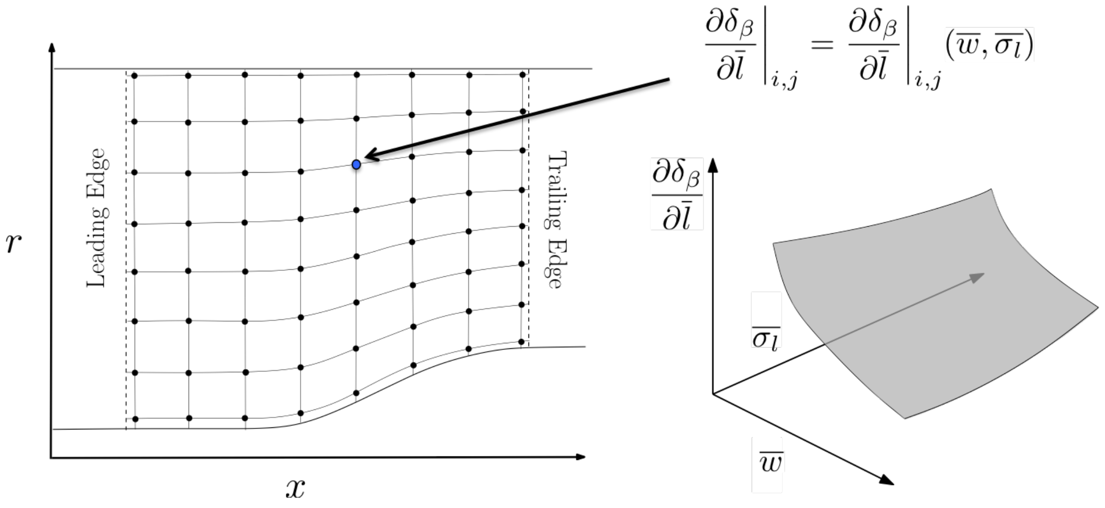

Figure 3-24: Analytical representation of relative flow angle deviation gradient for two-phase flows

### 3.7.2 Cavity Blockage Model

A preliminary model to capture the effect of cavity blockage on the flow was also formulated. The model is derived from the Rayleigh-Plesset cavitation model as implement in CFX [28] using the blade force average in the same manner as the force component models. Based on the equation of the same name which governs the growth and decay of individual vapor bubbles in a liquid, the Rayleigh-Plesset cavitation model defines the interphase mass transfer rate as a function of the local static pressure, the fluid's vapor pressure $p_v$, and vapor volume fraction $\alpha_v$. The model has four empirical parameters: $R_{nuc}$, which represents the radius of a typical nucleation site for cavitation (a dissolved gas bubble or solid particulate), $\alpha_{nuc}$, the volume fraction of nucleation sites, and $F_{vap}$ and $F_{cond}$, which account for the rate difference observed experimentally between the vaporization and condensation.

$$\dot{m}_{\ell\leftrightarrow v} = \begin{cases} F_{cond} \frac{3\alpha_v \rho_v}{R_{nuc}} \sqrt{\frac{2}{3}\frac{|p_v - p|}{\rho_\ell}} & \text{if } p \geq p_v \\ F_{vap} \frac{3\alpha_{nuc}(1-\alpha_v)\rho_v}{R_{nuc}} \sqrt{\frac{2}{3}\frac{|p_v - p|}{\rho_\ell}} & \text{if } p < p_v \end{cases} \tag{3.35}$$

Applying the blade force average creates an extra interphase mass source term $S_{cav}$ which is analogous to the force term in the blade force average derivations of the force component models.

$$S_{cav} = \begin{cases} \overline{\dot{m}_{\ell\leftrightarrow v}} - F_{cond} \frac{3\overline{\alpha_v} \rho_v}{R_{nuc}} \sqrt{\frac{2}{3}\frac{|p_v - \overline{p}|}{\rho_\ell}} & \text{if } \overline{p} \geq p_v \\ \overline{\dot{m}_{\ell\leftrightarrow v}} - F_{vap} \frac{3\alpha_{nuc}(1-\overline{\alpha_v})\rho_v}{R_{nuc}} \sqrt{\frac{2}{3}\frac{|p_v - \overline{p}|}{\rho_\ell}} & \text{if } \overline{p} < p_v \end{cases} \tag{3.36}$$

The new source term is used as the empirical term in the model and can be calculated directly from Equation 3.36. The analytical representation can be formulated in the same manner as for the force empirical terms, with a two dimensional fit to the local relative velocity and local cavitation number. Applying the body force calculation flow field quantities, the final expression for the cavity blockage model is given below.

$$\widehat{\dot{m}_{\ell\leftrightarrow v}} = \begin{cases} F_{cond}\frac{3\hat{\alpha_v}\rho_v}{R_{nuc}}\sqrt{\frac{2}{3}\frac{|p_v-\hat{p}|}{\rho_\ell}} + S_{cav} & \text{if } \hat{p} \geq p_v \\ F_{vap}\frac{3\alpha_{nuc}(1-\hat{\alpha_v})\rho_v}{R_{nuc}}\sqrt{\frac{2}{3}\frac{|p_v-\hat{p}|}{\rho_\ell}} + S_{cav} & \text{if } \hat{p} < p_v \end{cases} \tag{3.37}$$

# Chapter 4

# Assessment of Body Force Model Performance

## 4.1 Overview of Assessment Process

The performance of the body force model for single phase flows was assessed on a component by component basis. Figure 4-1 presents an outline of this process. The force extraction process was successfully validated, but challenges were encountered during assessment of the performance of the blade passage model with both specified empirical terms and analytically represented empirical terms. These challenges are described in Section 4.3.

## 4.2 Validation of Force Extraction from Single Passage RANS Calculations

To validate the force extraction process, body force calculations were carried out in which the forces extracted from single passage RANS calculations were directly applied to the flow as momentum source terms instead of being calculated by the force component models. The angles at which the forces were applied were specified from input data from the pitchwise averaged single passage RANS flow field rather

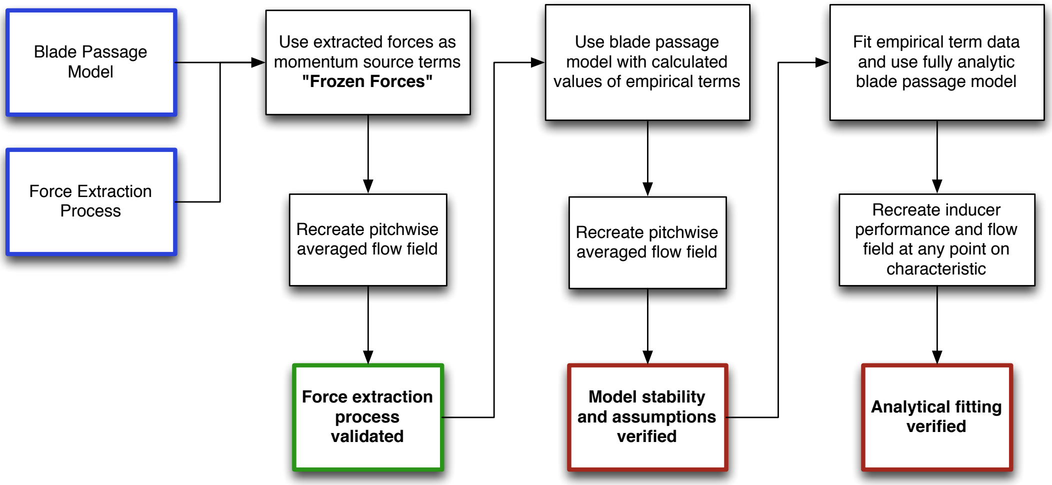

Figure 4-1: Outline of single-phase blade passage model assessment

then the local flow field. As the forces are effectively “frozen” and unable to respond to the flow field, the calculations are referred to as frozen force calculations.

As noted in Section 2.6, the most critical requirement for the body force model is that it capture the inducer local flow field accurately, so the metrics used to asses the force extraction process are the local velocity field and static pressure distribution, in addition to the global head rise performance.

### 4.2.1 Performance of Frozen Force Calculations at Design Point

At the design point, the frozen force calculation successfully captures the single passage RANS calculation flow field. The backflow region created by the tip clearance flow is qualitatively captured by the body force calculation, and the error in the axial extent of the backflow is 18%. A comparison between the single passage and body force backflow regions is shown in Figure 4-2. Streamwise distributions of axial velocity near the hub, at midspan, and near the shroud are presented in Figure 4-3, and the body force calculation captures the single passage RANS distributions with a maximum error of 8%. Near the shroud, the body force calculation over predicts the amount of backflow present, both near the leading edge of the main inducer blade and within the tandem blade passage.

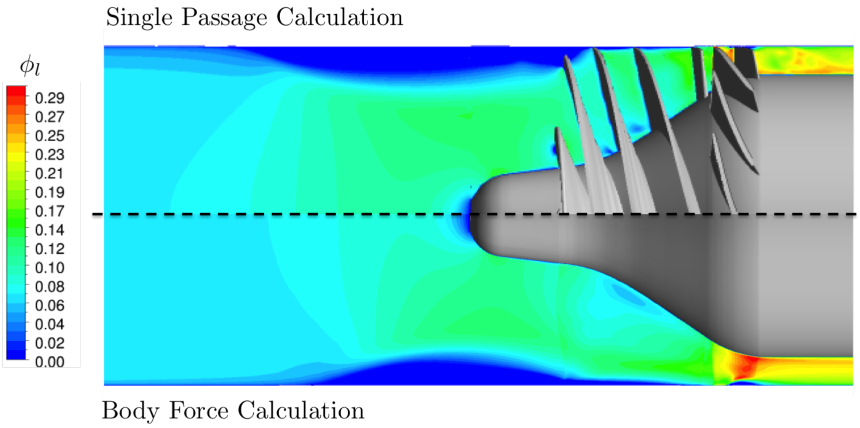

Figure 4-2: Contours of nondimensional axial velocity, $\phi = 0.07$

The static pressure distribution from the frozen force calculation shows good agreement with the single passage RANS distribution. A qualitative comparison is given in Figure 4-4, and streamwise distributions near the hub, at midspan, and near the shroud are shown in Figure 4-5. The maximum error observed in the streamwise distributions is 7.8%, and occurs in the tandem blade in the distribution at 99% span, where the body force calculation is over predicting the presence of a backflow region, as seen in the axial velocity distribution.

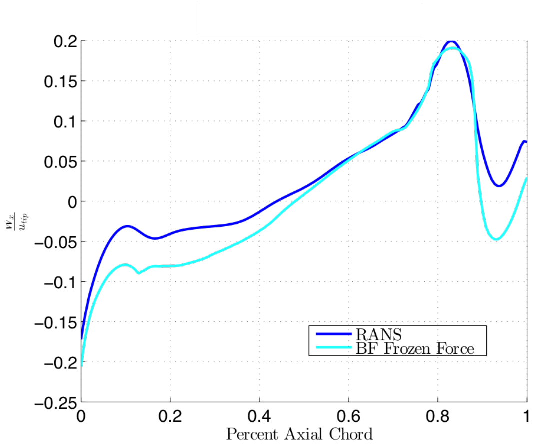

(a) Near shroud (99% Span)

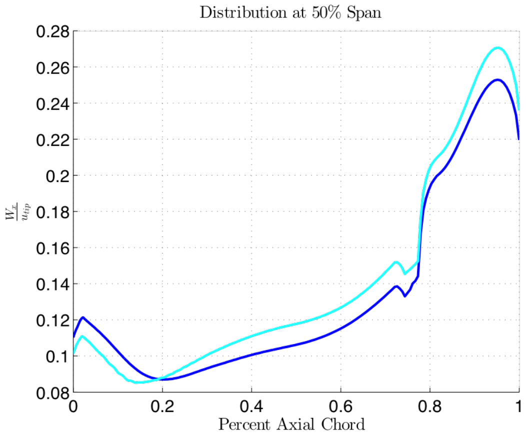

(b) Midspan

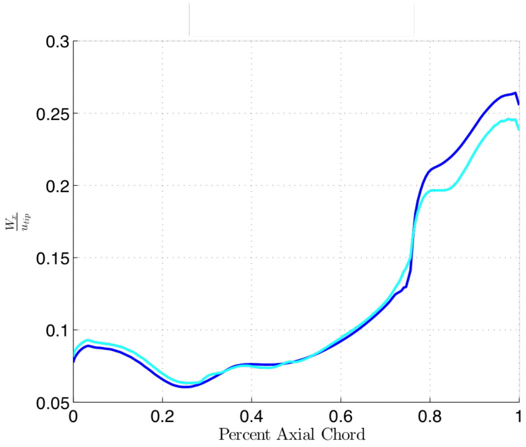

(c) Near hub (1% Span)

Figure 4-3: Streamwise axial velocity distributions in P-LPOP inducer

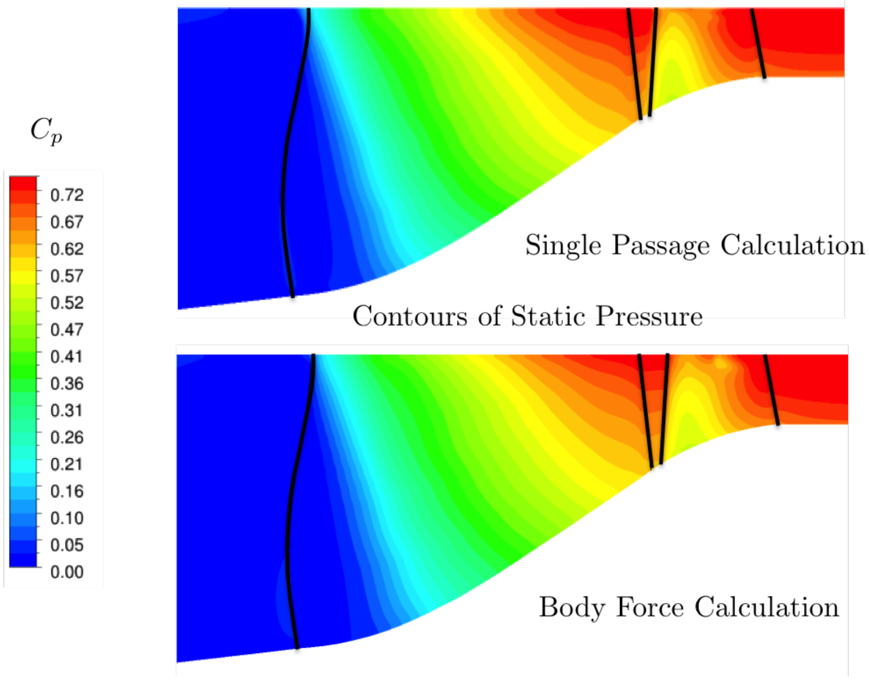

Figure 4-4: Comparison of pitchwise averaged single passage calculation and frozen force calculation static pressure fields at P-LPOP design point ($\phi = 0.07$)

### 4.2.2 Performance of Frozen Force Calculations at Off Design Conditions

Frozen force calculations also capture the single passage RANS flow fields at operating conditions off the design point of the inducer. At $\phi = 0.05$, the frozen force calculation captures the axial extent of the backflow region with an error of 17%, and at $\phi = 0.10$ the lack of an upstream backflow region is correctly captured. The flow fields of both cases are shown in Figures 4-6 and 4-7. The same trends are observed in the streamwise distributions of axial velocity and static pressure between the two cases. The frozen force calculations show good agreement with the single passage calculations outside of backflow regions, but have difficulty capturing the axial velocity distribution within the backflow regions, both at the hub and shroud for the low flow coefficient case, and at the shroud for the high flow coefficient case. The span wise extent of the backflow region within the passage is also overpredicted by 90% by the frozen force calculation, as observed in Figure 4-9e.

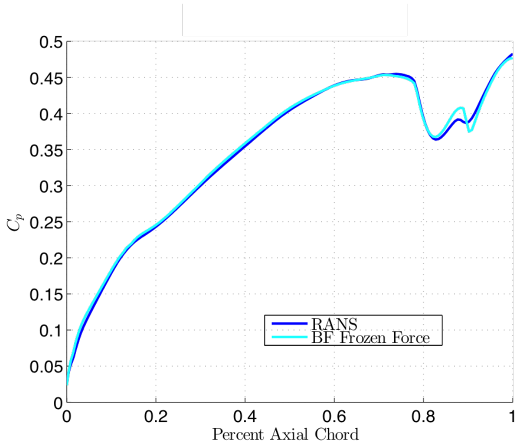

(a) Streamwise distributions near shroud (99% Span)

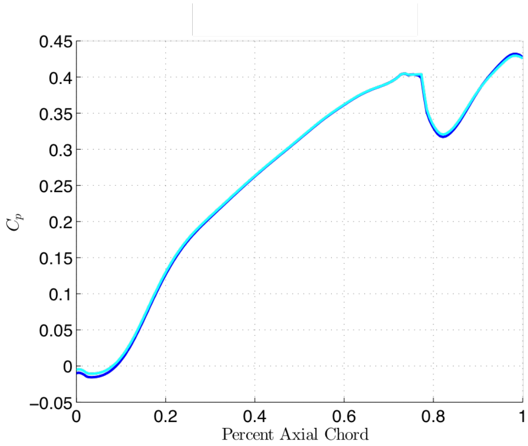

(b) Streamwise distributions at midspan

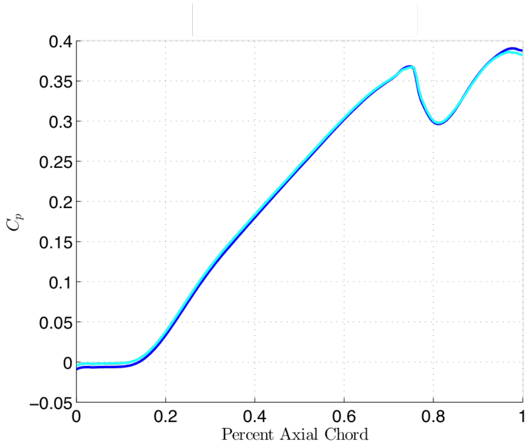

(c) Streamwise distributions near hub (1% Span)

Figure 4-5: Streamwise static pressure distributions in P-LPOP inducer

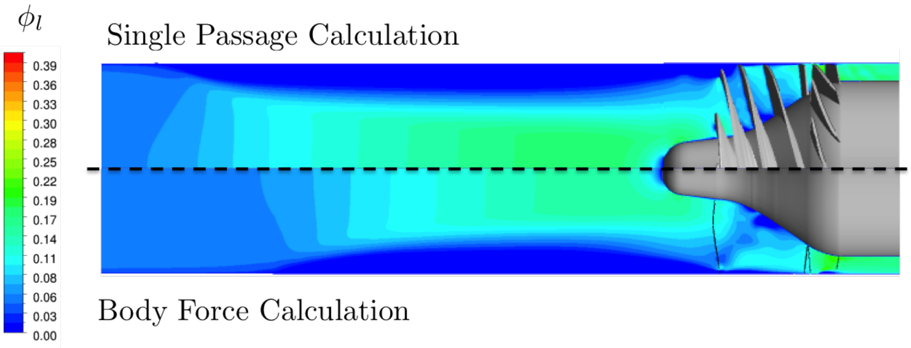

Figure 4-6: Contours of nondimensional axial velocity, $\phi = 0.05$

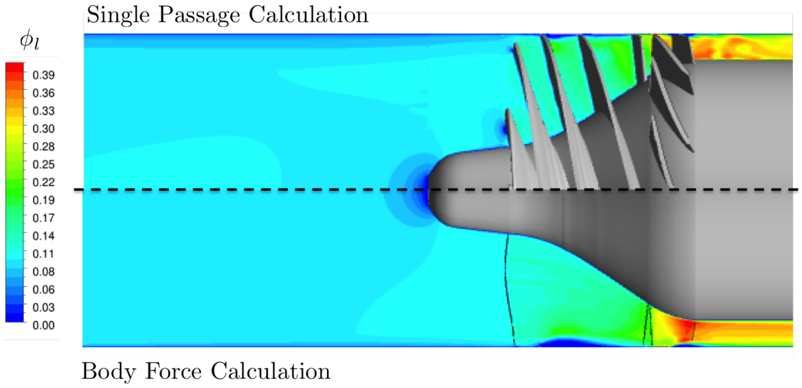

Figure 4-7: Contours of nondimensional axial velocity, $\phi = 0.10$

### 4.2.3 Global Head Rise Performance

The frozen force calculations reproduce the global head rise coefficient of the P-LPOP inducer with a maximum error of 3.9% between the frozen force calculation and the single passage RANS calculation at the lowest tested flow coefficient, as shown in Figure 4-10a. Similar accuracy is achieved for the PWA inducer, which sees a maximum error of 3.2%, again occurring at the lowest flow coefficient computed, as depicted in Figure 4-10b. The increasing error in the frozen force calculation head rise with decreasing flow coefficient is attributed to the difficulty observed in correctly capturing the axial velocity distributions when significant backflow regions are present, which occurs at lower flow coefficients.

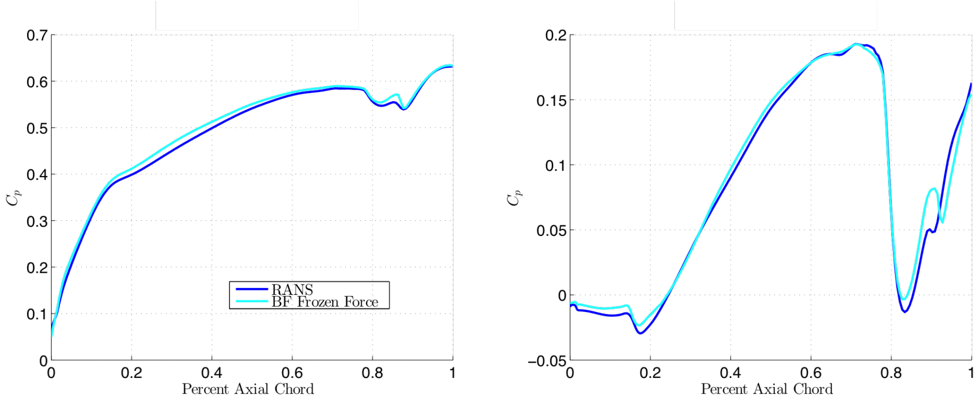

(a) 99% span - $\phi = 0.05$ (b) 99% span - $\phi = 0.10$

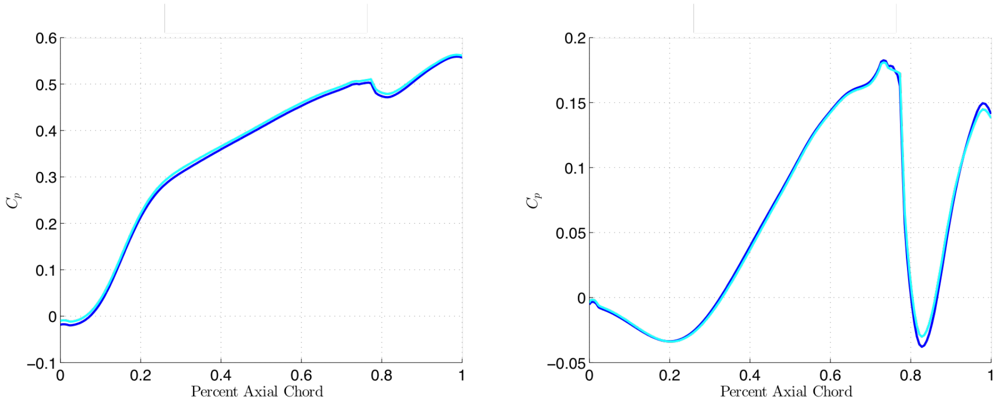

(c) Midspan - $\phi = 0.05$ (d) Midspan - $\phi = 0.10$

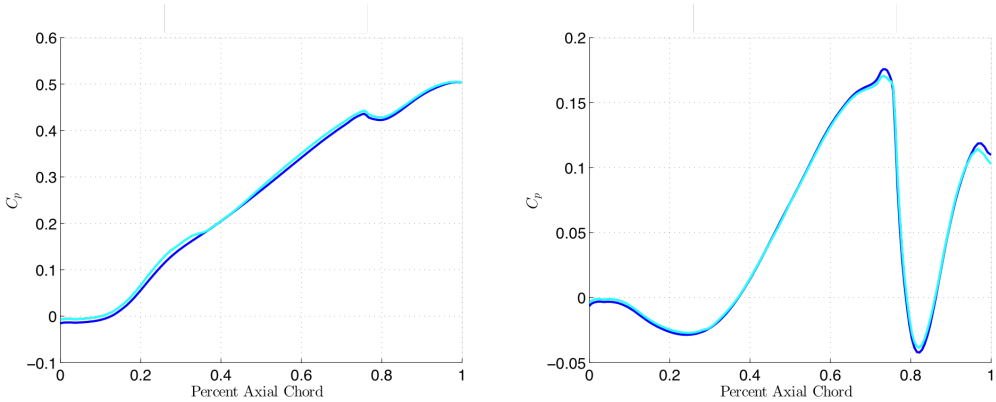

(e) 1% span - $\phi = 0.05$ (f) 1% span - $\phi = 0.10$

Figure 4-8: Streamwise static pressure distributions in P-LPOP inducer at off design conditions

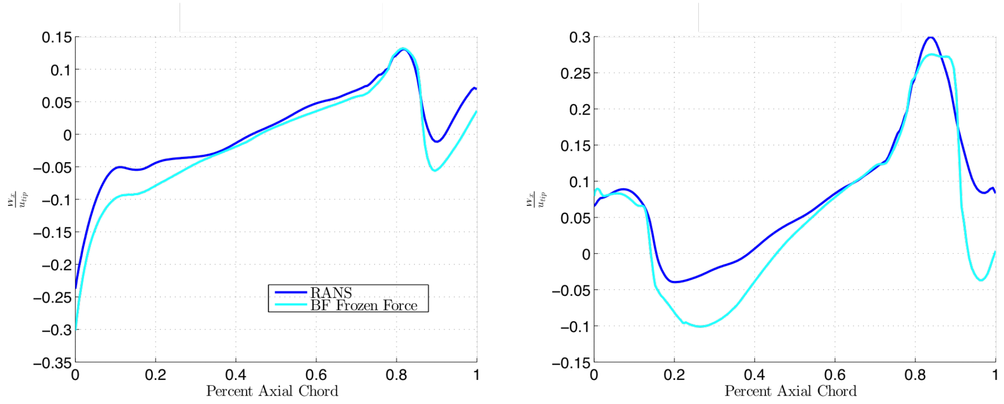

(a) 99% span - $\phi = 0.05$ (b) 99% span - $\phi = 0.10$

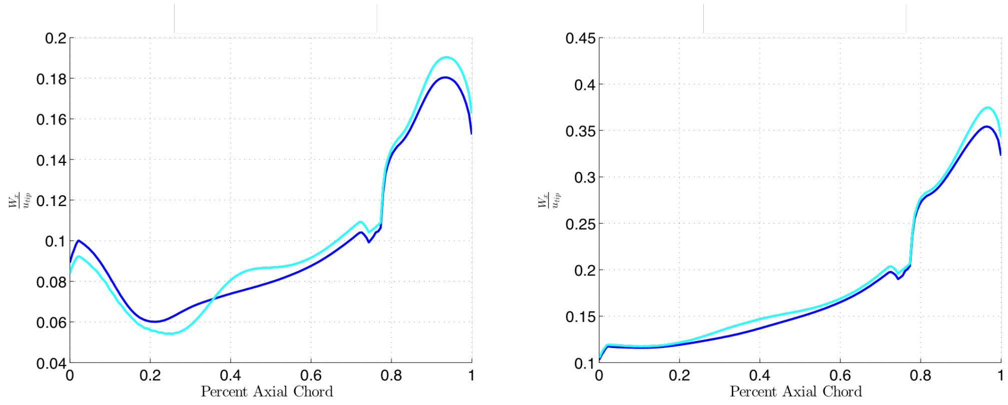

(c) Midspan - $\phi = 0.05$ (d) Midspan - $\phi = 0.10$

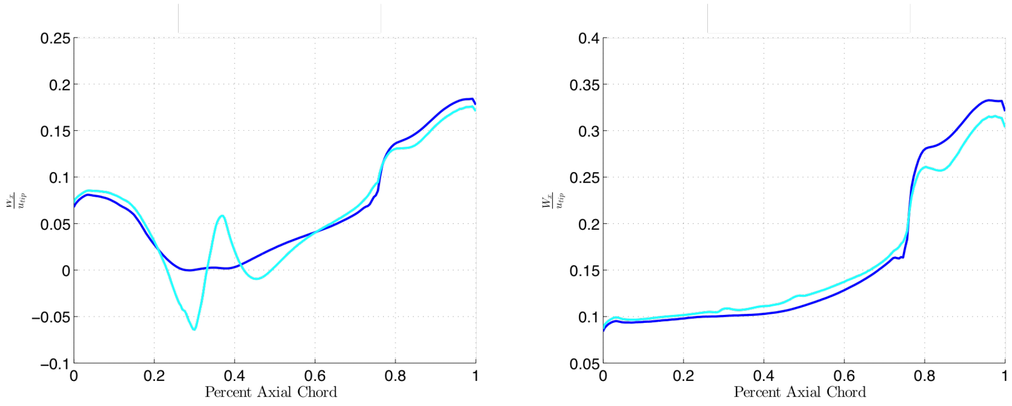

(e) 1% span - $\phi = 0.05$ (f) 1% span - $\phi = 0.10$

Figure 4-9: Streamwise axial velocity distributions in P-LPOP inducer at off design conditions

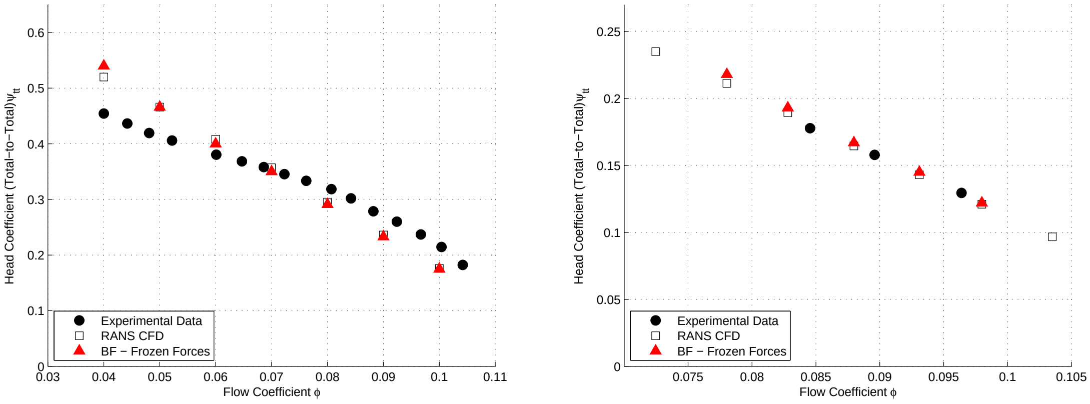

(a) P-LPOP inducer

(b) PWA inducer

Figure 4-10: Head rise performance of frozen force calculations

The frozen force calculations capture both the non-cavitating flow fields, including the passage radial flows and upstream backflow, and the global performance of the P-LPOP inducer across its operating range. This validates the force extraction process.

### 4.2.4 Necessity of Binormal Force Component

To assess the necessity of the binormal force component in the inducer blade passage model, a frozen force calculation with the binormal force removed was carried out. The forces were applied at specified angles, with the relative flow angle $\beta$ taken from the pitchwise averaged single passage calculation data, and the pitch angle $\varphi$ taken as the geometric gas path angle $\varphi_{GP}$ as was assumed in previous body force model formulations where a binormal force component was not included [13]. An operating condition of $\phi = 0.10$, significantly above the design point, was simulated in order to limit the extent of the radial flows within the passage. The calculation failed to capture the flow field of the single passage RANS calculation, with a large spurious recirculation region forming in front of the passage, as shown in Figure 4-11, proving the binormal force is required to capture the strong radial flows observed, and validating its addition to the blade passage model.

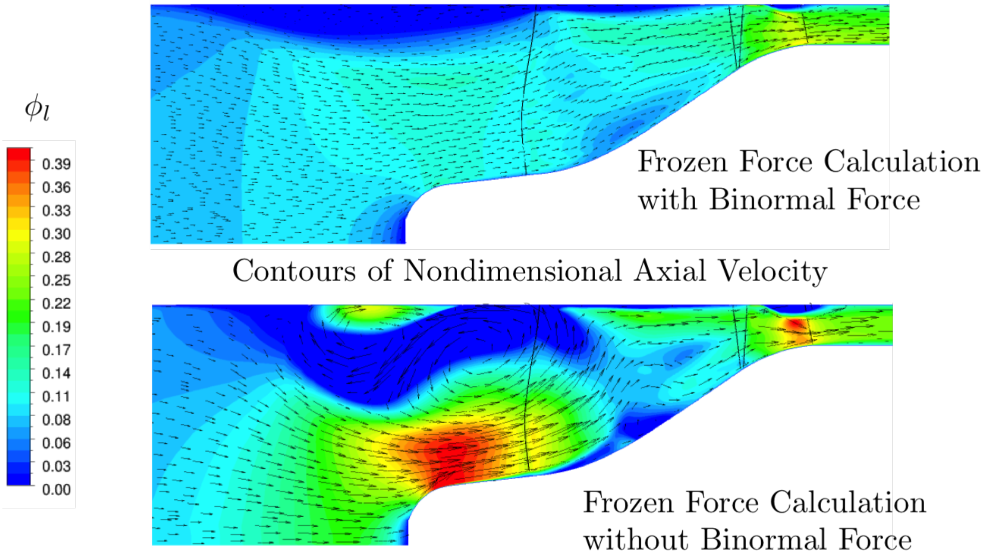

Figure 4-11: Impact of binormal force on frozen force calculation flow field for P-LPOP inducer at $\phi = 0.10$

## 4.3 Challenges Encountered in Model Assessment

Several challenges were encountered during the assessment of the blade passage model which resulted in body force calculation flow fields which failed to capture the original single passage RANS results. These flow fields contained a spurious recirculation region qualitatively similar to that seen in Figure 4-11. Diagnostics were carried out in an attempt to identify the causes of the recirculation. The results are presented here with suggestions for future work towards resolving the challenges.

### 4.3.1 Potential Pitch Angle Instability

In the blade passage model the forces, as calculated by the component models, are applied in the respective natural coordinate directions, as defined by the local flow angles $\hat{\beta}$ and $\hat{\varphi}$, creating an implicit dependence of the forces on the flow angles. In the frozen force calculations previously presented, the force application angles were not applied on the actual flow angles, but instead on the angles as calculated from the pitchwise averaged single passage RANS calculation.

During the development of previous body force models, an interim step in the assessment of the model was a frozen force calculation with the magnitude of the forces specified but the application angles set to the local flow angles, which validated the stability of the flow angle dependence. Previous models did not include the binormal force, so this dependency was only on the relative flow angle $\hat{\beta}$.

When frozen force calculations with the flow angle dependency enabled were carried out for the P-LPOP inducer, spurious recirculation regions were observed to form and dominate the flow field. In order to diagnose the cause of the recirculation regions, the same calculations were run with the simpler PWA inducer with no tip clearance to remove the impact of backflow near the shroud, and at high flow coefficient operating conditions to reduce the strength of the passage radial flows. Similar recirculation regions were observed to develop, as documented in Figure 4-12, which shows the state of the calculation flow field at intermediate iterations.

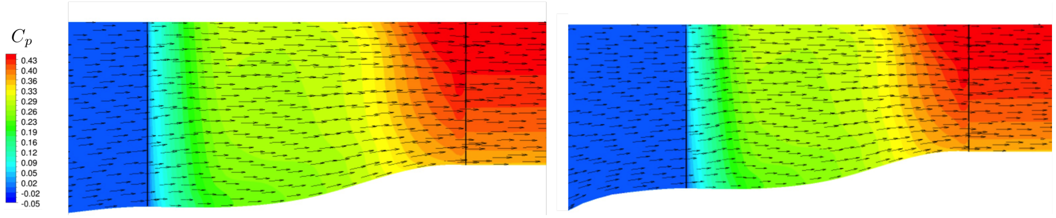

(a) 0 iterations (b) 20 iterations

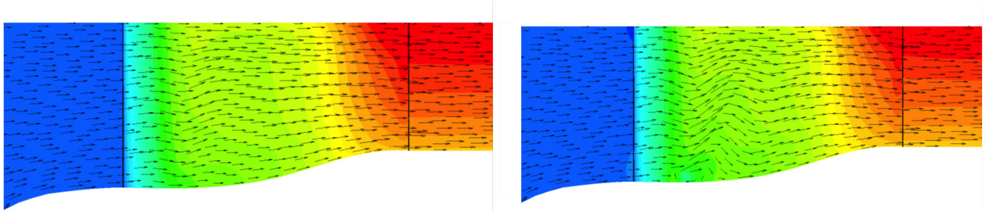

(c) 50 iterations (d) 100 iterations

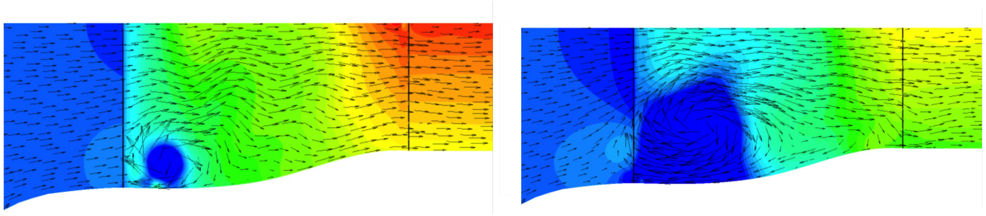

(e) 150 iterations (f) 200 iterations

Figure 4-12: Formation of spurious recirculation region in PWA inducer frozen force calculation with pitch angle dependence enabled ($\phi = 0.103$)

In order to isolate the impact of each flow angle, the same calculations were repeated but with only a single angle dependency enabled. Calculations testing the relative flow angle dependency confirmed its stability, as observed in previous model formulations, with only small discrepancies between the resulting flow fields and those observed in frozen force calculations without the angle dependency. The calculations with only the pitch angle dependency enabled showed the same recirculation regions.

As the magnitude of the forces applied is specified in the natural coordinate system, a change of pitch angle of the flow would result in a change in the magnitude of the individual force components in the solver's cylindrical coordinate system. Profiles of the pitch angle and radial force from the calculation shown in Figure 4-12 at 20 % chord, near where the first perturbations in the flow field appear, are presented in Figure 4-13. A strong correlation is noted between the change of the pitch angle and radial force magnitude as the calculation progresses, suggesting that a positive feedback loop may exist. The hypothesized mechanism is that an increase in pitch angle increases the radial component of the applied body force and decreases the axial component, which in turn further drives the pitch angle from its baseline value. This process would continue until the flow field breaks down, as observed in Figure 4-12e, where a spurious recirculation region has formed at the hub, as the axial force magnitude is no longer sufficient to balance the axial pressure gradient, and the flow reverses.

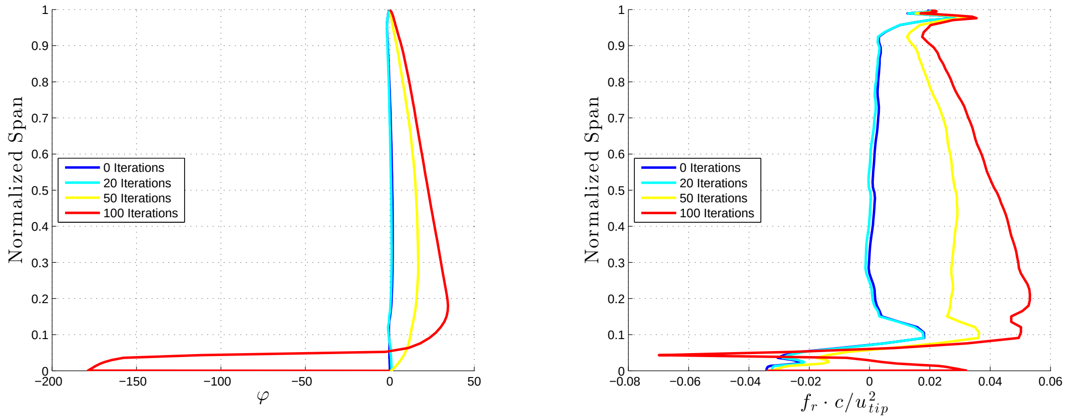

(a) Pitch angle $\hat{\varphi}$

(b) Radial force $f_r$

Figure 4-13: Profiles of pitch angle and radial force in PWA inducer at 20 % chord from frozen force calculation with pitch angle dependence enabled

More diagnostics are necessary to confirm this hypothesis. It is suggested that an analytical stability analysis be carried out on both flow angle dependencies in order to identify whether the observed recirculation regions occur due to a physical instability in pitch angle dependence. If this is the case, comparison with the seemingly stable relative flow angle dependence may reveal a method for resolution, similar to the recasting of the force model pressure gradient terms. If no physical instability is indicated, a more focused computational study could be undertaken to analyze exactly how the pitch angle begins to diverge.

### 4.3.2 Observed Discrepancy in Near-Hub Force Distributions

In order to continue assessment of the remaining components of the blade passage model, calculations with the blade passage model were run with the pitch angle dependence disabled and the force components applied according to specified pitch angle data from the appropriate single passage RANS calculation.

Two sets of calculations with the blade passage model were carried out. The first utilized the full blade passage model including analytical representations of each empirical term, and the second specified the values of the empirical terms directly from the extracted values. In both calculations, spurious recirculation regions were observed in the resultant flow fields. While qualitatively similar to the recirculation regions seen in the frozen force calculations carried out to asses the pitch angle dependence, it is believed that the root cause is dissimilar.

Investigation of the cause of the recirculation regions was again done using the PWA inducer with no tip clearance to eliminate the extraneous influences of the shroud backflow and associated radial flows. Figure 4-14 depicts the formation of the recirculation region in a body force calculation with the blade passage model and analytical representations. Unlike the pitch angle dependence calculations, no change in the bulk passage pitch angle is observed during the formation of the recirculation region. A similar process occurs in the calculations in which the empirical terms are directly specified, though more iterations are required before the recirculation region forms, suggesting that the same mechanism is causing the recirculation regions in both cases.

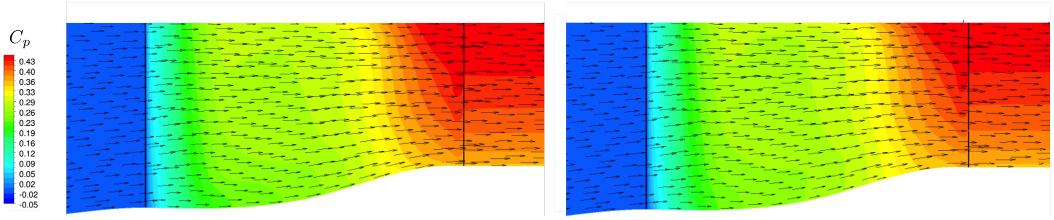

(a) 0 iterations (b) 20 iterations

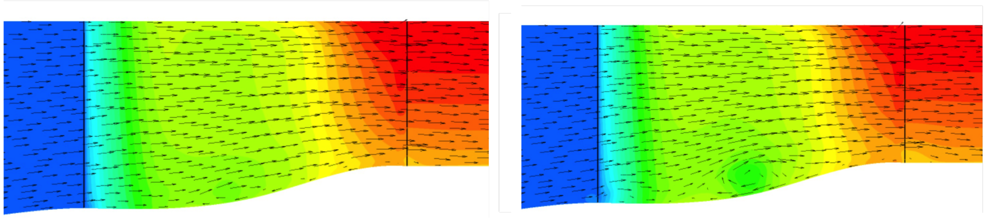

(c) 100 iterations (d) 200 iterations

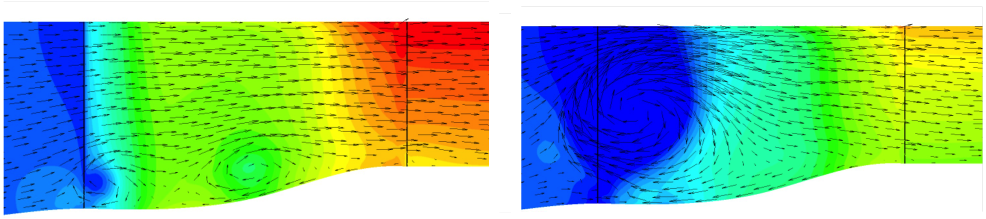

(e) 300 iterations (f) 500 iterations

Figure 4-14: Formation of spurious recirulation region in PWA inducer body force calculation with pitch angle frozen and force component models enabled ($\phi = 0.103$)

Analysis of the force distributions near the hub in the area where the recirculation region first forms reveal several factor that appear to contribute to the formation of the recalculation regions. Figure 4-15 displays a comparison of profiles of the normal force as extracted from the single passage RANS calculation and as calculated by the model from the flow field of a frozen force calculation which captures that single passage flow field at the 20% chord location. There are significant discrepancies between the two distributions near the hub, with the model force distribution displaying an inflection point not present in the extracted force distribution near 10% span, and a rapid change in the magnitude of the model force distribution in the boundary layer not seen in the extracted distribution. These discrepancies are hypothesized to be responsible for the recirculation region observed.

Plotting the extracted and analytically calculated relative flow deviation angle

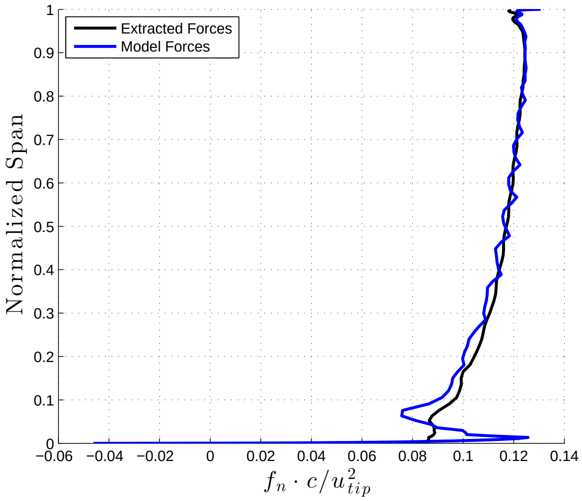

Figure 4-15: Discrepancy in normal force distribution at hub in blade passage model calculation for PWA inducer

gradients shows large errors in the analytical fits near the hub in the same region where the force discrepancies were observed; these errors are shown in Figure 4-16. The errors in $\frac{\partial \delta_\beta}{\partial \bar{l}}$ lead to larger force discrepancies than seen in Figure 4-15, accelerating the formation of the recirculation regions observed in calculations with the analytical representations of the empirical terms.

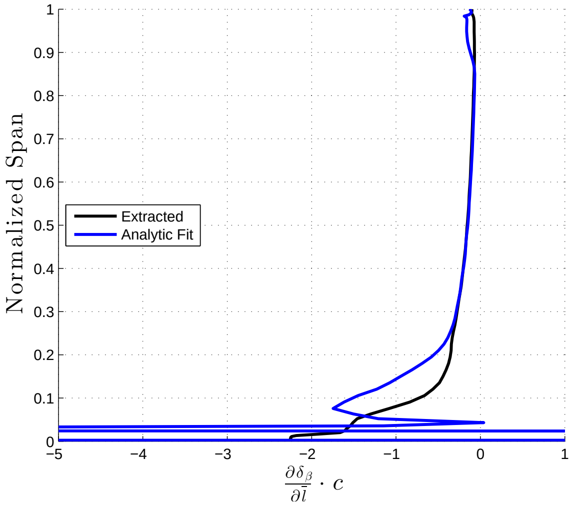

Figure 4-16: Error in analytical representation of relative flow angle deviation gradient at 20% chord for PWA inducer

It was discovered that the failure of the normal force model to recreate the extracted force distributions is partially attributable to a shortcoming in the pitchwise averaging scheme used in the force extraction process. As detailed in Section 3.6, the pitchwise averaged flow field data was obtained in an automated manner from CFD-Post using “polylines”. During development of the force extraction process, it was noted that placing a polyline within a certain distance of a boundary led to a failure of the polyline to accurately capture the circumferential data to be pitchwise averaged, as seen in Figure 4-17. This is caused by the fact that CFX is an unstructured solver, and as such no mesh information is available in the post processor. The polyline is independent of the mesh and interpolates data from nearby cells onto its coordinates; when the cells have low aspect ratios, as in the cells in inflated boundary layer mesh, the interpolation scheme fails. An acceptable tolerance was determined where the polyline would always capture valid circumferential data, and the final grid points of the body force extraction mesh were placed at this tolerance. This led to the extracted pitchwise averaged data to miss a portion of the boundary layer profile, as seen in Figure 4-18.

For the frozen force calculations, the failure to capture the full boundary layer profile had no impact, as CFX extrapolated the final force values to the endwall. However, when the force component models are used to calculate the forces, the large force discrepancies observed are created by the model’s response to the significantly different local flow field values in the boundary layer compared to the location where the empirical term value in the model was calculated.

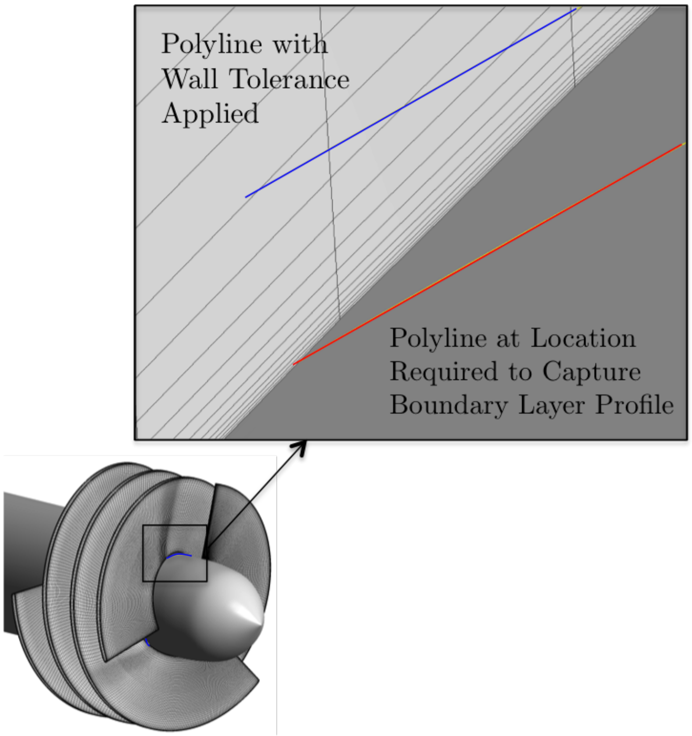

(a) Location of polylines

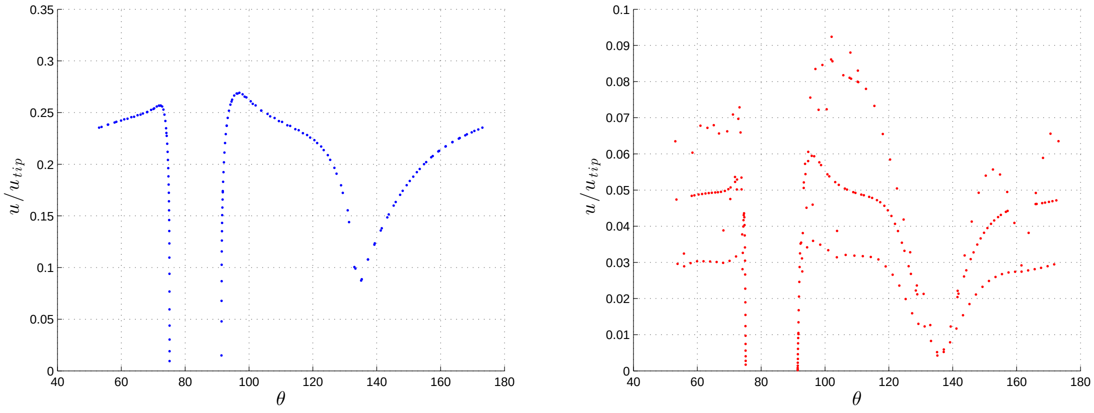

(b) Polyline with wall tolerance applied

(c) Polyline without wall tolerance applied

Figure 4-17: Necessity of polyline wall tolerance for capture of pitchwise averaged data

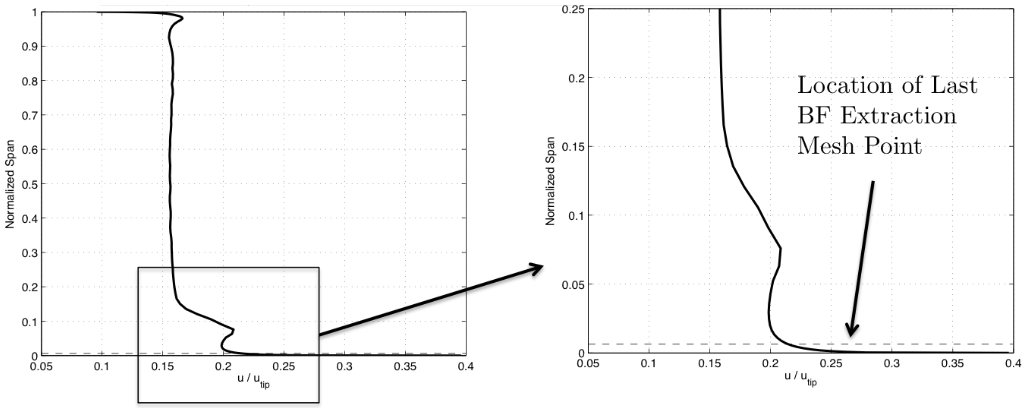

Figure 4-18: Profile of local stationary frame velocity at 20% chord demonstrating failure of force extraction process to capture full boundary layer profile

More diagnostics are required to determine the cause of the recirculation regions. In particular, the source of inflection point in the model force distribution outside of the boundary layer should be investigated. The pitchwise averaging method used in the force extraction process should also be modified to allow for capture of the full boundary layer profile.

## 4.4 Preliminary Assessment of Cavity Blockage Model

A preliminary assessment of the cavity blockage model was performed by carrying out a two-phase body force model calculation for the P-LPOP inducer with the cavity blockage model implemented. The operating conditions were set at the design flow coefficient of $\phi = 0.07$ and an intermediate cavitation number $\sigma = 0.04$ which corresponds to approximately 10% inducer head drop from the non-cavitating case. The forces extracted from the single passage RANS calculation were applied directly as momentum sources, with the application angles specified from input data. The pitchwise averaged interphase mass transfer rate was also applied directly in the calculation instead of being computed from the cavity blockage model.

Figure 4-19 displays the resulting vapor volume fraction in comparison with the pitchwise averaged single passage result. Both blade cavitation and backflow cavitation are captured in the body force calculation, but because no local flow field dependence is enabled, the vapor which forms inside the passage and is convected into the backflow region has no mechanism to condense back to the liquid phase.

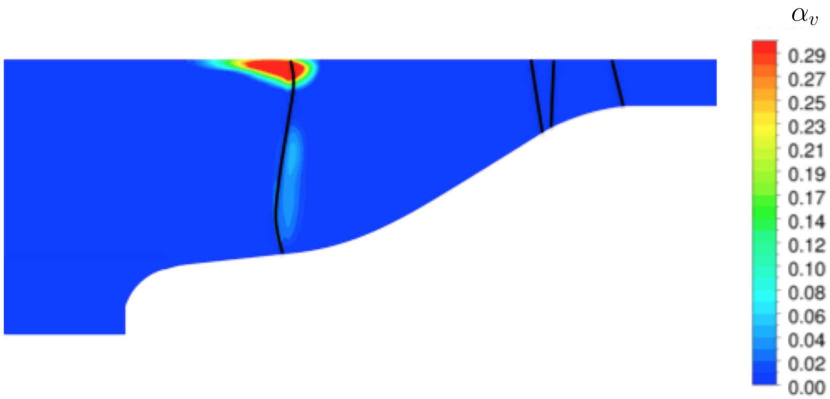

(a) Pitchwise averaged single passage RANS calculation

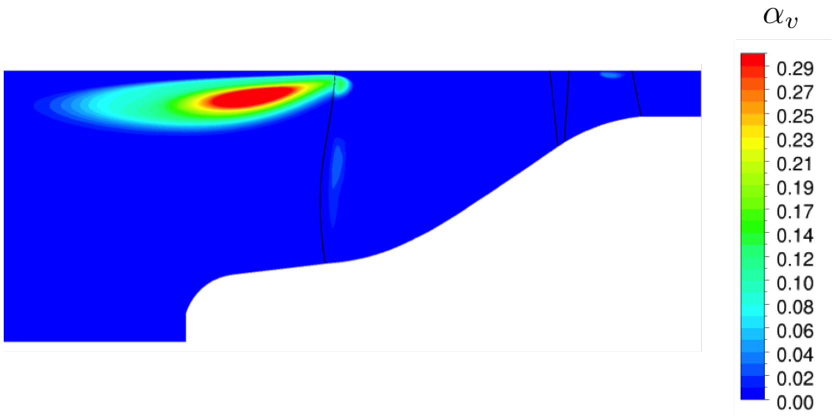

(b) Body force calculation

Figure 4-19: Comparison of pitchwise averaged single passage RANS distribution and body force distribution of vapor volume fraction

# Chapter 5

# Summary and Conclusions

## 5.1 Summary

The first body force model for a cavitating inducer was formulated with the end goal to enable the study of rotating cavitation and higher order cavitation instabilities. The model incorporates past blade passage model improvements as well as a new force component, the binormal force, introduced to allow the capture of the strong radial flows within the inducer blade passage and the upstream backflow regions. The force extraction process was successfully validated by demonstrating that body force calculations using the extracted forces directly as momentum source terms captured the performance and local flow fields of the P-LPOP inducer across its operating range. Several challenges with the blade passage model encountered during the course of this research were detailed and suggestions for their resolutions were given. A preliminary extension to the body force model for two-phase flows was formulated and initial calculations suggest the approach taken will successfully capture the observed steady cavitation behavior.

## 5.2 Conclusions

Several conclusions can be drawn from the research presented in this thesis:

- The axial turbopump inducer represents a challenging case for the body force modeling methodology due to the high blade stagger angles and leading edge backsweep which typify the geometry.
- The presence of upstream backflow regions driven by the tip clearance flows in inducer flow fields, and the associated radial flows within the blade passage, require the introduction of an additional force component, the binormal force, to enable the body force model to capture the flow fields accurately.
- The potential pitch angle instability and the discrepancy observed in near hub force distributions must be investigated and resolved before the body force model can be successfully used to study rotating cavitation and higher order cavitation instabilities.
- Preliminary two-phase body force calculations indicate that incorporating the effect of cavitation on the inducer flow field into the body force model is achievable within the existing body force model framework.

## 5.3 Extension to Future Work

The following recommendations are made to guide the continued development of the body force model to enable the study of cavitation instabilities:

- Carry out an analytical stability analysis on the pitch angle dependency in the model to determine whether a positive feedback loop exists which will always drive formation of spurious recirculation regions
- Devise a new pitchwise averaged data extraction method which resolves the near wall difficulties observed in the present work. One potential avenue is to remove CFD-Post from the process entirely by exporting the computational

data in CGNS format and using freely available MATLAB CGNS libraries to process the data. The details of CFX's interpolation scheme for user input data near mesh boundaries should also be investigated.

- An adaptive fitting scheme which alters the polynomial fit order based on an error criterion could be implement to improve the performance of the analytical fits near the hub and shroud.
- If the pitch angle or force discrepancy issues can not be satisfactorily resolved, other methods of introducing local flow dependency could be investigating, including Benneke's look-up table approach [1], which was seen to successfully capture elements of rotating stall.

# Appendix A

# Appendix - Derivation of the Body Force Model Governing Equations

The governing equations for the flow within the inducer blade row are the Navier-Stokes equations, coupled with a appropriate statements of conservation of mass and energy.

$$\frac{1}{\rho}\frac{D\rho}{Dt} + \nabla \cdot \mathbf{u} = 0 \tag{A.1}$$

$$\rho\frac{D\mathbf{u}}{Dt} = -\nabla p + \nabla \cdot \underline{\underline{\tau}} \tag{A.2}$$

$$\rho\frac{Dh_t}{Dt} = \frac{\partial p}{\partial t} + \nabla \cdot \mathbf{q} + \nabla \cdot (\mathbf{u} \cdot \underline{\underline{\tau}}) + \rho\dot{Q} \tag{A.3}$$

The working fluid in the blade row is assumed to be incompressible. In addition, it is assumed that the blade, hub, and shroud are adiabatic, and there are no volumetric heat sources within the flow, meaning $\mathbf{q} = 0$ and $\dot{Q} = 0$. Under these conditions, the energy equation is decoupled from the continuity and momentum equations, and does not play a roll in determining the flow field within the blade passage. The continuity and momentum equations can be rewritten as

$$\frac{D\rho}{Dt} = 0\,, \tag{A.4}$$

$$\frac{D\mathbf{u}}{Dt} = -\frac{1}{\rho}\nabla p + \nu\nabla^2\mathbf{u}\,. \tag{A.5}$$

The momentum equation can be transformed into the rotating frame of the rotor using the following relation, where **u** is the velocity in the stationary frame, **w** is the velocity in the rotating frame, **Ω** is the rotation vector of the rotor, and **r** is a vector from the rotational axis to the evaluation point.

$$\mathbf{u} = \mathbf{w} + (\boldsymbol{\Omega} \times \mathbf{r}) \tag{A.6}$$

This leads to the appearance of two fictitious forces in the equations, the centrifugal term and the coriolis term.

$$\frac{D\mathbf{w}}{Dt} = -\frac{1}{\rho}\nabla p + \nu\nabla^2\mathbf{w} - \boldsymbol{\Omega} \times (\boldsymbol{\Omega} \times \mathbf{r}) - 2(\boldsymbol{\Omega} \times \mathbf{w}) \tag{A.7}$$

The next step is to express these equations in the natural coordinate system detailed in Section 3.2. The appropriate coordinate transformation matrices are given below (note that the vector on the right is in terms of $-\theta$, in order to make the base coordinate system right-handed).

$$\begin{pmatrix} l \\ n \\ h \end{pmatrix} = \begin{pmatrix} \cos\beta & -\sin\beta & 0 \\ \sin\beta & \cos\beta & 0 \\ 0 & 0 & 1 \end{pmatrix} \begin{pmatrix} \cos\varphi & 0 & \sin\varphi \\ 0 & 1 & 0 \\ -\sin\varphi & 0 & \cos\varphi \end{pmatrix} \begin{pmatrix} x \\ -\theta \\ r \end{pmatrix} \tag{A.8}$$

$$= \begin{pmatrix} \cos\beta\cos\varphi & -\sin\beta & \cos\beta\sin\varphi \\ \sin\beta\cos\varphi & \cos\beta & \sin\beta\sin\varphi \\ -\sin\varphi & 0 & \cos\varphi \end{pmatrix} \begin{pmatrix} x \\ -\theta \\ r \end{pmatrix} \tag{A.9}$$

Using these transformations, each term in the equation can be appropriately transformed. The pressure gradient term is simple, as it is just the normal cartesian gradient operator.

$$\nabla p = \frac{\partial p}{\partial l}\,\hat{\mathbf{l}} + \frac{\partial p}{\partial n}\,\hat{\mathbf{n}} + \frac{\partial p}{\partial h}\,\hat{\mathbf{h}} \tag{A.10}$$

The centrifugal term has components in all three directions after the coordinate transform.

$$\begin{aligned}\boldsymbol{\Omega} \times (\boldsymbol{\Omega} \times \mathbf{r}) &= -\Omega^2 r\,\hat{\mathbf{r}} & \text{(A.11)}\\ &= -\Omega^2 r \sin\varphi \cos\beta\,\hat{\mathbf{l}} - \Omega^2 r \sin\beta \sin\varphi\,\hat{\mathbf{n}} - \Omega^2 r \cos\varphi\,\hat{\mathbf{h}} & \text{(A.12)}\end{aligned}$$

The Coriolis term lacks a component in the streamline direction since it is normal to the velocity vector.

$$\begin{aligned}\boldsymbol{\Omega} \times \mathbf{w} &= \Omega w_\theta\,\hat{\mathbf{r}} - \Omega w_r \hat{\theta} & \text{(A.13)}\\ &= -\Omega w \sin\varphi\,\hat{\mathbf{n}} - \Omega w \cos\varphi \sin\beta\,\hat{\mathbf{h}} & \text{(A.14)}\end{aligned}$$

The viscous stress term is just as simple as the pressure gradient term, since the normal cartesian definition of the vector laplacian operator can be directly applied. This results in an expression with only a component in the streamline direction.

$$\nabla^2 \mathbf{w} = \nabla^2 w\,\hat{\mathbf{l}} \tag{A.15}$$

The material derivative term can be decomposed into a time derivative and its associated convective derivatives.

$$\frac{D\mathbf{w}}{Dt} = \frac{\partial \mathbf{w}}{\partial t} + (\mathbf{w} \cdot \nabla)\mathbf{w} \tag{A.16}$$

The time derivative can then be expanded into two terms, one which expresses the unsteady acceleration along the streamline and another which expresses the unsteady change in streamline curvature.

$$\frac{\partial \mathbf{w}}{\partial t} = \frac{\partial w}{\partial t}\hat{\mathbf{l}} + w\frac{\partial \hat{\mathbf{l}}}{\partial t} \tag{A.17}$$

The second term is expanded by taking the appropriate derivative, which yields

$$\frac{\partial \hat{\mathbf{l}}}{\partial t} = \frac{\partial}{\partial t}\left(\cos\beta\cos\varphi\,\hat{\mathbf{x}} + \sin\beta\,\hat{\theta} + \cos\beta\sin\varphi\,\hat{\mathbf{r}}\right)\,, \tag{A.18}$$

$$= \left(-\cos\varphi\sin\beta\frac{\partial \beta}{\partial t} - \cos\beta\sin\varphi\frac{\partial \varphi}{\partial t}\right)\hat{\mathbf{x}} + \cos\beta\frac{\partial \beta}{\partial t}\,\hat{\theta} \tag{A.19}$$

$$+ \left(-\sin\beta\sin\varphi\frac{\partial \beta}{\partial t} + \cos\beta\cos\varphi\frac{\partial \varphi}{\partial t}\right)\hat{\mathbf{r}}\,. \tag{A.20}$$

Transforming back to the natural coordinate system gives

$$\frac{\partial \hat{\mathbf{l}}}{\partial t} = -\frac{\partial \beta}{\partial t}\,\hat{\mathbf{n}} + \cos\beta\frac{\partial \varphi}{\partial t}\,\hat{\mathbf{h}}\,. \tag{A.21}$$

The final expression for the time derivative term is then

$$\frac{\partial \mathbf{w}}{\partial t} = \frac{\partial w}{\partial t}\,\hat{\mathbf{l}} + -w\frac{\partial \beta}{\partial t}\,\hat{\mathbf{n}} + w\cos\beta\frac{\partial \varphi}{\partial t}\,\hat{\mathbf{h}}\,. \tag{A.22}$$

The convective derivatives are also expanded, and become

$$(\mathbf{w}\cdot\nabla)\mathbf{w} = w\frac{\partial w}{\partial l}\hat{\mathbf{l}} + w^2\frac{\partial \hat{\mathbf{l}}}{\partial l}\,. \tag{A.23}$$

The first term represents the acceleration of the fluid along the streamline, and the second is due to the turning of the streamline. An expression for $\frac{\partial \hat{\mathbf{l}}}{\partial l}$ can be found by again taking the appropriate derivative

$$\begin{aligned}
\frac{\partial \hat{\mathbf{l}}}{\partial l} =& \frac{\partial}{\partial l}\left(\cos\beta\cos\varphi\,\hat{\mathbf{x}} + \sin\beta\,\hat{\theta} + \cos\beta\sin\varphi\,\hat{\mathbf{r}}\right)\,, && \text{(A.24)}\\
=& \left(-\cos\varphi\sin\beta\frac{\partial\beta}{\partial l} - \cos\beta\sin\varphi\frac{\partial\varphi}{\partial l}\right)\hat{\mathbf{x}} + \cos\beta\frac{\partial\beta}{\partial l}\,\hat{\theta} && \text{(A.25)}\\
&+ \left(-\sin\beta\sin\varphi\frac{\partial\beta}{\partial l} + \cos\beta\cos\varphi\frac{\partial\varphi}{\partial l}\right)\hat{\mathbf{r}} + \sin\beta\frac{\partial\hat{\theta}}{\partial l} + \cos\beta\sin\varphi\frac{\partial\hat{\mathbf{r}}}{\partial l}\,. && \text{(A.26)}
\end{aligned}$$

The two derivatives $\frac{\partial\hat{\theta}}{\partial l}$ and $\frac{\partial\hat{\mathbf{r}}}{\partial l}$ are generally non-zero along the streamline, and capture the change in direction of the $\hat{\theta}$ and $\hat{\mathbf{r}}$ unit vectors in the original cylindrical coordinate system as $\theta$ changes. $\frac{\partial\hat{\theta}}{\partial l}$ is evaluated below.

$$\begin{aligned}
\frac{\partial\hat{\theta}}{\partial l} &= \frac{\partial\hat{\theta}}{\partial r}\cdot\frac{\partial r}{\partial l} + \frac{\partial\hat{\theta}}{\partial\theta}\cdot\frac{\partial\theta}{\partial l} + \frac{\partial\hat{\theta}}{\partial x}\cdot\frac{\partial x}{\partial l} && \text{(A.27)}\\
&= 0\cdot\frac{\partial r}{\partial l} + \frac{-\hat{\mathbf{r}}}{r}\cdot\frac{\partial\theta}{\partial l} + 0\cdot\frac{\partial x}{\partial l} && \text{(A.28)}\\
&= \frac{-\hat{\mathbf{r}}}{r}\cdot -\sin\beta && \text{(A.29)}
\end{aligned}$$

$\frac{\partial\theta}{\partial l}$ comes from the Jacobian matrix, which is simply the matrix inverse of the coordinate transformation matrix given earlier. $\frac{\partial\hat{\mathbf{r}}}{\partial l}$ is evaluated similarly, and the result is

$$\frac{\partial\hat{\mathbf{r}}}{\partial l} = \frac{\hat{\theta}}{r}\cdot -\sin\beta\,. \tag{A.30}$$

Collecting terms and then applying the coordinate transformation matrix to find the result in the natural coordinate system gives the following expression for $\frac{\partial \hat{\mathbf{l}}}{\partial l}$.

$$\frac{\partial \hat{\mathbf{l}}}{\partial l} = \left(-\frac{\partial \beta}{\partial l} - \sin\varphi \frac{\sin\beta}{r}\right) \hat{\mathbf{n}} + \left(\cos\beta \frac{\partial \varphi}{\partial l} - \cos\varphi \frac{\sin^2\beta}{r}\right) \hat{\mathbf{h}} \tag{A.31}$$

The final expression for the convective derivatives is then

$$(\mathbf{w}\cdot\nabla)\mathbf{w} = w\frac{\partial w}{\partial l}\hat{\mathbf{l}} + w^2\left[\left(-\frac{\partial \beta}{\partial l} - \sin\varphi \frac{\sin\beta}{r}\right) \hat{\mathbf{n}} + \left(\cos\beta \frac{\partial \varphi}{\partial l} - \cos\varphi \frac{\sin^2\beta}{r}\right) \hat{\mathbf{h}}\right]. \tag{A.32}$$

Returning to the full governing equations, collecting the terms in each direction results in three expressions. First, in the direction parallel to the streamline (the $\hat{\mathbf{l}}$ direction)

$$\frac{\partial w}{\partial t} + w\frac{\partial w}{\partial l} = -\frac{1}{\rho}\frac{\partial p}{\partial l} + \nu\nabla^2 w + \Omega^2 r \sin\varphi \,.\, \cos\beta \tag{A.33}$$

Next, the direction normal to the streamline on the stream surface

$$-w\frac{\partial \beta}{\partial t} + w^2\left(-\frac{\partial \beta}{\partial l} - \sin\varphi \frac{\sin\beta}{r}\right) = -\frac{1}{\rho}\frac{\partial p}{\partial n} + \Omega^2 r \sin\beta\sin\varphi + 2\Omega w \sin\varphi\,. \tag{A.34}$$

Lastly, the direction normal to the stream surface

$$w\cos\beta\frac{\partial \varphi}{\partial t} + w^2\left(\cos\beta \frac{\partial \varphi}{\partial l} - \cos\varphi \frac{\sin^2\beta}{r}\right) = -\frac{1}{\rho}\frac{\partial p}{\partial h} + \Omega^2 r \cos\varphi + 2\Omega w \cos\varphi\sin\beta\,. \tag{A.35}$$

The flow is further assumed to be quasi-steady and inviscid, with the viscous effects from the boundary layer on the inducer blades captured by the parallel force within the body force model. The final governing equations are then as follows. First, the parallel direction:

$$w\frac{\partial w}{\partial l} = -\frac{1}{\rho}\frac{\partial p}{\partial l} + \Omega^2 r \sin\varphi \cos\beta\,. \tag{A.36}$$

Next, the normal direction

$$w^2\left(-\frac{\partial \beta}{\partial l} - \sin\varphi\frac{\sin\beta}{r}\right) = -\,\frac{1}{\rho}\frac{\partial p}{\partial n} + \Omega^2 r \sin\beta\sin\varphi + 2\Omega w \sin\varphi\,. \tag{A.37}$$

Lastly, the binormal direction

$$w^2\left(\cos\beta\frac{\partial \varphi}{\partial l} - \cos\varphi\frac{\sin^2\beta}{r}\right) = -\frac{1}{\rho}\frac{\partial p}{\partial h} + \Omega^2 r \cos\varphi + 2\Omega w \cos\varphi\sin\beta\,. \tag{A.38}$$

# Appendix B

# Appendix - Influence Coefficient Analysis for Incompressible Swirling Flow

The objective for the influence coefficient analysis of incompressible swirling flow is to identify the influence coefficients for the normal and binormal pressure gradient terms in the body force model governing equations. The analysis is based on the compressible swirling flow influence analysis detailed in [6].

## B.1 Assumptions and Geometry

The following assumptions are made in this analysis:

- Steady, incompressible, adiabatic, and inviscid flow
- The axisymmetric swirling flow is bound to a two dimensional stream surface
- Axial, circumferential, and radial body forces are present

The analysis is done in a rotating reference frame, so the fictions centrifugal and coriolis forces must be included. The control volume used for the analysis is shown in Figure B-1.

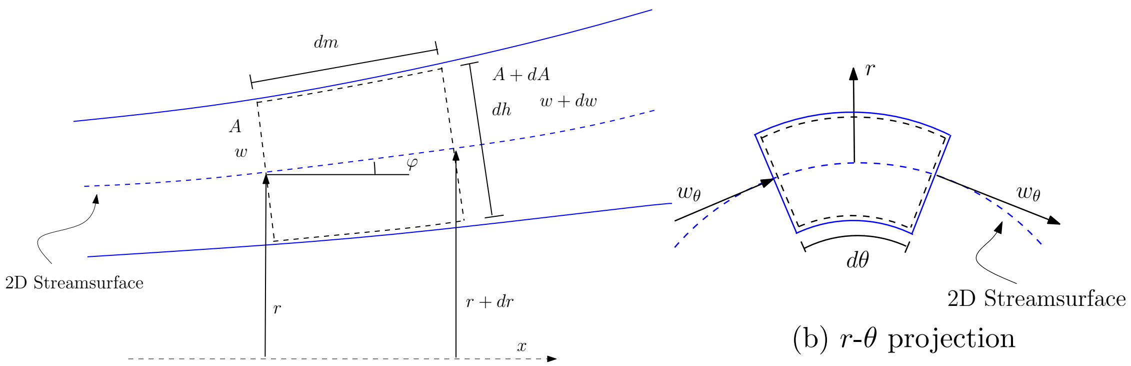

(a) $x$-$r$ projection (b) $r$-$\theta$ projection

Figure B-1: Differential control volume used in influence coefficient analysis

The coordinate transformation matrices in Appendix A are used to move from cylindrical to natural coordinates when appropriate.

## B.2 Governing Equations

The governing equations for the flow under the stated assumptions are the appropriate differential statements of the conservation of mass and meridional momentum.

$$\frac{dA}{A} = -\frac{dw_m}{w_m} \tag{B.1}$$

$$\frac{dp}{p} = -\frac{\rho w_m^2}{p}\frac{dw_m}{w_m} + \frac{\rho w_\theta^2}{p}\frac{dr}{r} + (f_l \cos\beta - f_n \sin\beta)\frac{\rho dm}{p} + (\Omega^2 r^2 + 2\Omega r w_\theta)\frac{\rho}{p}\frac{dr}{r} \tag{B.2}$$

The differential form of the meridional area definition is also required, and can be derived from modeling the stream surface as a frustum cone.

$$\frac{dA}{A} = \frac{dr}{r} \tag{B.3}$$

## B.3 Solution for the Normal Pressure Gradient Term

Beginning with the meridional momentum equation, use the continuity equation and the meridional flow area definition to express $\frac{dp}{p}$ solely in terms of $dr$ and $dm$.

$$\frac{dp}{p} = \frac{\rho}{p}(w_m^2 + w_\theta^2)\frac{dr}{r} + (f_l \cos\beta - f_n \sin\beta)\frac{\rho dm}{p} + (\Omega^2 r^2 + 2\Omega r w_\theta)\frac{\rho}{p}\frac{dr}{r} \tag{B.4}$$

The definition of relative velocity is applied to simply the expression

$$\frac{dp}{p} = \frac{\rho}{p}w^2\frac{dr}{r} + (f_l \cos\beta - f_n \sin\beta)\frac{\rho dm}{p} + (\Omega^2 r^2 + 2\Omega r w_\theta)\frac{\rho}{p}\frac{dr}{r}\,. \tag{B.5}$$

The geometric slope of the stream surface is

$$\frac{dr}{dm} = \sin\varphi\,. \tag{B.6}$$

Substituting this expression into Equation B.5 eliminates $dr$.

$$\frac{dp}{p} = (f_l \cos\beta - f_n \sin\beta)\frac{\rho dm}{p} + (\frac{w^2}{r} + \Omega^2 r + 2\Omega w_\theta)\sin\varphi\frac{\rho dm}{p} \tag{B.7}$$

Rearranging Equation B.7 yields an expression for the meridional pressure gradient.

$$\frac{1}{\rho}\frac{\partial p}{\partial m} = (f_l \cos\beta - f_n \sin\beta) + (\frac{w^2}{r} + \Omega^2 r + 2\Omega w_\theta)\sin\varphi \tag{B.8}$$

Taking the normal component gives the desired expression for the normal pressure gradient.

$$\frac{1}{\rho}\frac{\partial p}{\partial n} = (-f_l \cos\beta\sin\beta + f_n \sin^2\beta) - (\frac{w^2}{r} + \Omega^2 r + 2\Omega w_\theta)\sin\varphi\sin\beta \tag{B.9}$$

This expression is then substituted into the normal force model to derive the final normal force component model.

## B.4 Solution for the Binormal Pressure Gradient Term

Two more geometry definitions are required to create an expression for the binormal pressure gradient. These are the orthogonality of the meridional and binormal directions, and the differential ratio of radius to binormal direction changes.

$$\frac{dm}{dh} = 0 \tag{B.10}$$

$$\frac{dr}{dm} = -\cos\varphi \tag{B.11}$$

Applying these expressions to Equation B.5 gives

$$\frac{dp}{p} = -\cos\varphi(\frac{w^2}{r} + \Omega^2 r + 2\Omega w_\theta)\frac{\rho dh}{p}\,. \tag{B.12}$$

With suitable rearranging, the final binormal pressure gradient expression is

$$\frac{1}{\rho}\frac{\partial p}{\partial h} = -\cos\varphi(\frac{w^2}{r} + \Omega^2 r + 2\Omega w_\theta)\,. \tag{B.13}$$

Just as for the normal pressure gradient, this expression is used to create the final, recast binormal force component model.

# Bibliography

[1] B. Benneke. A Methodology for Centrifugal Compressor Stability Prediction. Master's thesis, Massachusetts Institute of Technology, 2009.

[2] M. Brand. An Improved Blade Passage Model for Estimating Off Design Axial Compressor Performance. Master's thesis, Massachusetts Institute of Technology, 2013.

[3] C. Brennen. *Hydrodynamics of Pumps.* 2011.

[4] C. Brennen and A Acosta. The Dynamic Transfer Function for a Cavitating Inducer. *Journal of Fluids Engineering*, 1976.

[5] Y. Gong. *A Computational Model for Rotating Stall and Inlet Distortions in Multistage Compressors.* PhD thesis, Massachusetts Institute of Technology, 1999.

[6] E. Greitzer, C. Tan, and M. Graf. *Internal Flow: Concepts and Applications.* Cambridge University Press, 2004.

[7] A. Hosangadi, V. Ahuja, and R. Ungewitter. Simulations of Cavitating Flows in Turbopumps. *Journal of Propulsion and Power*, August 2004.

[8] A. Hosangadi, V. Ahuja, and R. Ungewitter. Simulations of Rotational Cavitation Instabilities in the SSME LPFP Inducer. *43rd AIAA Joint Propulsion Conference*, (July), 2007.

[9] A. Hosangadi, V. Ahuja, and R. Ungewitter. Simulation of Cavitation Instabilities in Inducers. In *Proceedings of the Seventh International Conference on Cavitation*, 2009.

[10] K. Kamijo, H. Tamada, and N. Sakazume. Development History of Liquid Oxygen Turbopump for the LE-7 Engine. *36th AIAA Joint Propulsion Conference*, 2000.

[11] K. Kamijo, M. Yoshida, and Y. Tsujimoto. Hydraulic and Mechanical Performance of LE-7 LOX Pump Inducer. *Journal of Propulsion and Power*, 9(6), 1993.

[12] G. Kiwada. Development of a Body Force Description for Compressor Stability Assessment. Master's thesis, Massachusetts Institute of Technology, 2008.

[13] A. Kottapalli. Development of a Body Force Model for Centrifugal Compressors. Master's thesis, Massachusetts Institute of Technology, 2013.

[14] C. Lettieri, W. Sorensen, and Z. Spakovszky. Future Publication on MIT Psuedo-Low Pressure Oxidizer Pump.

[15] F. Marble. Three-Dimensional Flow in Turbomachines. *High Speed Aerodynamics and Jet Propulsion*, 1964.

[16] A. Mulder. NASA Low Pressure Oxidizer Pump Experimental Data. Personal Communication.

[17] A. Peters. *Ultra-Short Nacelles for Low Fan Pressure Ratio Propulsors.* PhD thesis, Massachusetts Institute of Technology, 2014.

[18] D. Prasad. Personal Communication.

[19] R. Ryan. The Space Shuttle Main Engine Liquid Oxygen Pump High-Synchronous Vibration Issue: The Problem , The Resolution Approach , The Solution. In *Proceedings of the 30th AIAA Joint Propulsion Conference*, 1994.

[20] D. Scheer. NASA CR-72712 Study of Inducer Loads and Stresses. Technical report, NASA, 1970.

[21] N. Shimiya, A. Fujii, and H. Horiguchi. Suppression of Cavitation Instabilities In an Inducer by J-Groove. In *Proceedings of the Sixth International Symposium on Cavitation*, 2006.

[22] M. Subbaraman and M. Patton. Suppressing Higher Order Cavitation Phenomena in Axial Inducers. In *Proceeding of the 6th Int. Symposium on Cavitation*, 2006.

[23] Y. Tsujimoto, K. Kamijo, and C. Brennen. Unified Treatment of Flow Instabilities of Turbomachines. *Journal of Propulsion and Power*, 17, 2001.

[24] Y. Tsujimoto, K. Kamijo, and Y. Yoshida. A Theoretical Analysis of Rotating Cavitation in Inducers. *Journal of Fluids Engineering*, 115(March), 1993.

[25] Y. Tsujimoto and Y. Yoshida. Observations of Oscillating Cavitation of an Inducer. *Journal of Fluids Engineering*, 119, 1997.

[26] H. Ugajin, M. Kawai, and K. Okita. Numerical Simulation of Unsteady Cavitating Flow in a Turbopump Inducer. In *Proceedings of the 42nd AIAA Joint Propulsion Conference*, 2006.

[27] T. Zoladz. Overview of Rotating Cavitation and Cavitation Surge in the Fastrac Engine LOX Turbopump. Technical report, NASA Marshall Spaceflight Center, Huntsville, Alabama, 2001.

[28] P. Zwart, A. Gerber, and T. Belamri. A Two-Phase Flow Model for Predicting Cavitation Dynamics. In *Proceedings of the Fifth International Conference on Multiphase Flow*, 2004.